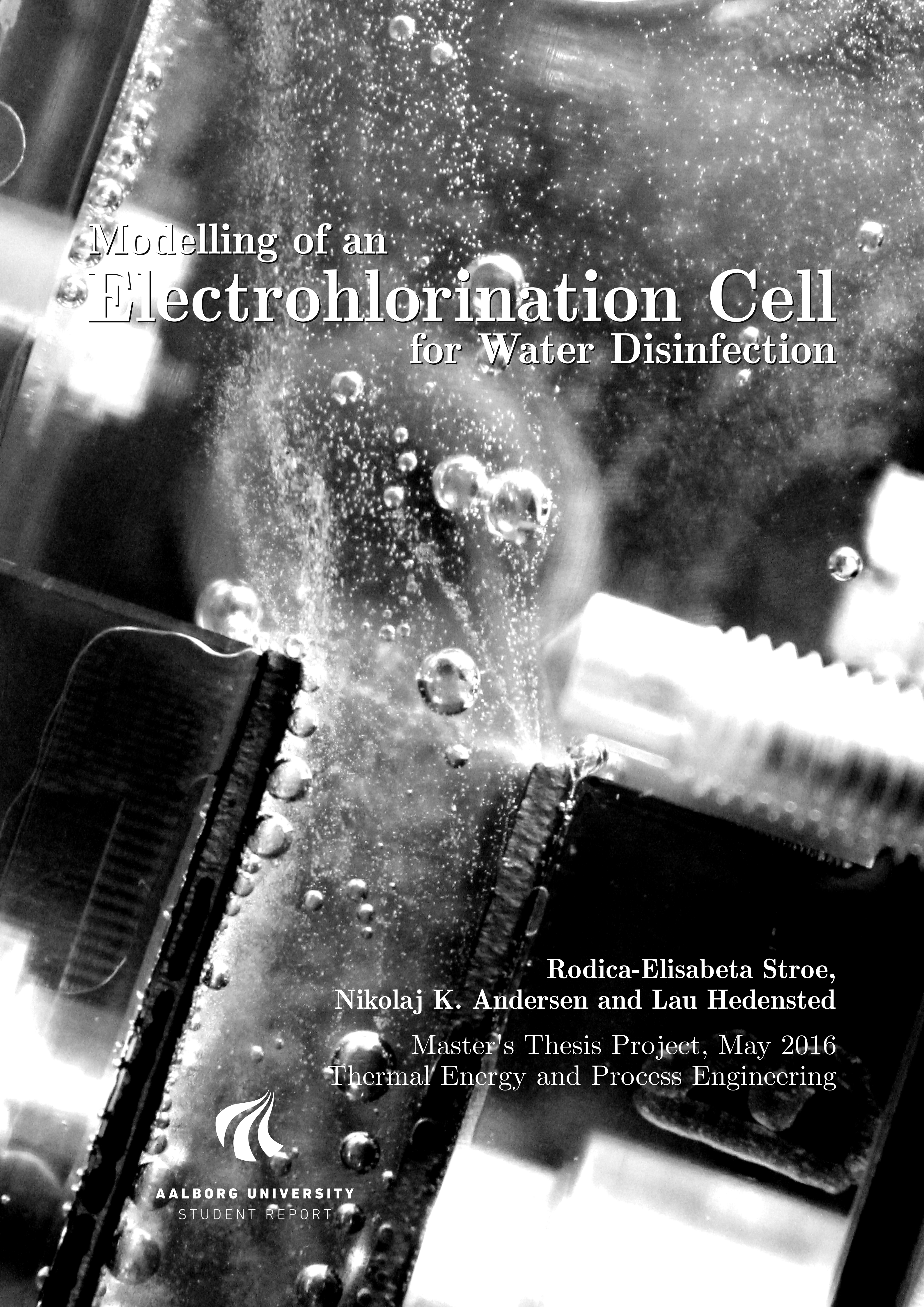

Modelling of an Electrohlorination Cell for Water Disinfection

Rodica-Elisabeta Stroe,
Nikolaj K. Andersen and Lau Hedensted

Master's Thesis Project, May 2016
Thermal Energy and Process Engineering

AALBORG UNIVERSITY
STUDENT REPORT

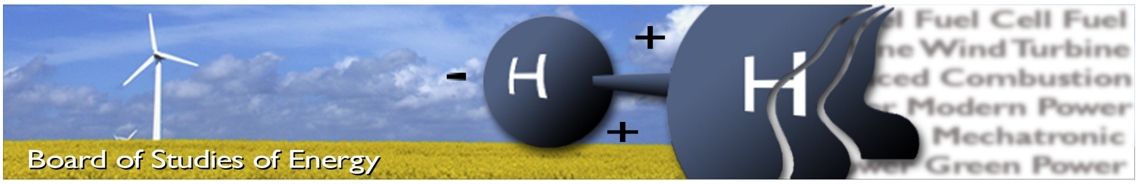

Title: Modelling of an Electrochlorination Cell for Water Disinfection
Semester: 9th and 10th, autumn semester 2015 to spring semester 2016
Project period: 02.09.2015 to 25.05.2016
ECTS: 50
Supervisors: Anders Christian Olesen, Jakob Hærvig & Henrik Sørensen
Project group: TEPE4-900

Lau Hedensted

Nikolaj Kortbek Andersen

Rodica-Elisabeta Stroe

Copies: 6
Pages, total: 155
Appendices: 7
Supplements: CD

SYNOPSIS:

The production of hypochlorite through electrolysis is a fast, reliable and on-site method of producing disinfectants for water treatment. This work presents the modelling of an undivided electrochlorination cell and the experiments carried out on a test cell for model validation. The numerical model made in COMSOL Multiphysics couples the various processes describing the electrochlorination - electrochemistry, chemical reactions, transport of species and two-phase, gas-liquid flow. Thus, establishing a comprehensive model, which can predict the behaviour of the cell. To characterize the dispersed gas bubbles, experiments are carried out using a direct imaging method that enables the capturing of shadow images of bubbles for size, gas volume fraction and velocity determinations. The model is validated against this data and the polarisation curve of the test cell, and its behaviour at varying input parameters is observed through a sensitivity analysis. Additional investigations are conducted for an electrochlorination cell with a smaller cell gap and higher cell voltage, resembling industrial applications.

By signing this document, each member of the group confirms that all participated in the project work and thereby all members are collectively liable for the content of the report. Furthermore, all group members confirm that the report does not include plagiarism.

Preface

This master's thesis is the documentation of the work carried out during September 2$^{\text{nd}}$ and May 25$^{\text{th}}$ 2016 by a group of fourth semester master students, studying Thermal Energy and Process Engineering at Aalborg University.

The aim of this project is to model the process of hypochlorite electrogeneration in an undivided electrochlorination cell and to experimentally investigate the flow dynamics, with emphasis on the bubble evolution at the electrodes. In order to investigate the flow dynamics an imaging system for capturing the evolved bubbles is set up and processing algorithms are developed for analysing the gathered images.

The written outcome of this project consists of this report, a conference paper, and a conference poster. The Conference Paper: *Measurement of bubble shape and size in bubbly flow structure for stagnant and pulsating liquid flow using an undivided electrochlorination cell and Telecentric Direct Image Method* investigates the flow structure of the gas bubbles in two different flow types by means of a direct imaging method which allows the capturing of bubble shadows. The poster was made to be presented at the International Conference of Multiphase Flow 2016, where the paper was submitted and accepted. The Conference Paper is found in Appendix A.

This report covers the experiments carried out for bubble size and velocity y-component, and gas volume fraction determinations and the numerical model of the electrochlorination process. It contains the following parts:

- Description of the electrochlorination system on which the numerical model is based and with which experiments are conducted.
- Methods and procedures employed for bubble image capturing, processing and analysis, with the purpose of determining the size of the bubbles, as well as gas volume fraction and y-component of the bubble velocity.
- Description of applied theory, assumptions, and choices made for the modelling of the electrochlorination cell.
- Considerations about the numerical strategy, simulations and mesh design in COMSOL Multiphysics.
- Validation of the model against the acquired experimental data.
- Investigations of model behaviour through a sensitivity analysis.
- Investigations of model behaviour at conditions resembling those used in industrial applications.

The project presupposes a level of general knowledge about fluid dynamics and two-phase flows, as well as basic notions of electrochemistry. Basic acquaintance with Computational

Fluid Dynamics techniques and direct imaging methods can be an advantage to the reader. In addition, basic knowledge of COMSOL Multiphysics would be advantageous, but not required.

Instructions:
The report conforms to the scientific standard of citing the sources used throughout. The report follows the Harvard citation method, where sources are listed in the text as [Surname, year]. This citation refers to the bibliography at the end of the report, where books are listed with author, year, title, edition and publisher; Websites are listed with author, title, date and URL; Articles are listed with author, title, journal, year. The bibliography is arranged alphabetically. Citations placed outside the sentence are in connection to the whole paragraph, whereas citations inside a sentence refer to that particular sentence.

Figures, tables and equations are numbered according to chapters and appendices and the order of appearance therein. Furthermore, electronic versions of this report and executive summary, together with the models, programs, and scripts developed throughout the project, as well as the Conference Paper and the conference poster were submitted. The interested reader can acquire these by contacting Anders Christian Olesen at aco@et.aau.dk or Henrik Sørensen at hs@et.aau.dk.

Acknowledgements:
The authors would like to thank Grundfos Holding A/S for providing the electrochlorination system. Furthermore, the authors would like to thank Karin Doolewerdt, Maryam Momeni and Helge Grann for very valuable discussions and much knowledgeable criticism.

Nomenclature

Abbreviations

Abbreviation	Explanation
AI	Interrogation Area
BF	Bubbly Flow (COMSOL Module)
CCD	Charge-Coupled Device
CHEM	Chemistry (COMSOL Module)
CMOS	Complementary Metal-Oxide-Semiconductor
DAQ	Data Acquisition Device
EEAR	Equivalent Ellipse Axis Ratio
enh.	Enhanced
FEM	Finite Element Method
FFT	Fast Fourier Transform
FOD	Field of Depth
FOV	Field of View
fps	Frames per second
LabVIEW	Laboratory Virtual Instrument Engineering Workbench
LED	Light Emitting Diode
LIF	Laser Induced Fluorescence
LII	Laser Induced Incandescence
LKP	Pyramid implementation of the Lucas-Kanade algorithm
MATLAB	Matrix Laboratory
MAX	Measurement & Automation Explorer (Software)
NaN	Not a Number
NI	National Instruments
PDE	Partial Differential Equation
PIV	Particle Image Velocimetry
PMAG	Primary Magnification
PVC	Polyvinyl Chloride
SCD	Secondary Current Distribution (COMSOL Module)
TDIM	Telecentric Direct Image Method
TDS	Transport of Dilute Species (COMSOL Module)
UOD	Universal Outlier Detection
UV	Ultraviolet
VI	Virtual Instrument (LabVIEW program)
AAU	Aalborg University

List of symbols

Symbol	Explanation	Unit
$\mathbf{0}$	Zero vector	$[-]$
A	Area	$[\mathrm{m}^2]$
AR	Aspect ratio	$[-]$

List of symbols - Continued

Symbol	Explanation	Unit
A_{EE}	Equivalent ellipse area	[px^2]
a	Equivalent ellipse semi-major axis, $2a = E_{2a}$	[px]
a_{factor}	Electrode surface factor	[$-$]
α	Transfer coefficient	[$-$]
b	Equivalent ellipse semi-minor axis, $2b = E_{2b}$	[px]
$\beta_{overall}$	Overall current efficiency	[$-$]
C_D	Drag coefficient	[$-$]
C_W	Linearisation parameter	[$\text{kg}/(\text{m}^3\,\text{s})$]
c	Concentration	[mol/m^3]
D	Diffusion coefficient	[m^2/s]
d_b	Diameter of gas bubbles	[m]
ΔS_b	Bubble displacement	[µm]
ΔS	Displacement	[px]
$\Delta \boldsymbol{S}_r$	Residual displacement vector	[px]
Δx	Mesh element size	[m]
δ	Diffusion layer thickness	[m]
E_{2a}	Equivalent ellipse major axis	[px]
E_{2b}	Equivalent ellipse minor axis	[px]
Eo	Eötvös number	[$-$]
E_{eq}	Equilibrium potential	[V]
ϵ	Minimum normalisation level	
ε	Image matching error	[$-$]
η	Activation overpotential	[V]
F	Faraday's constant	[C/mol]
FOV	Field of view	[µm]
f	Volume force	[N/m^3]
f_{AM}	Volume force due to added mass	[N/m^3]
f_B	Volume force due to buoyancy	[N/m^3]
f_D	Volume force due to drag	[N/m^3]
f_{int}	Force contributions from drag, added mass and lift	[N/m^3]
f_L	Volume force due to lift	[N/m^3]
$\boldsymbol{g}$	Gravitational acceleration	[m/s^2]
Γ	Control volume surface	[m^2]
Γ_q	Control surface for definition of q	[m^2]
Γ_ϕ	Control surface for definition of φ	[m^2]
γ	Tafel slope	[V/decade]
h	Parameter	[$-$]
I	Image matrix	[$-$]
$\boldsymbol{I}$	Identity matrix	[$-$]
I_0	Original unprocessed image matrix	[$-$]
$\bar{I}_{BG}$	Averaged background image matrix	[$-$]
I_c	Contrast enhanced foreground image matrix	[$-$]

List of symbols - Continued

Symbol	Explanation	Unit
I_f	Foreground image matrix	[−]
i_{loc}	Local current density (reaction specific)	[A/m^2]
I_n	Normalised foreground image matrix	[−]
I_{res}	Image resolution	[px]
i_0	Exchange current density	[A/m^2]
$\boldsymbol{i}_l$	Current density	[A/m^2]
K_{eq}	Equilibrium constant	[See Pages 45 and 46]
k	Thermal conductivity	[W/(m K)]
k_f	Forward rate constant	[s^{-1}]
k_{log}	Tafel slope correction coefficient	[−]
k_m	Mass transfer coefficient	[m/s]
k_O	Oxidised species coefficient	[−]
k_R	Reduced species coefficient	[−]
k_r	Backward rate constant	[See Pages 43 and 46]
L	Pyramid level, see Appendix D	[−]
l	Computational 1D domain length	[m]
Λ	Generic source term	
M	Molar mass	[kg/mol]
$\dot{m}$	Mass flow rate	[kg/s]
$\dot{m}''$	Mass flux	[kg/(m^2 s)]
$\dot{m}''_0$	Mass boundary flux	[kg/(m^2 s)]
$\dot{m}'''_{gl}$	Mass transfer rate between the gas and liquid phases	[kg/(m^3 s)]
μ	Dynamic viscosity	[kg/(m s)]
N	Shape function	
$\boldsymbol{N}''$	Molar flux	[mol/(m^2 s)]
$\boldsymbol{N}''_0$	Molar boundary flux	[mol/(m^2 s)]
n	Refractive index	[−]
$\boldsymbol{n}$	Normal vector	[−]
n_b	Number of bubbles	[−]
n_{e^-}	Number of electrons	[−]
n_{img}	Number of images	[−]
ν	Stoichiometric coefficient	[−]
$\boldsymbol{o}$	Image coordinate, $\boldsymbol{o} = (x, y)^T$	[px]
Ω	Domain surface	[m^2]
ω	Integer which defines LKP search area	[px]
$\boldsymbol{P}$	Array of bubble positions	[px]
P_{EE}	Equivalent ellipse perimeter	[px]
Pe_{el}	Element Peclet number	[−]
PMAG	Primary magnification	[−]
p	Pressure	[Pa]
Φ_l	Electrolytic solution potential	[V]
Φ_s	Electrode potential	[V]

List of symbols - Continued

Symbol	Explanation	Unit
ϕ	Volume fraction	[–]
φ	Potential function	
$\dot{Q}$	Volumetric flow rate	[L/h]
q	Heat flux	[W/m^2]
$\dot{R}$	Rate of production or consumption of a species	[mol/(m^3 s)]
$\mathcal{R}$	Ideal gas constant	[J/(mol K)]
Re	Reynolds number	[–]
r_0	Normalised vector residual	
r_m	Median residual	
Stk	Stokes number	[–]
S_{px}	Sensor pixel size	[µm]
ρ	Density	[kg/m^3]
σ	Electrolytic solution conductivity	[S/m]
ς	Surface tension	[N/m]
T	Temperature	[K]
$\{T^e\}$	Element vector with temperature nodal values	[K]
$\tilde{T}$	Temperature field	[K]
t	Time	[s]
τ	Response time	[s]
θ	Angle	[°]
u	Velocity x-component	[m/s]
$\boldsymbol{u}$	Velocity vector, $\boldsymbol{u} = \boldsymbol{u}(u, v)$	[m/s]
$\boldsymbol{u}_0$	Inlet velocity of the electrolytic solution	[m/s]
$u_{g,sf}$	Superficial velocity of the gas phase	[m/s]
$\boldsymbol{U}_m$	Median vector	
u_m	Mobility	[(s mol)/kg]
$\boldsymbol{u}_{drift}$	Drift velocity due to turbulence	[m/s]
$\boldsymbol{u}_{slip}$	Slip velocity between phases	[m/s]
$\boldsymbol{x}$	Image coordinate, $\boldsymbol{x} = (x, y)^T$	[px]
x, y, z	Coordinates or component indicators	
$\boldsymbol{\xi}$	Guess vector, $\boldsymbol{\xi} = (\xi_x, \xi_y)$	[px]
V	Velocity	[m/s]
$\rlap{-}V$	Volume	[m^3]
$\rlap{-}V_{img}$	Image volume	[µm^3]
v	Velocity y-component	[m/s]
v_t	Terminal velocity of gas bubbles	[m/s]
w_{gap}	Width of cell gap	[m]
$w(x)$	Weight function	[–]
z	Valence	[–]
ζ	Tuning parameter	[–]

Commonly used subscripts

Script	Explanation
a	Anode
b	Bubble
c	Cathode
g	Gas phase
h	Horizontal
l	Liquid phase
v	Vertical

Chemical species and ions

Formula	Explanation
$ClO_3{}^-$	Chlorate
Cl^-	Chloride ion
Cl_2	Chlorine
H_2O	Dihydrogen monoxide (water)
H_2	Hydrogen
H^+	Hydrogen ion
OH^-	Hydroxide
OCl^-	Hypochlorite
HOCl	Hypochlorous acid
O_2	Oxygen
RuO_2	Ruthenium oxide
Na^+	Sodium ion
Ti	Titanium
e^-	Electron

Mathematical operators

Script	Explanation
∇	Vector differential operator
∂	Partial differential operator
$\bar{h}$	Mean value of h
T	Transpose (superscript)
$[]$	Vector
$\min(\boldsymbol{H})$	Minimum value of the matrix $\boldsymbol{H}$
$\max(\boldsymbol{H})$	Maximum value of the matrix $\boldsymbol{H}$

Table of contents

First Chapter

Introduction

Water has always been an important resource for humans, thus a lot of attention has been given to drinkable water as well as to the fulfilment of requirements for the medical, pharmaceutical, and industrial sectors. Furthermore, with the growing population and climate changes, regions across the world may be threatened by unavailability of drinkable water. The sources for drinkable water, such as lakes, rivers, and streams, have to be pretreated before use, as these can carry viruses and bacteria, or contain a chemical or microbial agent, all of which can cause numerous diseases in humans and animals. Thus, chemical disinfection processes, such as chlorination, flocculation, ozonation, and electromagnetic radiation, have been implemented to remove contaminants that can cause various diseases. [Black and Veatch Corporation, 2010]

For decades chlorine has been widely used with the purpose of disinfecting water and for wastewater treatment. The potential issues with using chlorine as disinfectant are the risks and hazards of handling, storing and transporting the large amounts of concentrated liquid chlorine needed for water disinfection. In the absence of moisture, liquid and gaseous chlorine will not attack ferrous metals, and can therefore be stored safely in steel containers. Current commercial technologies, however, are not able to produce "dry" liquid and gaseous chlorine, hence there is a risk of corrosion during storage. This makes it necessary to use steel containers with extra thick walls in order to prevent leaks resulting from corrosion. Furthermore, liquid chlorine has toxic effects and depending on the degree of exposure it can cause irritation to the respiratory system, as well as skin and eye irritation, which lead to injuries similar to burns or frostbites. Other potential hazards are the chlorine leaks, which generally are defined as discharges of liquid or gaseous chlorine into the atmosphere. These can be divided into 3 categories: minor, major, and catastrophic, such as valve failures, breaks in pipes under pressure, and ruptures in chlorine containers, respectively. [Black and Veatch Corporation, 2010]

Due to the risks of working with chlorine the on-site electrogeneration of hypochlorite from salt water electrolysis, also called electrochlorination, has become of interest in the recent years, especially in developing countries [Spasojevic et al., 2015]. This method of producing hypochlorite involves the electrolysis of an electrolytic solution containing sodium chloride, NaCl. The solution is pumped through an electrochlorination cell, which has a channel of relatively small thickness, the cell gap. On the sides of the cell gap a DC current of low voltage is applied through two electrodes, the anode and the cathode, which triggers the electrolysis of the electrolytic solution.

From the different cells, which are currently commercially available, the undivided cells, represented in Figure 1.1a, which use dilute electrolytic solutions or sea water, and divided chlor-alkali cells with incorporated membranes, Figure 1.1b, are most commonly used [J. Choi, 2013].

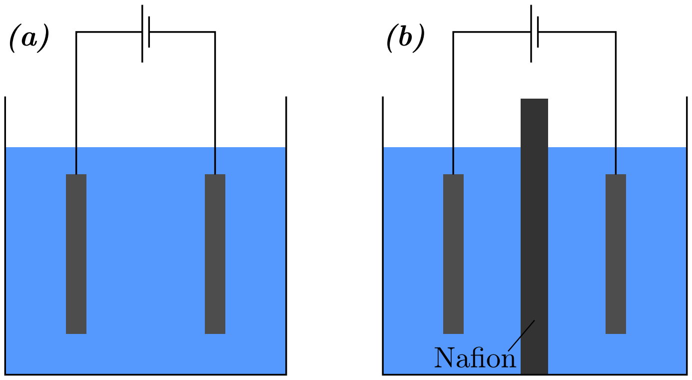

Figure 1.1. Conceptual drawing of an undivided electrolysis cell ***(a)*** and a divided electrolysis cell ***(b)***. Inspired by [J. Choi, 2013].

In this study, the technology of undivided cells is used for electrogeneration of hypochlorite, hence this cell type is the focus in the following.

Second Chapter

Problem analysis

2.1 System analysis

As introduced in Chapter 1, the main focus of this study is the undivided cells. On a large scale this process is used by Grundfos within the Selcoperm unit, shown in Figure 2.1, developed and used for water treatment. The main components of the system are the electrolysis system, storage tanks for the electrolytic solution and product solution, an exhaust fan for hydrogen removal and a dosing pump. When supplied with a saturated solution and electricity, the Selcoperm electrolytic chlorination system is capable of producing a hypochlorite solution. Among various advantages of using this technology, the following are mentioned: non-toxicity of used solution and products, on-site safe generation of hypochlorite and low operating cost. [Grundfos]

Figure 2.1. Selcoperm electro-chlorinator [Grundfos].

In order to study the phenomena occurring during operation of these electrochlorination systems, a small scale electrochlorination cell has been constructed, which likewise serves to validate a numerical model developed during this study. Figure 2.2 shows the small scale electrochlorination cell along with its two-dimensional representation. The two-dimensional representation together with the zooms used throughout the report are given in Appendix G for easy reference for the reader. The different zooms are referenced in the chapters in which they are used in order to clarify, where comparisons and investigations are carried out. The reader is encouraged to have Appendix G lying beside this report for easy reference.

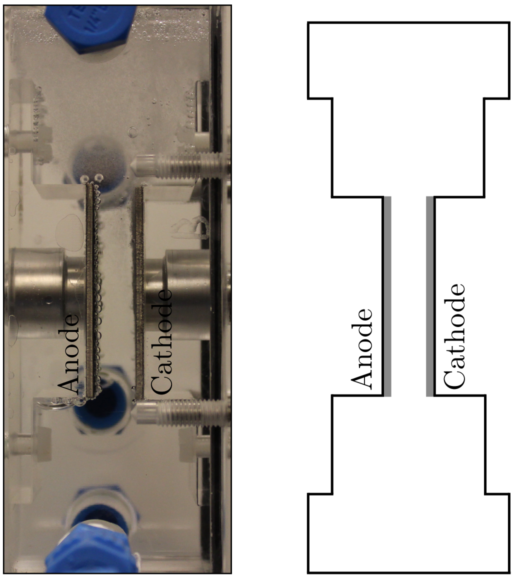

(a) Real cell. ***(b)*** 2D representation.

Figure 2.2. Small scale electrochlorination cell and its two-dimensional representation.

As seen from Figure 2.2, the small scale electrochlorination cell consists of a rectangular plexiglass walled cell with two electrodes immersed into the electrolytic solution, an inlet at the bottom, through which the electrolytic solution is fed to the cell, and an outlet at the top, that lets the product solution, as well as the formed gases, out of the cell. The electrolytic solution is prepared by dissolving the desired amount of NaCl in deionised water in a container from which it is fed to the cell at the desired liquid flow rate with the help of a pump. The anode is made out of ruthenium oxide-coated titanium (Ti/RuO_2) and the cathode is also made out of titanium, but unlike the anode, it is uncoated. The ruthenium oxide greatly increases the anode's resistance to corrosion, lifespan and improves the ability to operate at high voltages [Khelifa et al., 2004]. Furthermore, RuO_2 is an active electrocatalyst for oxygen and chlorine evolution. Thus, RuO_2-based anodes have an increased activity, selectivity and stability towards the chlorine evolution [Arikawa et al., 1998].

As stated in Chapter 1, the electrolysis of the electrolytic solution, which is fed to the electrochlorination cell occurs when a DC current is applied through the electrodes, initiating electrochemical reactions. In the case of a sodium chloride and water solution being fed through the electrochlorination cell, the following primary electrochemical reactions, Reactions (C 2.1) and (C 2.2), occur at the anode and cathode, respectively [C.Y. Cheng, 2007].

$$2\mathrm{Cl}^- \longrightarrow \mathrm{Cl}_2 + 2\,\mathrm{e}^- \qquad \text{(Anode)} \tag{C 2.1}$$

$$2\mathrm{H}_2\mathrm{O} + 2\,\mathrm{e}^- \longrightarrow \mathrm{H}_2 + 2\mathrm{OH}^- \qquad \text{(Cathode)} \tag{C 2.2}$$

Due to the potential difference across the cell gap, charged species will migrate towards either the anode or cathode, depending on their charge. Furthermore, concentration gradients in the electrolytic solution makes species in regions of high concentration diffuse towards regions with lower concentration and the forced flow of the electrolytic solution through the cell gap mixes the species. All of these effects will in turn result in Reactions

(C 2.3) to (C 2.8) taking place in the bulk flow [C.Y. Cheng, 2007].

$$2\,\mathrm{OCl}^- \rightleftharpoons 2\mathrm{Cl}^- + \mathrm{O}_2 \tag{C 2.3}$$

$$2\,\mathrm{HOCl} + \mathrm{OCl}^- \rightleftharpoons \mathrm{ClO_3}^- + 2\,\mathrm{Cl}^- + 2\,\mathrm{H}^+ \tag{C 2.4}$$

$$\mathrm{ClO}^- + \mathrm{H}_2 \rightleftharpoons \mathrm{H_2O} + \mathrm{Cl}^- \tag{C 2.5}$$

$$\mathrm{Cl}_2 + \mathrm{H_2O} \rightleftharpoons \mathrm{HOCl} + \mathrm{Cl}^- + \mathrm{H}^+ \tag{C 2.6}$$

$$\mathrm{HOCl} \rightleftharpoons \mathrm{H}^+ + \mathrm{OCl}^- \tag{C 2.7}$$

$$\mathrm{H_2O} \rightleftharpoons \mathrm{H}^+ + \mathrm{OH}^- \tag{C 2.8}$$

As seen from some of the bulk reactions, these will have a negative influence on the hypochlorite, OCl^-, output from the electrochlorination cell. Beside such reactions hypochlorite might also be consumed by the cathodic loss reaction. Similarly, a loss reaction is reported to occur at the anode. These secondary electrochemical reactions at the anode and cathode are given by (C 2.9) and (C 2.10), respectively [C.Y. Cheng, 2007].

$$2\mathrm{H_2O} \rightarrow \mathrm{O}_2 + 4\mathrm{H}^+ + 4\,\mathrm{e}^- \quad \text{(Anode loss reaction)} \tag{C 2.9}$$

$$\mathrm{OCl}^- + \mathrm{H_2O} + 2\,\mathrm{e}^- \rightarrow \mathrm{Cl}^- + 2\mathrm{OH}^- \quad \text{(Cathode loss reaction)} \tag{C 2.10}$$

These loss reactions mean that the current efficiency at the anode and cathode are less than one and that the hypochlorite output of the electrochlorination cell is less than the theoretical maximum.

As seen from Reactions (C 2.1), (C 2.2) and (C 2.9) species like Cl_2, H_2 and O_2 are produced. If their solubility in water is exceeded gas bubbles will be formed. Hence, the flow occurring inside the electrochlorination cell is a two-phase, gas-liquid flow. The presence of gas bubbles close to the electrodes of the electrochlorination cell will hinder the reactants access to the electrode surface and thus influence the current density of the electrochlorination cell. Furthermore, the gas bubbles will affect the migration and diffusion of aqueous species as these cannot migrate or diffuse to regions occupied by the gas bubbles. Hence, the presence of gas bubbles means that the electrolytic solution can be treated as a porous media. [Ipek et al., 2008]

Summing up, four phenomena have been identified to be occurring in the electrochlorination cell during operation:

- Electrochemistry
- Chemical Reactions
- Transport of species
- Two-phase, gas-liquid flow

To correctly model the behaviour of the electrochlorination cell during operation these phenomena have to be coupled to each other.

2.2 Existing models and studies of electrochemical systems with gas-evolving electrodes

Most mathematical models of electrochemical systems with gas-evolving electrodes only compute the current and concentration distributions. Thus, disregarding the fluid flow inside the cell, the evolution of bubbles and influence of these on the fluid flow dynamics, current distribution and the transport of species. Furthermore, because the evolution of bubbles is neglected, the existence of a two-phase flow is not taken into account. [Aldas et al., 2008]

Selman and Newman [1971] concluded that migration causes nonuniform concentration distribution in the electrolytic solution, which in turn greatly affects the velocity profile, compared to forced convection. Menon and Landau [1987] developed a 2D model to simulate electrochemical cells by taking into account migration, diffusion, and unsteady effects. The model was used to estimate the concentration distribution along the electrode surface and the current distribution under the influence of transport of species and unsteady-state behaviour in a system that relates the concentration to the potential field. Due to the fact that the electrolytic solution was considered to be stagnant and single phase, the influence of the flow and bubbles on cell parameters is not predicted by this model. Selman and Newman [1971] developed a model based on phenomena of free convection and ionic migration, in a system that uses a supporting electrolytic solution, with the purpose of investigating the contribution of migration to the limiting current in free convection. Wallgren et al. [1996], on the other hand, considered forced convection of a binary electrolytic solution through a two-dimensional channel with electrodes placed opposite to each other. Through the mathematical model they derived two modified boundary conditions below the limiting current density.

C.Y. Cheng [2007] modelled the hypochlorite production in electrochemical cells with near-neutral aqueous sodium chloride solution, considering both plate and porous electrodes. The model based on a porous anode aimed to investigate the feasibility of using such electrodes for enhancing the single pass conversion in oxidising chloride ions. Planar anodes were considered for the reactor model in order to study and analyse the effects of diffusion, migration and convection on the transport of species involved in the reactions. It was concluded that the single pass conversion was 36% more efficient in the case of a porous anode compared to a plate anode. Similarly, the overall current efficiency was reported to increase by 6% when replacing the plate electrode with a porous one.

As mentioned, even though numerous mathematical models are available in the literature, only few studies consider a two-phase flow and the influence of the bubbles on the flow dynamics, together with current distribution and the transport of species [Aldas et al., 2008].

Ibl and Landolt [1968] investigated the anodic process in the case of the formation of ClO_3^- in both dilute and concentrated NaCl solutions. It was concluded that the production of ClO_3^- is proportional to the concentration of OCl^- in the solution and that the mass transfer of $HOCl/OCl^-$ towards the anode is a rate-determining step for the production of ClO_3^-. A kinetic model was developed by Ibl and Vogt [1983] which was successfully used to predict the concentration profiles of the species involved in the anodic reaction layer in an electrogeneration of hypochlorite/chlorate process. Dahlkild [2001] modelled an electrochlorination cell considering a bubbly two-phase flow, which was coupled with a uniform electric current distribution along a single electrode. With this model the already existing experimental findings were confirmed, which showed that the non-uniformity of the current density distribution is given by the non-uniformity of the bubble distribution in the vicinity of the electrode. The model also helped in investigating the non-linear boundary condition which arises due to electrode kinetics.

This overview on the existing modelling approaches in the field of electrochemical systems with gas-evolving electrodes shows that there is still a need for models which incorporate and couple the different subprocesses taking place. Furthermore, the developed models have to be validated against measured data obtained from experiments. It was emphasized in this literature study that the gas bubbles plays an important role in these types of systems, because it can influence the fluid dynamics, the transport of species and also electrochemical parameters, such as the access of reactants to electrode surfaces. This points towards the necessity of a model which is able to handle a two-phase flow and to solve separate mass transport equations, while also solving for the current and concentration distribution. Furthermore, the desired two-phase flow model couples the concentration with the potential field and estimates the concentration along the surface of the electrodes. Finally, experimental data which describes the fluid flow, the evolution of bubbles, phase volume fractions and phase velocities are required for validation purposes and in order to obtain a complete model that is detailed enough for studying an electrochemical system, such as an electrochlorination cell.

2.3 Bubble measurement techniques

The techniques generally fall into one of two categories: intrusive and non-intrusive techniques [Boyer et al., 2002]. The former are easy to apply and robust, but have the disadvantage of influencing the fluid dynamics of the process through the presence of the probe and of being able to provide only local information about the desired parameters, meaning that extensive experiments have to be carried out in order to gather data for the whole geometry [Boyer et al., 2002]. Due to the risk of these techniques affecting the fluid flow, they cannot be used in the case of chemical and electrochemical systems where the flow should not be altered, as this would cause the chemical characteristics to change [Busciglio et al., 2013]. Hence, non-intrusive techniques are of interest.

Two non-intrusive techniques are generally used to study different important aspects of the two-phase flow; Particle Image Velocimetry (PIV) and Phase Doppler Anenometry (PDA). PIV has historically been used to determine the velocity field for a single phase flow. This method applies a laser sheet, which is used to illuminate a defined volume of the fluid carrying seeding particles. Pictures are then taken within a short time interval. The captured change in distance between the positions of the seeding particles, thus constitute the instantaneous velocity field of the fluid. Though, classically used for single-phase flows this method can be used for gas-liquid flow. However, in such cases the main problem has been reported to be the clear identification of the bubbles in the liquid. For PDA the emitted light by the laser is divided into two beams, which are focused on the volume desired for measuring. Two photodetectors are placed in the plane of the emitted laser beams and the direction of the flow. When a bubble flows into the focused volume, shifts in frequency, the Doppler-effect, are measured by both photodetectors. The velocity can be related to these shifts in frequency. Moreover, the bubble size can be determined by measuring the phase difference of the shifts in frequency, measured by the two detectors. The main disadvantages of these two techniques are the high level of required safety when operating with laser sheets and beams, the high cost of the equipment and software required to obtain the desired parameters of the gas-liquid flow and finally, that only flows with low gas volume fractions can be considered. [Boyer et al., 2002]

Boissonneau and Byrne [2000] applied PIV and PDA to investigate the two-phase flow regimes, bubble sizes, gas phase volume fraction and fluid velocities between the electrodes of an electrochemical cell. It was found that the fluid flow can transition from laminar to turbulent across the cell channel. In addition they were able to visualize the existence of three different regions in the vicinity of the electrodes characterised by different bubble regions; adherence, diffusion and bulk.

Image analysis techniques, whether it be the acquisition of still images or video recordings, have been used to capture images of many of the important flow aspects, such as flow structure, bubble size and shape, phase velocities and volume fractions. The main disadvantage of these techniques is the requirement of transparent walls and a transparent liquid in order to light up the flow, such that the desired flow parameters can be obtained. Moreover, just like in the case of PIV and PDA, only flows with low gas volume fractions can generally be considered, as distinguishing between individual bubbles in such cases can become difficult. On the other hand, this method is much less expensive than PIV and PDA. [Boyer et al., 2002]

Using an imaging analysis technique Jianu et al. [2015] mapped the hydrogen bubble size, number, and velocity as the bubbles ascended through the liquid, in an electrolysis process. The obtained data was used to investigate the relations between the flow dynamics and kinetics of mass and heat transfer of the two-phase flow composed of inert gas bubbles and the amount of water entrained by the gas. Christensen and Thomassen [2014] applied a Telecentric Direct Image Method (TDIM), where a telecentric lens, CCD camera and LED background lighting were used to acquire shadow images of bubbles. The captured bubbles appeared as shadows due to the LED background lighting being refracted or reflected at the bubble-liquid interface. The TDIM was validated using polyamid particles with a known mean size of 50 µm. For these particles the TDIM measured a mean size of 58.5 µm with a standard deviation of ±11.5 µm.

THIRD CHAPTER

Problem statement

Having a technology which can be used on-site to produce the necessary disinfectants for water treatment brings several advantages. Transportation, storage and handling of dangerous chemicals can be avoided and the needed clean water is readily obtained. Such a technology is available through the electrochlorination process, which has been studied experimentally for decades. However, the current computational technologies allow a more detailed modelling, with the purpose of obtaining a better and deeper understanding of the phenomena occurring during operation as well as discover and investigate possible optimizations.

Four aspects have been identified to be occurring inside the electrochlorination cell during operation:

- Electrochemistry
- Chemical reactions
- Transport of species
- Two-phase, gas-liquid flow

The purpose of this study is to develop a 2D model capable of predicting the operational behaviour of the electrochlorination cell by taking these four aspects into account. The developed model is subsequently used to investigate the performance of the cell at conditions resembling those used in industrial applications. In order to fulfil this objective, the following approach is applied:

- Application of a reliable measurement method in order to obtain inputs for the developed model as well as to measure parameters in the constructed electrochlorination cell for model validation.
- Development of a model of a single electrochlorination cell including the aspects identified to be occurring during operation.
- Validation of the developed model by comparison with measured parameters of the electrochlorination cell during operation.
- Sensitivity analysis, where the behaviour of the model is analysed for varying inputs.
- Investigations on the performance of the electrochlorination cell at conditions resembling those used in industrial applications.

In order to obtain inputs for the model as well as to measure parameters in the electrochlorination cell during operation for model validation, an experimental setup is assembled. This setup is composed of the constructed small scale electrochlorination cell, depicted in Figure 2.2, and a direct imaging system.

To obtain a comprehensive model, which correctly captures the behaviour of the electrochlorination cell, couplings between the aspects have to be taken into account. Such couplings include among others the generated gas bubbles influencing the access of the electrochemical reactants to the electrode surface.

3.1 Delimitations

The 2D model only considers the cell gap between the electrodes and the top part of the electrochlorination cell located just above these. The bottom part of the electrochlorination cell is not considered due to only a single-phase flow occurring in this part. Thus, the inlet of the cell gap is considered as the inlet of the electrochlorination cell for the modelling. Much of the top part is not considered due to bubble accumulation occurring when considering the whole top part. This bubble accumulation leads to considerable convergence issues due to the relative simple two-phase flow formulation applied in this study. In addition, removing the top part greatly saves computational power and time.

Due to convergence issues the dissociation of water reaction is not taken into account in this study. Disregarding this reaction also means that the hydrogen and hydroxide ions are not kept in balance by the dissociation of water reaction, which in turn results in the inability of evaluating the pH value throughout the electrochlorination cell. As a consequence, the reaction kinetics for considered bulk reactions as well as the equilibrium potentials for the considered electrochemical reactions cannot be made pH dependent. Hence, assumptions for the pH values throughout the electrochlorination cell have to be made, and reaction kinetics as well as equilibrium potentials estimated accordingly.

The electrochemical reactions occurring at the anode and cathode lead to heat transfer between the electrodes and the electrolytic solution. However, for this study it is assumed that this heat transfer is negligible and is therefore not considered in the modelling.

The solution strategy employed for the simulations aims at obtaining a time-dependent solution, due to the fact that the problem in question is highly non-linear and a time-dependent solution results in a better and smoother convergence than a stationary solution. For future work however, the time-dependent solution can be used as a starting point for the stationary problem by using its results as initial guesses, provided that the simulation time is sufficiently long for the problem to converge towards sufficiently steady values.

As the problem is highly non-linear and coupled, a coupled solver should in principle be used. However, applying a coupled solver failed to give a converged solution. These convergence issues have only been alleviated by using a segregated solver where the potential across the electrolytic solution is solved first, followed by the effective gas density as well as pressure and liquid velocity field and lastly, the transport of species.

When operating at high current densities, bubble clouding occurs in the constructed electrochlorination cell and the applied experimental methodologies are not capable of distinguishing between the individual bubbles in this case. Hence, experimental data is only obtained at lower current densities and a large cell gap of 7.68 mm. This means that validation of the model is only done by comparing experimental data to those of the model for a large cell gap. If validated, further investigations are conducted at conditions resembling industrial applications.

3.2 Outline of the report

In the following a short description of the content in each chapter is given. This is summarised in Figure 3.1.

Experimental work is conducted with the purpose of obtaining a mean bubble size to be implemented in the model and for validation purposes, in terms of bubble flow structure and velocities as well as gas volume fractions. Chapter 4 presents detailed descriptions of the methodologies used to obtain these experimental data. Throughout the chapter references are given to appendices describing considerations about the used experimental setup and procedures along with the obtained results and data processing algorithms.

Chapter 5 treats the detailed modelling of the four phenomena identified to be occurring in the electrochlorination cell:

- Electrochemistry
- Chemical reactions
- Transport of species
- Two-phase, gas-liquid flow

The preprogrammed modules used in COMSOL Multiphysics and couplings between modelling aspects are described as well. References are given throughout the chapter to the experimental procedures described in Appendix B.

Chapter 6 describes how the simulations are conducted in COMSOL Multiphysics by solving partial differential equations through the Finite Element Method. The employed solution and numerical stabilisation strategies are presented, together with the used mesh topologies and grid independence analyses for two cell gaps, small (2 mm) and large (7.68 mm). References are given throughout the chapter to the experimental procedures described in Appendix B and the Finite Element Method described in Appendix F.

With the entire system modelled, validation against the obtained experimental data is carried out in Chapter 7 using the model geometry with a large cell gap. Furthermore, a sensitivity analysis is conducted in order to study the behaviour of the model as the inputs are varied.

Chapter 8 presents the numerical investigations conducted using the small cell gap geometry, where flow structures, hypochlorite output, overpotentials and current densities are analysed.

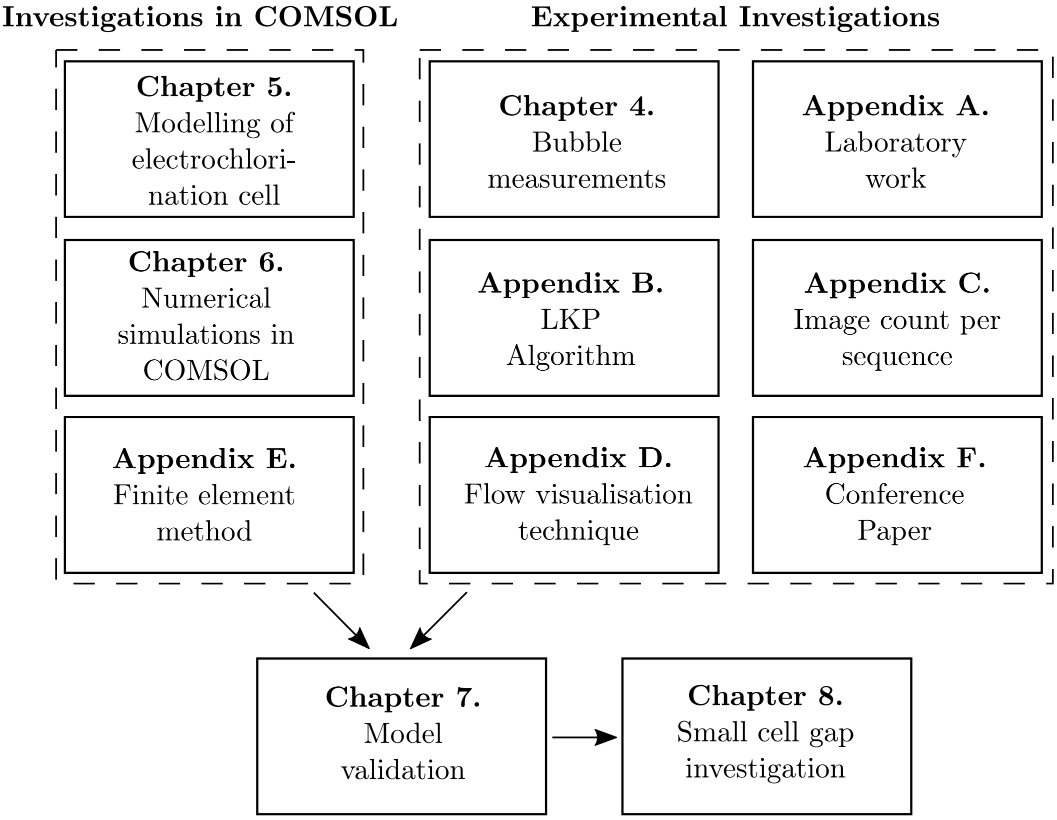

Figure 3.1. Report overview.

Fourth Chapter

Bubble measurements

This chapter describes the investigations related to the measurement of bubble size and velocity, and gas volume fraction. This information will be used as input to the model or as reference data for validation of the model described in Chapter 5.

The bubble measurements are acquired using a Telecentric Direct Image Method (TDIM) with which the wanted parameters can be measured directly in shadow images of the bubbles. These shadow images are created by positioning a light source behind the bubbly flow such that the light is reflected or refracted at the bubble-liquid interface, thus making these appear as dark, filled contours on a light background when photographed with a telecentric lens. If the bubbles are perfect in focus, a light spot will be visible in the centre of the bubble where the background light passes straight through the bubble, as seen in Figure 4.1.

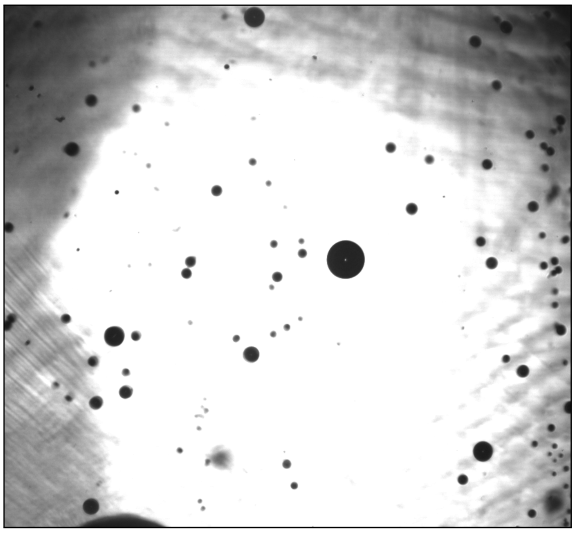

Figure 4.1. Preliminary bubble shadow image with a bubble in perfect focus.

In the following the laboratory work is referenced as Tasks (A) and (B):

(A) Determination of the mean bubble size and averaged local gas volume fraction.
(B) Determination of the mean bubble velocity for different bubble size groups.

where both Tasks (A) and (B) are performed at multiple horizontal positions in the cell.

Note that the original purpose of Task (A) was to determine the bubble size as function of the current density, but this was found to be impossible due to limitations of the applied methodology. Thus, it was chosen to repurpose some of the data to estimate a single mean bubble size. More information on the above is found in Appendix B.

The following Sections 4.2 and 4.4, and parts of Section 4.3 are based on the Conference Paper (Appendix A) and describes how the bubble shadow images are captured for each task as well as the subsequent processing procedure.

4.1 The experimental setup

The following introduces the experimental setup used for the TDIM measurements and describes the choices made with respect to positioning of the image plane and lighting. The experimental setup is shown Figure 4.2.

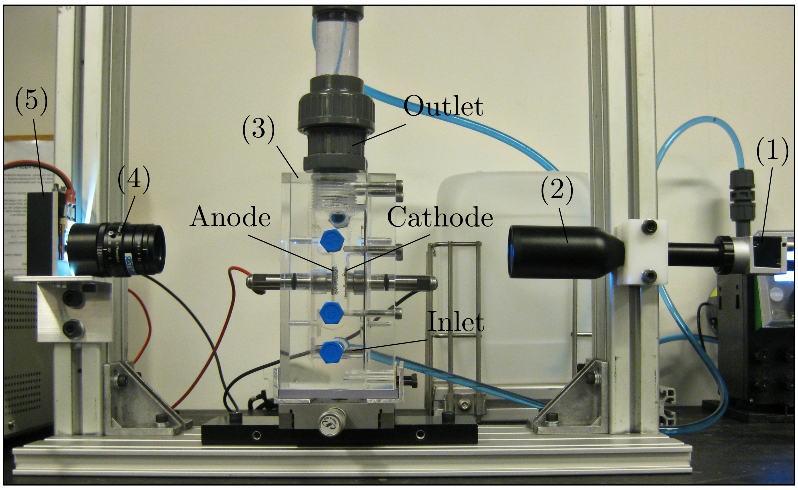

(1)	Digital camera	(3)	Electrochlorination cell	(5)	LED and heat sink
(2)	Telecentric lens	(4)	Lens for the LED		

Figure 4.2. Experimental setup used for TDIM.

As seen in Figure 4.2 the TDIM setup consists of three overall parts.

- The image capture consists of a digital camera (1) and a telecentric lens (2).
- The electrochlorination cell (3) in which the bubbly flow of interest occurs.
- The background lighting consists of a lens (4) and a LED (5).

All of the above is mounted on a stable aluminium frame which makes it possible to adjust the position of the Field of View (FOV) by moving the cell instead of having to reposition the camera and lighting.

Preliminary tests showed that when applying current densities of more than about $5\,\mathrm{mA/cm^2}$ resulted in the cell becoming very clouded with bubbles which would block the background light, thus making the bubbles appear as one large black mass on the shadow images. Thus, it was chosen to only operate the cell at current densities below $5\,\mathrm{mA/cm^2}$, where a significant gas bubble evolution occurs at the cathode but virtually no bubbles flow from the anode. Therefore, focus was set on acquiring measurements at the cathode.

It was originally intended to capture the images of the bubbles in the cell gap by positioning the FOV perpendicular to the cathode and thus having the camera look along the cathode. However, this proved problematic as the gas bubbles produced on the electrode surfaces stays in a narrow plane very close to the electrodes after detachment. This means that, with the FOV positioned perpendicular to the electrodes, the camera focuses into a very dense mass of bubbles thus making it impossible to distinguish individual bubbles from each other in the resulting images. This dense mass of bubbles furthermore made it difficult to obtain an acceptable background lighting because the bubbles furthest away from the lens would block the background light before it reached the bubbles in focus. Finally, the gas bubbles had a tendency to stick to the inner wall of the plexiglass housing and, thus completely blocking the view of the bubbles.

To circumvent the problems described in the above, it was chosen to position the FOV above the cathode and in the plane the bubbles move in, as it is seen in Figure 4.2. Because of the thin bubble plane, due to the spreading of the gas bubbles occurring above the cathode, this viewing angle made it much easier to obtain images with clearly distinguishable bubbles.

With respect to the background lighting, preliminary tests showed that it was necessary to have precise control of the background lighting as a too intense background light would result in the smaller bubbles becoming unclear or completely disappear, as can be seen in Figure 4.1. Therefore, it was chosen to use a combination of an LED and a optic lens as this makes it possible to control the intensity as well as the focus of the background lighting. During image capture, the LED was operated at approximately 2 V and 1.2 A, and the lens was set at a focusing range of 0.3 m and $f/6$. This produced somewhat dark images but ensured that small bubbles would not disappear due to overexposure.

The positioning of the camera, lighting and FOV relative to the cell, is illustrated in Figure 4.3 and dimensional specifications are given in Table 4.1.

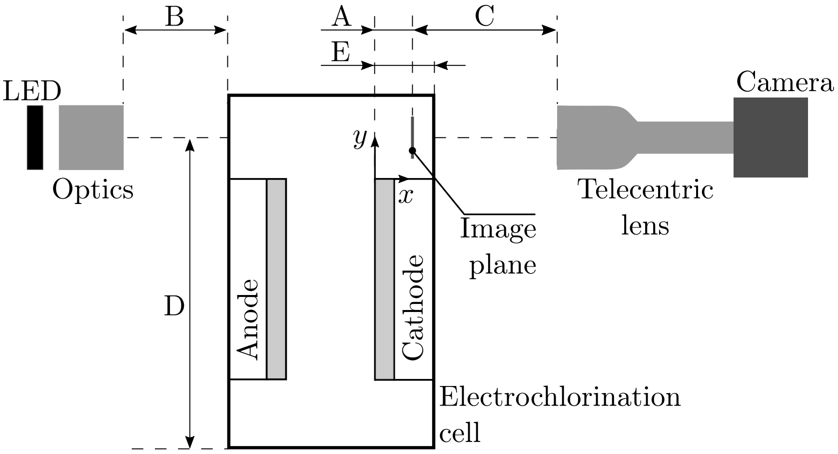

Figure 4.3. Conceptual drawing of the experimental setup. This drawing is not to scale.

Table 4.1. Dimensional specifications for the experimental setup.

	Description	Dimensions [mm]	
		Task (A)	Task (B)
A	Length between cathode plane and FOV	−0.77–4.65	1.65–4.57
B	Length from the outer cell wall to the lighting optics	131.6–137	131.6–134.5
C	Length from the FOV to the telecentric lens housing	120	120
D	Vertical position of the telecentric lens and lighting	106	106
E	Length between cathode plane and the inner cell wall	16.16	16.16

Note that throughout this and the following chapters the horizontal positioning of the FOV is given as the normalised horizontal position A/E, hereafter referred to as horizontal position (A/E). For Task (A) the normalised horizontal positions were A/E $= -0.046$, -0.016, 0.016, 0.048, 0.079, 0.099, 0.16, 0.22 and 0.28. For Task (B) the normalised horizontal positions were A/E $=$ 0.10, 0.16, 0.22 and 0.28. The operational conditions during image capture are listed in Table 4.2.

Table 4.2. Operational conditions for the electrochlorination cell during image capture. This drawing is not to scale.

		Task (A)	Task (B)
Salt concentration	[g/L]	30	30
Current density	[mA/cm^2]	1.25, 2.5, 3.75, 5.0	2.5
Cell voltage	[V]	2.6-2.9	2.66
Flow	[L/h]	2.0	2.0

A description of the advantages of using a telecentric lens, as well as laboratory procedures and specifications for the applied equipment are found in Appendix B.

4.2 Digital image capture

The experimental setup described above and procedure described in the Conference Paper were used to capture the shadow images for the determination of bubble size and gas volume fraction, Task (A). A series of 100 images were captured for each combination of current density and normalised horizontal position of the FOV, and a dead time of 10 s was applied between the capture of each image to ensure that no bubbles appear in the data set multiple times.

Moreover, the same experimental setup was applied to capture shadow images for the determination of the mean bubble velocity for different bubble size groups, i.e. Task (B). However, preliminary experiments showed that the maximum capture speed of 30 fps of the Basler acA1300-30um camera used for Task (A) was too slow, and consistent tracking of the captured bubbles could not be achieved as the captured bubbles moved too much from one image to the next. Hence, for Task (B), 100 sequences each consisting of 15 images were captured sequentially at 4 different horizontal positions above the cathode at a frame rate of 150 fps using a Basler acA1920-155um.

From Figure 4.3 it is furthermore important to note that the images for Task (B) are taken from the right side, as shown in Figure 4.3, and hence capture bubbles in the zy-plane while the model operates in the xy-plane. Thus, the y-component of the bubble velocity predicted by the model and the velocity y-component estimated from the images of Task (B) will be comparable. However, the bubble velocity magnitude estimated through Task (B) will be different from the bubble velocity magnitude predicted by the model, because the horizontal components are different.

The determination of the necessary number of images per sequence for Task (B) is described in Appendix C.

4.3 Methodology for image processing

The methodology employed to determine bubble sizes and velocities from the captured bubble shadow images is illustrated in Figure 4.4.

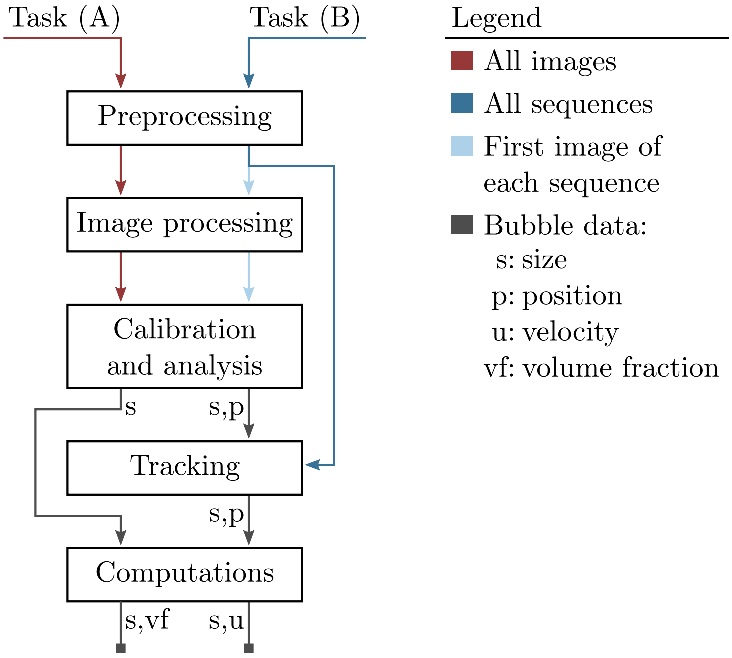

Figure 4.4. Flow diagram representing the processing procedure employed for the determination of bubble size at varying current densities, and the mean bubble velocity for different bubble size groups.

The preprocessing and image processing stages have the purpose of enabling the use of the particle analysis tools implemented in the Vision toolbox in LabVIEW in order to acquire precise measurements of the captured gas bubbles. These processing stages include the following:

- Preprocessing in MATLAB: background removal, image normalisation and contrast enhancement.
- Image processing in LabVIEW: edge detection, thresholding, fill closed edges and object filtering.

Note that all captured images for Task (A) undergo the three first stages; preprocessing, image processing, and calibration and analysis. However, all the image sequences for Task (B) are forwarded directly from the preprocessing to the tracking step, while copies of the first image of each sequence continue through the image processing, as well as calibration and analysis, as indicated in Figure 4.4.

The calibration and analysis stage involves a conversion from pixels to SI units. Furthermore, the images are analysed and bubble sizes are recorded and saved. These bubble data are then forwarded to the computations stage where the local gas volume fraction is computed. This concludes the processing performed for Task (A); however, the positions of each bubble are also recorded during the analysis and forwarded to the tracking stage, in the case of Task (B).

The tracking stage determines the final positions of each bubble. This is done by tracking the bubbles through their respective sequences, using the bubble positions recorded from the first image of each sequence as initial positions for the tracking algorithm. The final positions are then forwarded, together with the initial positions from the analysis stage, to the final computations stage where the displacements and velocities of each bubble are computed.

The following, Section 4.4, describes the preprocessing, image processing, and calibration and analysis stages in detail as well as the verification of the methodology. The tracking and velocity estimation stages are described in Section 4.5 and the estimation of the averaged local gas volume fraction is covered in Section 4.6. The measurement results are presented throughout the report, as needed, whereas raw results are presented in Appendix B.3. The MATLAB scripts and LabVIEW programs used for the image processing and tracking are found on the CD attached in Appendix H.

4.4 Digital image processing for bubble size determination

The following is inspired by the work of [Christensen and Thomassen, 2014].

An example of a typical bubble shadow image is shown in Figure 4.5. In the following, Figure 4.5 is used as a reference image and the bubbles denoted by A, B and C are used as reference bubbles to illustrate the effects of the image processing. Bubbles A and B are both in focus and are relatively large and small, respectively. Bubble C is not completely in focus and is thus an example of a bubble which is to be kept out of the final data set.

Note that Figure 4.5 as well as the other examples throughout Section 4.4 are taken from Task (A). However, the procedure is the same for Task (B), with the exception that the image sequences for Task (B) contain large black borders which are cropped out before the preprocessing to decrease the time necessary for image processing and bubble tracking. This is illustrated in Figure 4.6, where everything outside the rectangle is cropped out.

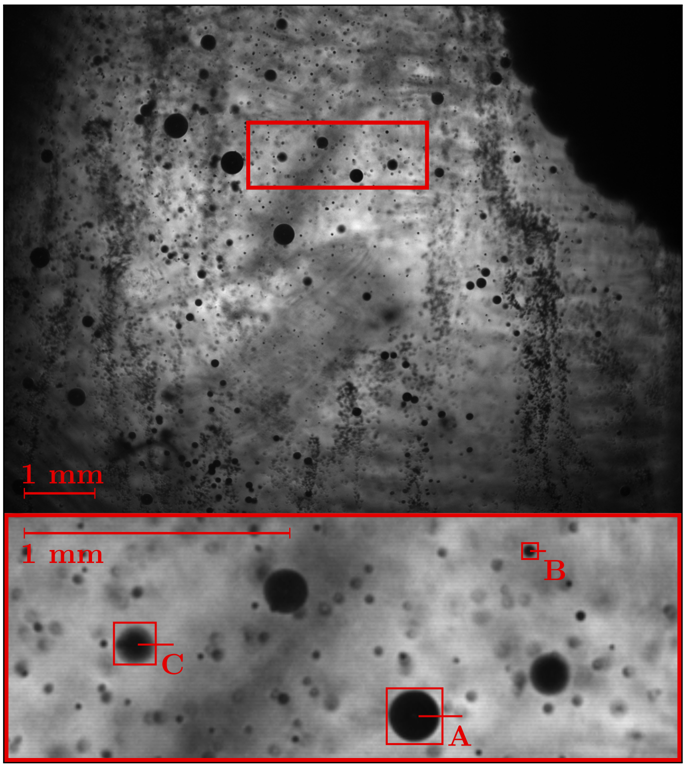

Figure 4.5. Unprocessed reference bubble shadow image from Task (A).

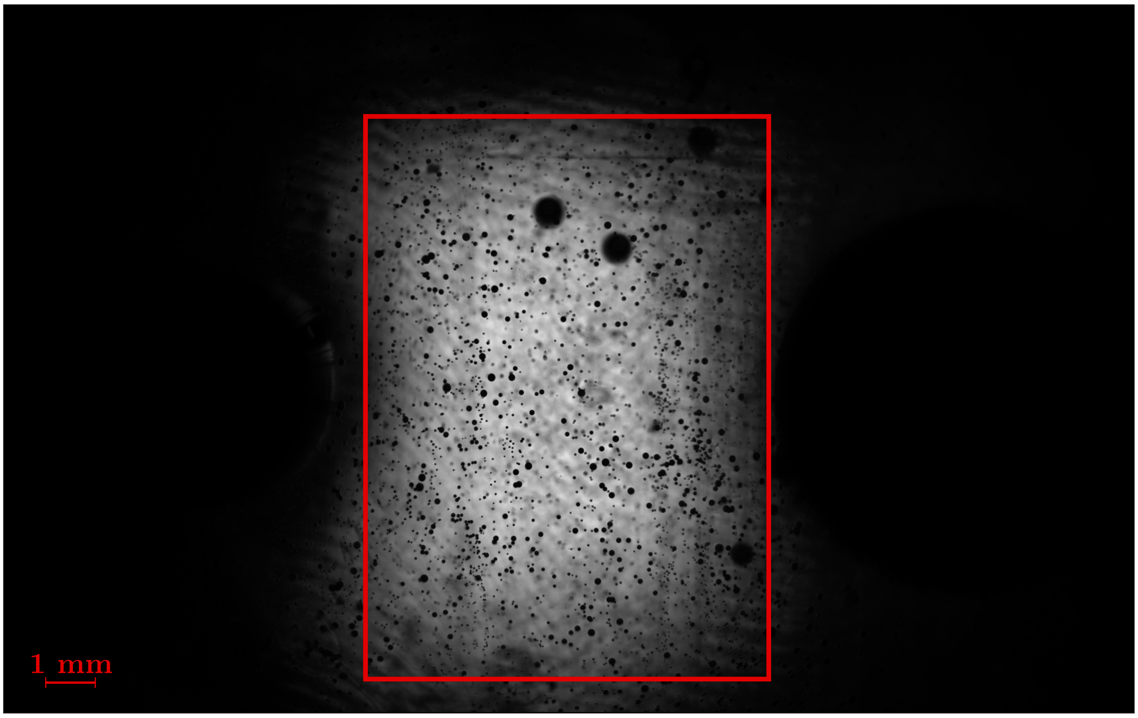

Figure 4.6. Unprocessed example image from Task (B). Everything outside the rectangle is cropped out before the preprocessing to decrease the time required for image processing and bubble tracking.

4.4.1 Pre-processing in MATLAB

From Figure 4.5 it is seen that the background is very uneven due to the spot effect created by the background lighting in the centre portion of the image and the streaky texture in the bottom half of the image, which results from tool marks created inside the electrochlorination cell during manufacturing.

The main purpose of the image preprocessing is to ease the main image processing in LabVIEW by removing these background effects and otherwise enhance the quality of the image such that the dark bubble contours in the foreground stand out from the background as much as possible.

Note that in the following, unless specified otherwise, all images are cast as doubles in MATLAB. Hence, the images have greyscale values going from 0 to 1.

The first preprocessing step is to cancel out the background of the image by dividing the original image I_0, pixel by pixel, with an averaged background image $\bar{I}_{BG}$ as shown in Equation (4.1). The averaged background image $\bar{I}_{BG}$ is created by computing the average of 50 images which have been captured sequentially with the background lighting turned on and the electrochlorination cell turned off. The resulting averaged background image is shown in Figure 4.7.

$$I_f(x,y) = \frac{I_0(x,y)}{\bar{I}_{BG}(x,y)} \qquad \text{if } I_f(x,y) > 1 \text{ then } I_f(x,y) = 1 \tag{4.1}$$

where:			
	I_f	Foreground image matrix (without background)	[−]
	I_0	Original unprocessed image matrix	[−]
	$\bar{I}_{BG}$	Averaged background image matrix	[−]

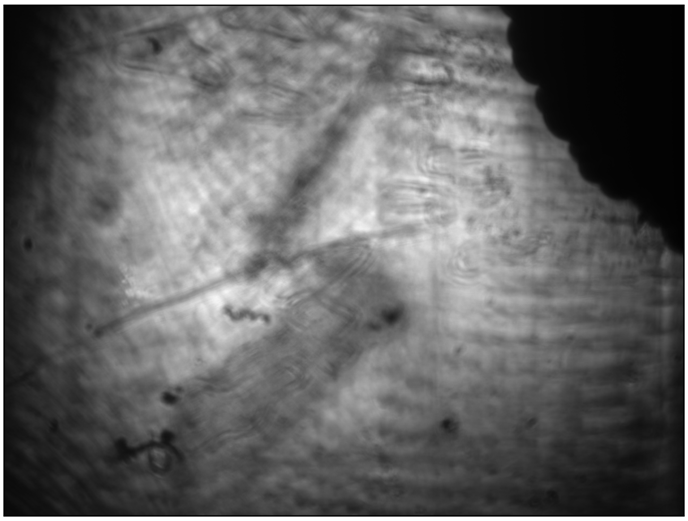

Figure 4.7. Averaged background image, $\bar{I}_{BG}$. Created using 50 images which are captured sequentially with the cell turned off and the background lighting turned on.

Regarding Equation (4.1), it should be noted that in areas at the image border where $\bar{I}_{BG}$ is black the image has a greyscale value of 0, hence, the result of Equation (4.1) goes to infinity. This is not a problem in terms of the resulting image I_f as this area will turn out to be white in I_f as wanted. However, it constitutes a problem when trying to normalise the image as the above results in division by infinity. This problem is circumvented by finding all elements of I_f which are larger than one and setting these equal to one, as shown in Equation (4.1).

The second preprocessing step is the normalisation of I_f, Equation (4.2), which stretches the image such that more of the greyscale spectrum is utilized. This ensures a greyscale range of 0 to 1, which is required by the contrast enhancement operation in the following preprocessing step.

$$I_n(x,y) = \frac{I_f(x,y) - \min(I_f)}{\max(I_f) - \min(I_f)} \tag{4.2}$$

where: I_n | Normalised foreground image matrix [−]

The third preprocessing step is contrast enhancement. For the purpose of this study, it has been chosen to apply the non-linear intensifier operation given in Equation (4.3) [Chaira and Ray, 2010]. This operation transforms the greyscale levels of the normalised image I_n such that greyscale values larger than 0.5 increase and greyscale values smaller than 0.5 decrease. That is, dark areas are darkened and light areas are lightened [Chaira and Ray, 2010]. This essentially creates a steeper greyscale gradient between the bubble contours and the background, thereby improving the conditions for precise edge detection. Figure 4.8 shows a plot of the intensifier operation for a greyscale range from 0 to 1.

$$I_c(x,y) = \begin{cases} 2 \cdot [I_n(x,y)]^2 & \text{for } 0.0 \leq I_n \leq 0.5 \\ 1 - 2 \cdot [1 - I_n(x,y)]^2 & \text{for } 0.5 < I_n \leq 1.0 \end{cases} \tag{4.3}$$

where: I_c | Contrast enhanced foreground image matrix [−]

Finally, the images are converted back into unsigned 8-bit integers and saved as image files ready for import into LabVIEW for further processing. Figure 4.9 shows the preprocessed version of the reference image, Figure 4.5.

Comparing Figures 4.5 and 4.9 shows that the image preprocessing has completely removed the spot light and tool mark effects from the image. The grey unclear patches left in Figure 4.9 are groups of bubbles which are completely out of focus and hence will be filtered out by the further processing in LabVIEW. Furthermore, it is noted that any fuzzy bubble edges have been preserved from Figure 4.5 to Figure 4.9.

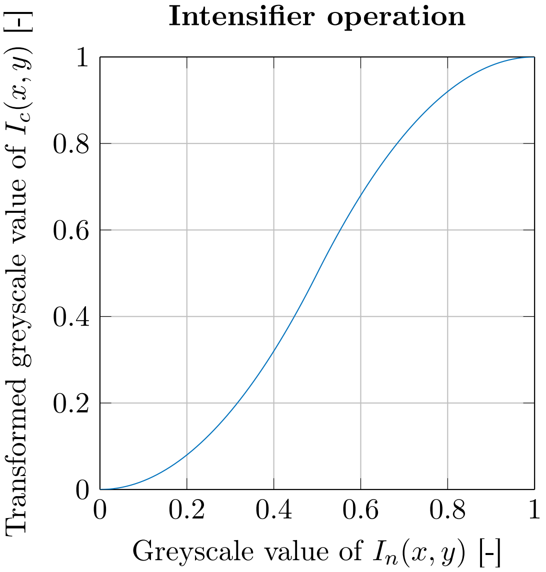

Figure 4.8. The non-linear intensifier applied for contrast enhancement. Inspired by Chaira and Ray [2010].

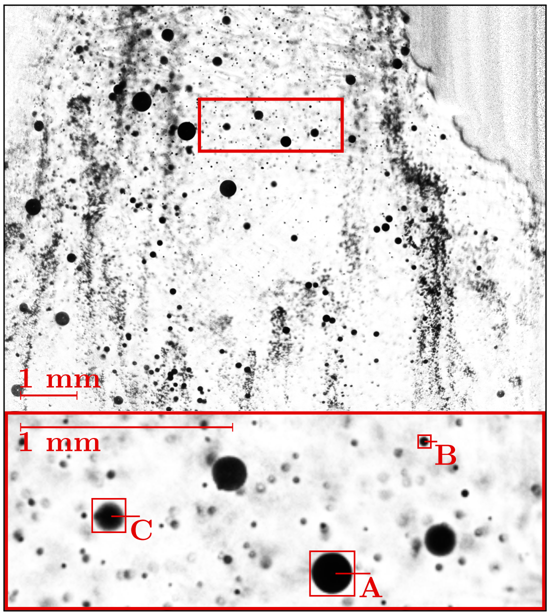

Figure 4.9. Reference bubble shadow image, Figure 4.5, after preprocessing.

The greyscale line profiles for bubble A, B and C are plotted in Figure 4.10 for the original image, Figure 4.5, as well as for each of the preprocessing steps.

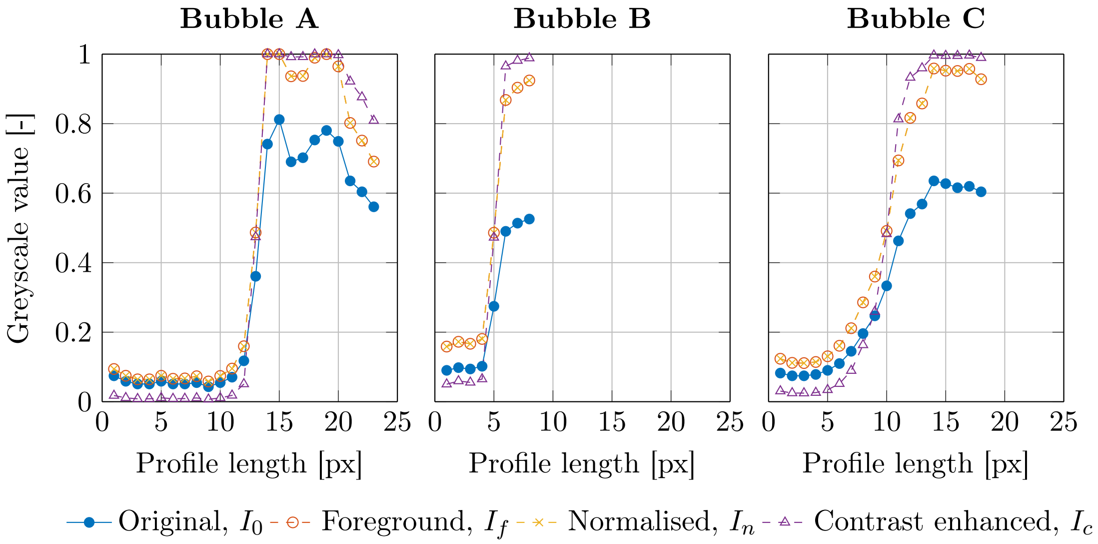

Figure 4.10. Greyscale line profiles across the right edges of reference bubbles A, B and C after preprocessing.

From Figure 4.10 it is seen that the preprocessing generally has the most effect on the lighter midtones which constitutes the streaky texture and the spot light effect in the background of the original unprocessed image, Figure 4.5. Comparing greyscale profiles for I_0 and I_f it is seen that the background division mainly affects the background around the bubbles. The reasoning for this is seen from Equation (4.1). Inside the bubbles the numerator is either zero or close to zero and thus, the division with the corresponding background pixels has very little effect. However, around the bubbles where I_0 and $\bar{I}_{BG}$ have similar greyscale values the result of Equation (4.1) goes towards one. Thus, the greyscale value increases from I_0 to I_f in these areas, which lightens the dark background areas greatly and negates the background effects created by the lighting and tool marks.

In addition, Figure 4.10 shows that the normalisation between I_f and I_n has little to no effect, which indicates that I_f already employed the entire greyscale range in this case. The contrast enhancement, from I_n to I_c has darkened the bubble contours and lightened the background in all three cases as intended.

The reference image is shown in Figure 4.11 for each of the preprocessing step.

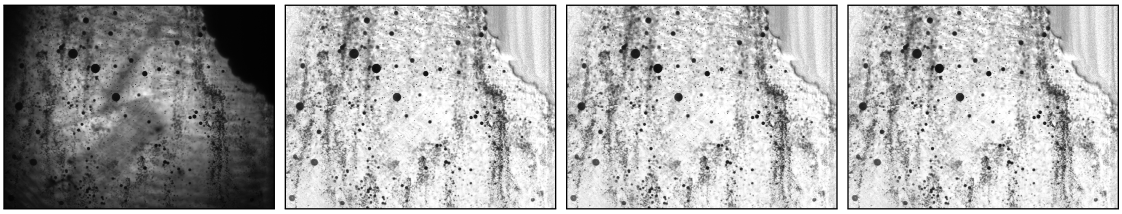

(a) Original, I_0 ***(b)*** Foreground, I_f ***(c)*** Normalised, I_n ***(d)*** Contrast enh., I_c

Figure 4.11. Reference bubble shadow image at each of the preprocessing steps.

The following section describes the main processing performed in LabVIEW.

4.4.2 Image processing in LabVIEW

The purpose of the image processing in LabVIEW is to remove bubble contours which would skew the measurements. This includes bubbles which are out of focus or bubble contours with incomplete edges. Moreover, it has been chosen to remove overlapping bubbles from the images as it has not been possible to find a consistent method for dividing these without breaking their edges and other bubble contours.

The image processing steps performed in LabVIEW are:

- Edge detection
- Thresholding
- Fill closed edges
- Object filtering
    - Removal of border objects
    - Removal of unwanted objects

The image processing exploits the fact that the edge detection and thresholding leave bubbles which are in focus as closed outlines while the outlines of bubbles out of focus are broken up. These broken outlines are then removed using binary morphology and an equivalent ellipse axis ratio filter. The complete outlines of bubbles in focus are filled and analysed to determine size and shape.

The choice of filters and settings for each of the above mentioned processing steps are described in the following.

Edge detection and thresholding

Edge detection treats the subject of finding intensity change, that is a gradient in the greyscale value, in the image [National Instruments, 2015b]. The Vision toolbox in LabVIEW includes a number of different edge detection filters which are all able to extract and outline the bubble contours in the preprocessed images. The outline created by the filters is depending on the local sharpness, or the local greyscale gradient, of the given bubble contour [National Instruments, 2015b]. This means that a bubble which is in focus, and thus has a sharp edge, results in a light outline, and a bubble which is out of focus, and thus has a soft edge, results in a darker, smudged or even incomplete outline. Thus, bubbles in focus can easily be separated from bubbles out of focus using a threshold.

The edge detection filters which have been found relevant for this study are:

- Differentiation
- Prewitt
- Sobel
- Roberts

Each of these filters is applied to Figure 4.9 and the greyscale line profiles for bubbles A, B and C are plotted in Figure 4.12.

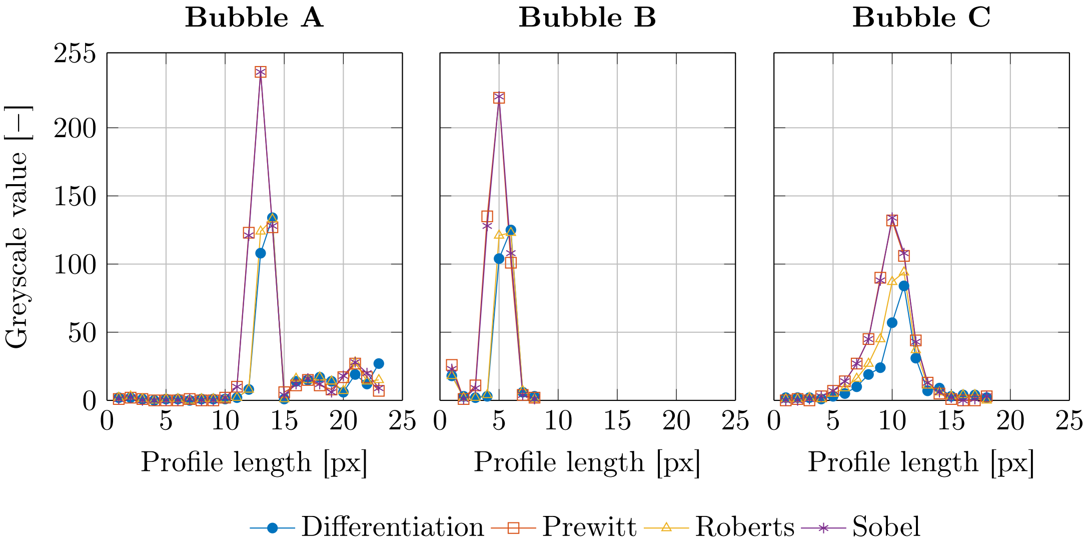

Figure 4.12. Greyscale line profiles across the right edges of reference bubbles A, B and C illustrating the effect of the different edge detection filters.

From Figure 4.12 it is seen that the Differentiation and Roberts filters, and Prewitt and Sobel filters result in virtually the same outlines. Prewitt and Sobel produce the brightest outlines with widths of approximately 3 pixels while the Differentiation and Roberts filters produce somewhat darker outlines with widths of approximately 2 pixels. For bubble C, Figure 4.12 shows lower greyscale values and thicker outlines for all filters compared to bubbles A and B. This is expected as bubble C is out of focus and hence has a smaller greyscale gradient along its edge compared to bubbles A and B, as can be seen in Figure 4.10. Finally, Figure 4.12 shows that the Prewitt and Sobel filters peak approximately one pixel further to the left, that is closer to the centre of the bubble, compared to the other edge detection filters.

As noted above, the outlines of in focus bubbles are thresholded, filled and then analysed to determine the size and shape of the bubble. Hence, depending on the applied threshold, the measured bubble size may include the added thickness of the edge detection outline. In order to investigate this further, it is chosen to apply thresholding to the images which have undergone edge detection with the Prewitt and Roberts filters and thereby determine how much the edge detection filters add to the measured bubble widths. For the Prewitt edge detection filter it is chosen to apply the threshold at a greyscale values of 115. A threshold at a greyscale value of 80 is applied in the case of Roberts filter as a result of the lower peaks seen for this filter in Figure 4.12. Close-ups of reference bubbles A, B and C after edge detection and thresholding are shown in Figures 4.13 and 4.14. Furthermore, close-ups taken from the original unprocessed image, Figure 4.5, are shown in Figure 4.15 for reference. It should be noted that the outline of bubble C is incomplete and hence not suitable for size measurements. Bubble C is included in Figures 4.13 to 4.15 to provide a reference for how an out of focus bubble appears after the edge detection and thresholding.

Comparing the outlines of bubble A across Figures 4.13 and 4.14 it is seen that both the Prewitt and Roberts filters produce outlines of 1 to 3 px, however the top, bottom, left and right edges, which define the measured width and height of the bubbles, are seen to be about 1 px thinner with the Roberts filter compared to the Prewitt filter, as one would expect from Figure 4.12. It is furthermore seen that both widths and heights of 28 px and 27 px are measured with the application of the Prewitt and Roberts filters, respectively.

Comparing the outlines of bubble B across Figures 4.13 and 4.14 show tendencies similar to those seen for bubble A. However, widths of 7 px are found for both the Prewitt and Roberts filters while the height is found to be 8 px with the Prewitt filter compared to 7 px for the Roberts filter.

Comparing the above mentioned size estimates to Figure 4.15 it is assessed that the Roberts and Prewitt edge detection filters add 1 px and 2 px, respectively, to the actual bubble size. For large bubbles this added size would be negligible. However, in the case of small bubbles in the order of 30 µm, which are expected to occur in the electrochlorination cell, the addition of a few extra pixels will provide a significant difference between the measured and actual bubble size. In order to minimise this error it is chosen to use the Roberts edge detection filter combined with a threshold of 80 for the final image processing.

Furthermore, it should be noted that the Roberts edge detection filter works by highlighting pixels where variation in intensity occurs along the diagonal axis [National Instruments, 2015c]. Hence, the pixel added to the height and width of the bubble will be added on the left and bottom edges of the bubble contours. Consequently, all measurements of bubble width and height will be corrected by subtracting 1 px from the original measurements.

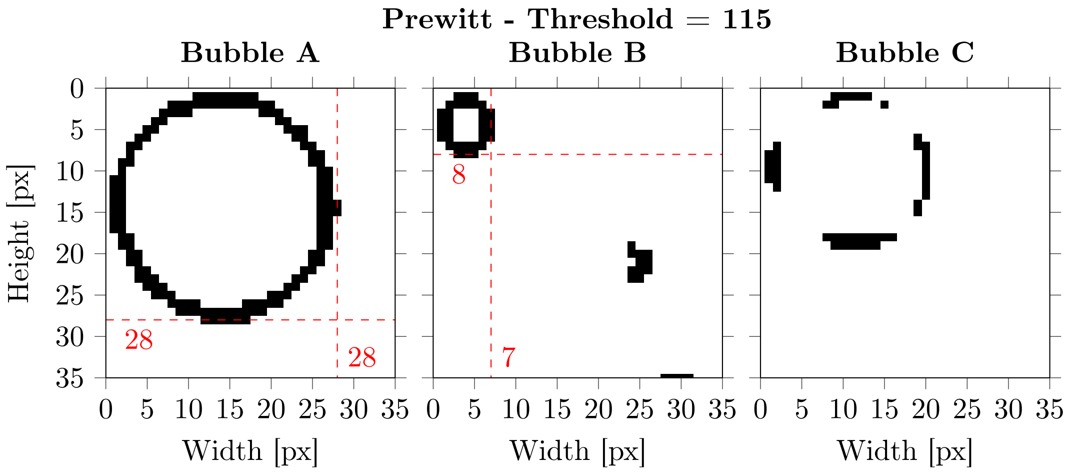

Figure 4.13. Close-ups of reference bubbles A, B and C after application of the Prewitt edge detection filter and a threshold of 115.

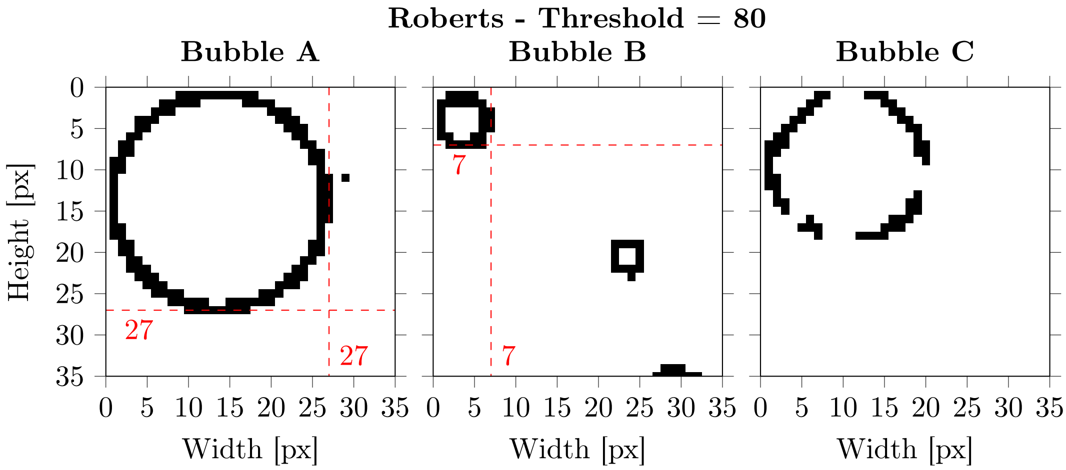

Figure 4.14. Close-ups of reference bubbles A, B and C after application of the Roberts edge detection filter and a threshold of 80.

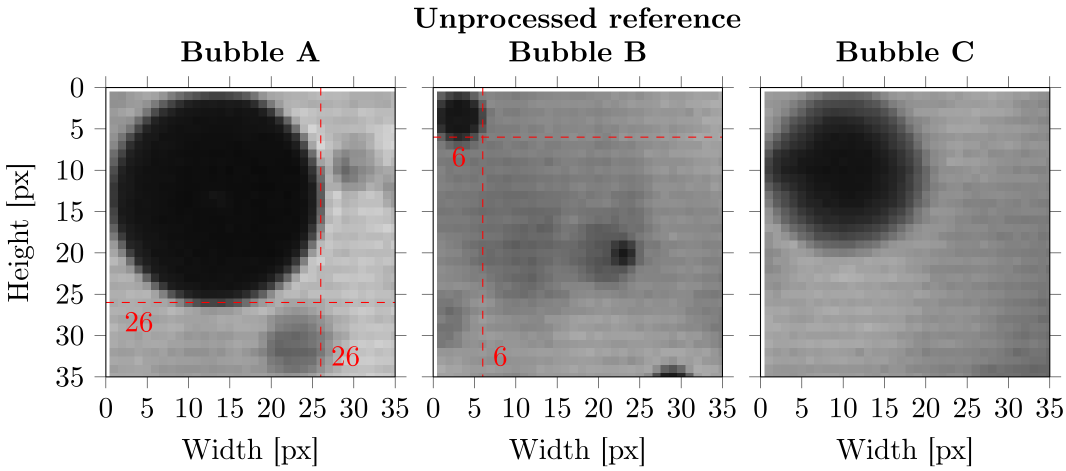

Figure 4.15. Close-ups of unprocessed reference bubbles A, B and C.

Fill closed edges

After edge detection and thresholding, the images undergo binary morphology operation which finds the closed contours resulting from in focus bubbles and sets the pixel values within these contours to 1 (the background is now black). This operation is required as it makes it possible to remove the broken edges left over from out of focus bubbles without affecting the, now filled, contours of in focus bubbles. The effects of the edge detection, thresholding and filling of edges operations are illustrated in Figure 4.16.

Object filtering

The final steps of the image processing in LabVIEW are the removal of contour edges from unwanted bubbles. The first of these processing step is a binary morphology operation that removes contours touching the borders of the image. Then the broken edges left from the edge detection and thresholding as well as overlapping bubbles are removed using a Equivalent Ellipse Axis Ratio (EEAR) filter. The equivalent ellipse is the ellipse with the same area and perimeter as the bubble contour.

The EEAR is defined mathematically in Equation (4.4) [National Instruments, 2015d].

$$\mathrm{EEAR} = \frac{E_{2a}}{E_{2b}} + \frac{a}{b} \tag{4.4}$$

where:			
	E_{2a}	Equivalent ellipse major axis	[px]
	E_{2b}	Equivalent ellipse minor axis	[px]
	a	Equivalent ellipse semi-major axis, $2a = E_{2a}$	[px]
	b	Equivalent ellipse semi-minor axis, $2b = E_{2b}$	[px]

The semi-major and -minor axes are determined using the definitions of the area and perimeter of the equivalent ellipse given in Equations (4.5) and (4.6), respectively.

$$A_{EE} = \pi ab \tag{4.5}$$

$$P_{EE} = \pi\sqrt{2 \cdot (a^2 + b^2)} \tag{4.6}$$

where:			
	A_{EE}	Equivalent ellipse area	[px^2]
	P_{EE}	Equivalent ellipse perimeter	[px]

From Equation (4.4), it is seen that the more the equivalent ellipse resembles a circle the closer the EEAR is to 1. Hence, the broken edges and overlapping bubbles, which are far from being circular, can be removed by applying a EEAR filter which only keeps objects with an EEAR between 0 and 1.5. Finally, one last binary morphology operation is applied to remove any residue left over by the EEAR particle filter. The effects of the filtering operations are illustrated in Figure 4.17.

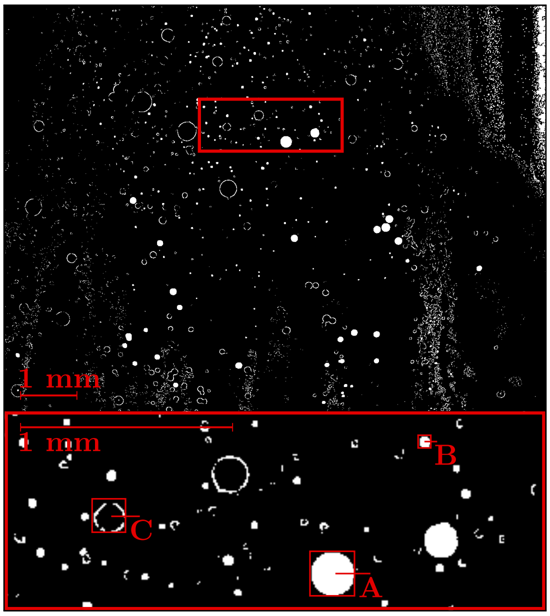

Figure 4.16. Reference image, Figure 4.5, after edge detection, thresholding and filling of closed contours.

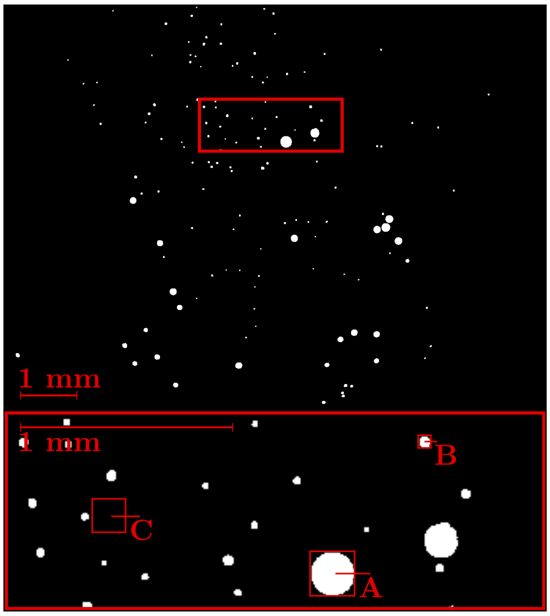

Figure 4.17. Reference image, Figure 4.5, after ended image processing in LabVIEW.

Common for the three binary morphology operations, as well as for the EEAR filter, is that all of these are applied with a connectivity of 8. When the Vision toolbox in LabVIEW processes a binary image, the intensity of each pixel in the image is analysed and the pixels are grouped into "particles" based on the found intensity levels. This is the method the software employs to determine which pixels in the image are part of a bubble and which are not. The connectivity has two possible settings, 4 and 8, which determines whether the diagonal neighbouring pixels are considered in the pixel grouping, as illustrated in Figure 4.18. The choice of connectivity-8 is made to improve the conditions for correctly identifying thin edges in the images.

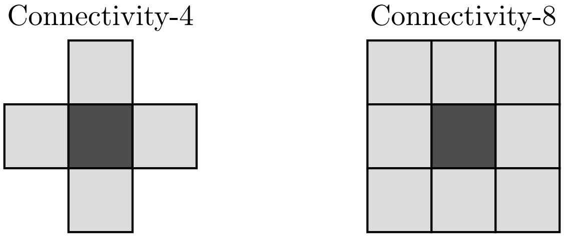

Figure 4.18. Illustration of the neighbouring pixels considered with connectivities of 4 and 8. Inspired by [National Instruments, 2015a].

In the following section the calibration and particle analysis steps are described.

4.4.3 Calibration and particle analysis in LabVIEW

In the above it has been explained how the bubble shadow images are processed such that these are ready for analysis. However, it is necessary to convert the acquired measurements from pixels to micrometers, as well as correct any distortions or perspective errors.

As described in Appendix B, the applied telecentric lens has a zero angular FOV, meaning that the light captured in the focus plane travels straight into the lens. Furthermore, the camera and cell are fixed on an aluminium frame such that the camera is positioned at a perpendicular angle with respect to the nearest cell wall. Hence, the light captured by the image sensor passes through the plexiglass wall along the surface normal. Applying Snell's law, as shown in Equation (4.7) and Figure 4.19, it is seen that due to the perpendicular path of the light, the angle of incidence is zero and hence the angle of refraction is zero. Consequently, no distortion of the image occurs as a result of light refractions in the water-to-plexiglass or plexiglass-to-air interfaces, assuming planar surfaces. It could be argued that the surfaces are not planar as a result of tool marks on the plexiglass housing, as seen in Figure 4.7. However, it is chosen to neglect the presence of tool marks in this context, as neither the preliminary measurements nor the method verification for the Conference Paper (Appendix A) gave any indication that these tool marks have any significant influence on the measurements.

$$\sin(\theta_A) \cdot n_A = \sin(\theta_B) \cdot n_B, \qquad n_A \wedge n_B \neq 0 \tag{4.7}$$

where:			
	θ_A	Angle of incidence	[°]
	θ_B	Angle of refraction	[°]
	$n_A,\ n_B$	Refractive indices for medium A and B, respectively	[−]

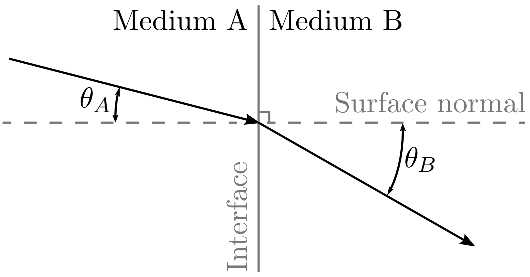

Figure 4.19. Illustration of the refraction of light across an interface between media of different refractive indices. Inspired by [Wolfson, 2012].

The fact that there are no distortions reduces the calibration to a simple unit conversion from pixels to micrometers. For the purpose of this study, the conversions from pixels to micrometres are performed using the known image resolutions and pixel sizes of the cameras as well as the primary magnification of the applied lens, as shown in Equations (4.8a) and (4.8b).

$$\mathrm{FOV}_h = \frac{I_{res,h} \cdot S_{px,h}}{\mathrm{PMAG}} \tag{4.8a}$$

$$\mathrm{FOV}_v = \frac{\mathrm{FOV}_h}{\mathrm{AR}} \tag{4.8b}$$

where:			
	FOV	Field of view	[µm]
	I_{res}	Image resolution	[px]
	S_{px}	Sensor pixel size	[µm]
	PMAG	Primary magnification of the lens	[−]
	AR	Aspect ratio, AR = $\mathrm{FOV}_h/\mathrm{FOV}_v$	[−]
	$v,\ h$	Denotes vertical and horizontal components, respectively	

The resulting FOVs as well as the information needed for the computations are listed in Table 4.3 for both camera and lens configurations A and B.

Table 4.3. List of information necessary for the computation of the conversion ratio between pixels and micrometers for camera and lens configurations A and B [Basler, 2016a,b; Edmund Optics, 2015a].

		Configuration A	Configuration B
Camera		Basler acA1300-30um	Basler acA1920-155um
Telecentric lens		Edmund Optics 63-729	Edmund Optics 63-729
Magnification, PMAG	[−]	0.5	0.5
Image resolution, I_{res}	(h × v) [px]	1280 × 960	1920 × 1200
Aspect ratio, AR	[-]	4:3	16:10
Sensor pixel size, S_{px}	(h × v) [µm]	3.75 × 3.75	5.86 × 5.86
Field of view, FOV	(h × v) [µm]	9600 × 7200	22502 × 14064
Pixel size	(h × v) [µm]	7.50 × 7.50	11.72 × 11.72

After the calibration, the images are analysed using the particle analysis tool in the NI Vision toolbox. From the analysis the following information is extracted:

- Boundary rectangle width: Used to approximate the bubble diameter.
- Centre of mass: Used as initial position for bubble tracking.

Note that the use of the boundary rectangle width as approximation for the diameter assumes circular bubbles. An assumption which was confirmed in the Conference Paper (Appendix A), where the same experimental setup were used to measure bubble diameters at 1.9 mA/cm^2, 2.6 V and a NaCl concentration of 30 g/L.

In the following, the methodology for bubble size measurements is verified using measurements of particles with a known mean size.

4.4.4 Methodology verification

For camera and lens configuration A, it was shown in the Conference Paper that processing 100 shadow images of polyamid particles, with a known mean size of 50 µm, suspended in water resulted in a mean size estimate of 49.7 µm with a confidence interval of ±0.9 µm. Conclusively, the methodology is suitable for bubble size measurements, since the known mean falls within the statistical uncertainty of the estimated mean.

Similar measurements have been conducted for camera and lens configuration B to investigate to what extent the increased pixel size (see Table 4.3) influences the resulting size estimates. Again, 100 images were captured using the methodology described in Section 4.2, resulting in 890 recognised and measured particles. The resulting size distribution is shown in Figure 4.20.

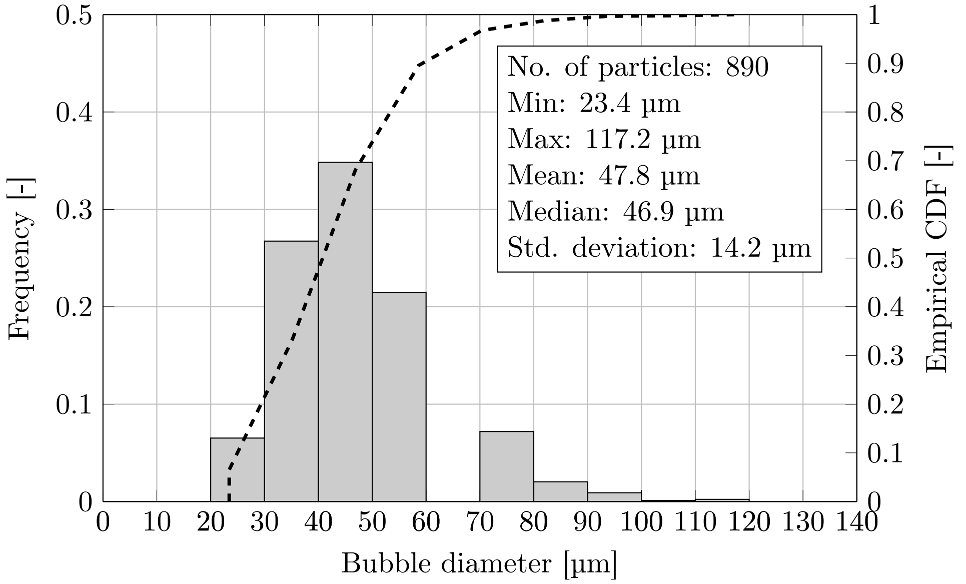

Figure 4.20. Normalised size distribution of polyamid particles measured using TDIM with camera and lens configuration B.

The resulting mean estimate of 47.8 µm, with a confidence interval of ±0.7 µm is in sufficient agreement with the known mean size of 50 µm. However, this estimate is not as precise as the estimate obtained for camera and lens configuration A, which is expected considering the lower spatial resolution which results from the increased pixel size of camera and lens configuration B compared to lens and camera configuration A. Based on the above, it is assessed that lens and camera configuration B is suitable for bubble size measurements. The slightly lower precision of lens and camera configuration B compared to lens and camera configuration A is considered to be of minor importance, as the size measurements conducted with configuration B have the purpose of classifying the bubbles into size groups.

4.5 Bubble tracking and velocity estimation

The purpose of the bubble tracking is to track individual bubbles through each image sequence to obtain pairs of initial and final bubble positions. These position pairs are then used to determine the displacement and velocity of each bubble when knowing the frame rate.

The bubble tracking procedure, illustrated in Figure 4.21, works as follows. The procedure is started and the first sequence is initialised by setting the *previous* and *current* images, $I_{s,i-1}$ and $I_{s,i}$, as the first and second images in the first image sequence, respectively. These images as well as the previously obtained bubble positions, $\boldsymbol{P}_{s,i-1}$ for $I_{s,i-1}$ are then loaded and fed to the tracking algorithm which determines the corresponding bubble positions in the current image and saves these to the current array of bubble positions $\boldsymbol{P}_{s,i}$.

A test is then conducted to determine whether the final image in the current sequence has been reached. If this is not the case ($i < i_{max}$), the current image $I_{s,i}$ and the current array of bubble positions $\boldsymbol{P}_{s,i}$ are redefined as the previous image $I_{s,i-1}$ and the previous array of bubble positions $\boldsymbol{P}_{s,i-1}$, respectively, the image counter i is increased by one and the next iteration of the inner loop is conducted to get bubble positions for image $I_{0,2}$.

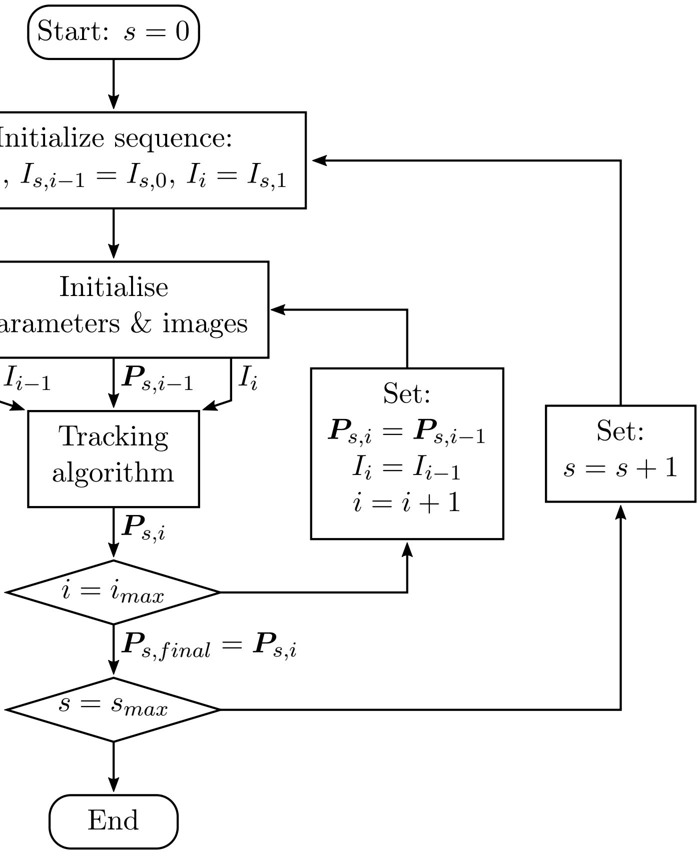

Figure 4.21. Flow diagram representing the bubble tracking procedure.

The inner loop continues until the last image in the current sequence has been reached, at which point $i = i_{max}$, and the current array of bubble positions $\boldsymbol{P}_{s,i}$ is saved as the final positions for the current sequence $\boldsymbol{P}_{s,final}$. Then a test is conducted to determine whether the last sequence has been reached. If this is not the case ($s < s_{max}$), the sequence counter s is increased by one and the outer loop starts over with the next sequence.

The applied feature tracking algorithm is a pyramid-based Lucas and Kanade (LKP) algorithm embedded in LabVIEW. A detailed description of this algorithm is beyond the scope of this text. However, a description of the basic concepts behind the algorithm are given in Appendix D.

4.5.1 Potential problems with the bubble tracking

Preliminary testing of the tracking procedure revealed two problems, both related to the LKP algorithm loosing track of some of the bubbles which are to be tracked:

1. Large and fast moving bubbles push the tracking algorithm off smaller bubbles.
2. Bubbles move out of the image frame during tracking.

Item 1 is illustrated in Figure 4.22, which shows three images from the tenth sequence of the test series conducted for the investigation of the sufficient image count per sequence described in Appendix C. The images have been overlaid with green circular markers which indicate the objects being tracked by the LKP algorithm. From the images of Figure 4.22, it is seen how the tracking algorithm is pushed off a number of small bubbles as a result of a larger and faster moving bubble.

From Figures 4.22b and 4.22c it is furthermore noted that the pushed tracking markers are positioned in white areas while the other markers are centred on the dark bubbles. This is exploited to negate Item 1 by recording the greyscale pixel value at the final position of each bubble to be tracked. Every point in the data set which is found to have a greyscale value of more than 200, and thus position in a white spot, is then removed from the data set.

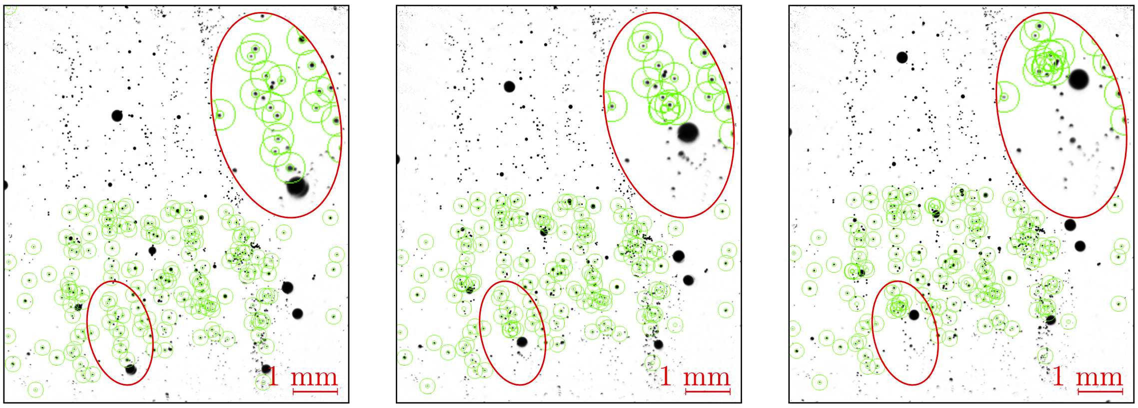

(a) Image: 1. ***(b)*** Image: 5. ***(c)*** Image: 9.

Figure 4.22. Example of how the tracking algorithm can be pushed off track by large and fast moving bubbles. The images are taken from the tenth sequence of the test series acquired for the investigation in Appendix C. The image number in the subcaption of each image denotes the order of the images within that sequence.

As for Item 2, the LKP algorithm returns a NaN value when the object being tracked moves out of the image frame or alternatively the tracker will in the case of the smaller bubbles wrongly jump to another bubble and hence introduce errors into the data set. To avoid this, the algorithm is limited to only consider bubbles in the lower half of the image, as seen in Figure 4.22a, as these are much less likely to move out of the image frame during tracking. Furthermore, any NaN values in the set of final positions are combined with a pixel value of 255 and are thus removed together with the problematic bubbles of Item 1.

4.5.2 Bubble velocity estimation

The initial and final bubble positions are given as coordinate sets in the yz-plane and thus the displacement y-component of each bubble is determined as shown in Equation (4.9). Note that the coordinates are in pixels and thus the displacement is multiplied with the pixel size (see Table 4.3) to convert the displacement into micrometres.

$$\Delta S_{b,y} = (\text{Pixel Size}) \cdot (y_f - y_i) \tag{4.9}$$

where:		
$\Delta S_{b,y}$	Bubble displacement y-component	[µm]
y	Bubble y-coordinates	[px]
i, f	Denote initial and final coordinates, respectively	

Knowing the displacement components, the mean y and z velocity components of each bubble during tracking are estimated as the displacement divided by the time difference between the first and last image of each sequence. The time difference is determined as the number of images in each sequence divided by the frame rate, as indicated in Equation (4.10).

$$\bar{v} = \frac{\Delta S_{b,y}}{\Delta t} = \frac{\Delta S_{b,y} \cdot fps}{n_{img}} \tag{4.10}$$

where:		
$\bar{v}$	Average bubble y-velocity component	[µm/s]
Δt	Time between first and last image of each sequence	[s]
fps	Frames per second. Here $fps = 150$	[s^{-1}]
n_{img}	Number of images per sequence. Here $n_{img} = 15$	[−]

The following section treats the estimation of the averaged local gas volume fraction.

4.6 Estimation of the local gas volume fraction

As stated in Table B.3 in Appendix B the applied lens has a field of depth of ±1.9 mm. Thus, the lens creates a volume in which the bubbles are in focus. Knowing the bubble size, the above can be used to estimate an averaged local gas volume fraction from the images captured for Task (A).

The averaged local gas volume fraction at each horizontal position is determined using Equation (4.11).

$$\bar{\phi}_{g,i} = \frac{\bar{V\!\!\!\!-}_{g,i}}{V\!\!\!\!-_{img}} \tag{4.11}$$

where:		
$\bar{\phi}_{g,i}$	Averaged local gas volume fraction at the i^{th} position	[−]
$\bar{V\!\!\!\!-}_{g,i}$	Average gas volume at the i^{th} position	[µm^3]
$V\!\!\!\!-_{img}$	Image volume	[µm^3]

The average gas volume at a given horizontal position, $\bar{V\!\!\!\!-}_{g,i}$, is determined by computing the volume of each bubble in each image, assuming spherical bubbles, and summing up to obtain the total gas volume in each image. This is repeated for each image at the given horizontal position and the result is used to find the average gas volume fraction across all images at the given position. The average gas volume is expressed in Equation (4.12).

$$\bar{V}_{g,i} = \frac{\sum_{j=1}^{n_{img}} \sum_{k=1}^{n_{b,j,i}} \left(\frac{\pi}{6} d_{b,k,j,i}^{3} \right)}{n_{img}} \tag{4.12}$$

where:	$n_{b,j,i}$	Number of bubbles in the j^{th} image at the i^{th} position	[−]
	$d_{b,k,j,i}$	Diameter of the k^{th} bubble in the j^{th} image at the i^{th} position	[µm]

The image volume is determined as shown in Equation (4.13).

$$V_{img} = \text{FOV}_h \cdot \text{FOV}_v \cdot \text{FOD} \tag{4.13}$$

where:	FOD	Field of Depth for the applied lens. Here FOD $= 3.8 \times 10^3$ µm

4.7 Summary

This chapter dealt with the method employed for capturing the bubbles evolved at the cathode and computations made to obtain data that can characterize the gas bubbles. The captured images were used for bubble mean size determination and to compute gas volume fractions as well as bubble velocity estimation. The experimental setup, equipment configurations and the applied methodology of direct imaging were presented. The methodology included two steps which prepared the images for further analysis - pre-processing and processing. The processing procedures were conducted in MATLAB and LabVIEW. The velocity estimations were done by relating bubble displacements within image sequences to time. The volume fraction determination of the gas bubbles made use of the bubble size distributions and the FOD of the lens. The methodology proved to be reliable, after a verification was applied on particles of known size, which showed consistency with the expected results.

In the following Chapter 5, the modelling of the phenomena occurring in the electrochlorination cell is described.

FIFTH CHAPTER

Modelling of the electrochlorination cell

This chapter serves to describe the applied theory, assumptions, and choices made during the modelling of the electrochlorination cell. The following aspects are considered:

- Electrochemistry
- Chemical reactions
- Transport of species
- Two-phase, gas-liquid flow

First, the electrochemistry is described in Section 5.1, followed by descriptions of the chemical reactions, the transport of species and the two-phase, gas-liquid flow, in Sections 5.2 to 5.4. Finally, an overview of the couplings between the different modelling aspects is given in Section 5.5.

5.1 Modelling of electrochemistry

This section serves to describe the equations which govern the electrochemistry, the assumptions used to model the electrochemistry in this study, and finally the electrochemical reactions, electrode kinetics and kinetics data.

5.1.1 Governing equations of electrochemistry

For a solution in an electrochemical cell a current occurs due to the motion of charged species. The motion, and hence the molar flux, of dissolved species in an electrolytic solution is given by Nernst-Planck equation. This is given by Equation (5.1) [Newman, 1991].

$$\boldsymbol{N}_i'' = -\underbrace{D_i \nabla c_i}_{\text{diffusion}} - \underbrace{z_i u_{m,i} F c_i \nabla \Phi_l}_{\text{migration}} + \underbrace{c_i \boldsymbol{u}}_{\text{convection}} \tag{5.1}$$

where:			
	$\boldsymbol{N}_i''$	Molar flux of species i	[mol/(m^2 s)]
	D_i	Diffusion coefficient of species i	[m^2/s]
	c_i	Concentration of ion i	[mol/m^3]
	z_i	Valence of species i	[−]
	$u_{m,i}$	Mobility of species i	[(s mol)/kg]
	F	Faraday's constant	[C/mol]
	Φ_l	Electrolytic solution potential	[V]
	$\boldsymbol{u}$	Velocity vector, $\boldsymbol{u} = (u, v)$	[m/s]

The mobility of species i can be determined by the Nernst-Einstein relation, which is given in Equation (5.2).

$$u_{m,i} = \frac{D_i}{\mathcal{R}T} \tag{5.2}$$

where:			
	$\mathcal{R}$	Ideal gas constant	[J/(mol K)]
	T	Temperature	[K]

Nernst-Planck equation, Equation (5.1), states that a molar flux can occur due to a concentration gradient in the electrolytic solution (Diffusion), charged species and a potential gradient across the solution (Migration), and forced flow of the electrolytic solution (Convection). The current density occurring in the electrolytic solution, due to this molar flux, is given by Equation (5.3) [Newman, 1991].

$$\boldsymbol{i}_l = F \sum_i z_i \boldsymbol{N}_i'' \tag{5.3}$$

where:			
	$\boldsymbol{i}_l$	Current density in the electrolytic solution	[A/m^2]

Here $z_i F$ is the charge per mole for a species, also called the charge density. By combining Equations (5.1) and (5.3) the current density in the electrolytic solution can be expressed as in Equation (5.4) [Newman, 1991].

$$\boldsymbol{i}_l = -F \sum_i z_i D_i \nabla c_i - F^2 \nabla \Phi_l \sum_i {z_i}^2 u_{m,i} c_i + F \boldsymbol{u} \sum_i z_i c_i \tag{5.4}$$

Equation (5.4) shows that a current density occurs in the electrolytic solution with nonzero charge density due to a concentration gradient, a potential gradient, and forced flow of the electrolytic solution [Newman, 1991].

There is conservation of mass and since the current density in the electrolytic solution is due to molar fluxes of charged species, conservation of charge is ensured as well [Newman, 1991]. Conservation of charge is given by Equation (5.5).

$$\nabla \bullet \boldsymbol{i}_l = 0 \tag{5.5}$$

In the following the assumptions for modelling the electrochemistry in the electrolytic solution are described.

5.1.2 Assumptions for electrochemistry modelling

It is assumed that the electrolytic solution is electrically neutral. Hence, the electrolytic solution is assumed to be uncharged everywhere in the electrochlorination cell at any time. This assumption is valid in all solutions except very close to the electrodes, due to the double charge layer, and other boundaries [Newman, 1991]. Thus, the sum of the product of the valence and the concentration of every species equals zero everywhere in the electrolytic solution. This is given by Equation (5.6).

$$\sum_i z_i c_i = 0 \tag{5.6}$$

Using Equation (5.6) means that the convective contribution on the right side of Equation (5.4) equals zero. Hence, the forced flow of an electrolytic solution with no charge density does not result in any current density contribution [Newman, 1991].

Concentration gradients are expected to be occurring close to the electrodes due to the electrochemical reactions taking place. Without any forced flow such gradients are expected to be quite significant. However, due to the forced flow considered in this study these concentration gradients are assumed to have negligible influence. This is given by Equation (5.7).

$$\nabla c_i = 0 \tag{5.7}$$

Hence, the diffusive contribution on the right side of Equation (5.4) equals zero. By using these assumptions Equation (5.4) reduces to Equation (5.8) [Newman, 1991].

$$\boldsymbol{i}_l = -F^2 \nabla \Phi_l \sum_i {z_i}^2 u_{m,i} c_i \tag{5.8}$$

Equation (5.8) states that a current density only occurs in the electrolytic solution due to a potential gradient and charged species. The conductivity of the electrolytic solution is given by Equation (5.9) [Newman, 1991].

$$\sigma = F^2 \sum_i {z_i}^2 u_{m,i} c_i \tag{5.9}$$

where: σ | Electrical conductivity of the electrolytic solution [S/m]

Substituting Equation (5.9) into Equation (5.8) means that an Ohm's Law type expression is obtained, as shown in Equation (5.10) [Newman, 1991].

$$\boldsymbol{i}_l = -\sigma \nabla \Phi_l \tag{5.10}$$

In order to account for the volume occupied by the gas bubbles next to the electrodes, and hence, influencing the electrochemical reactions and thereby the current densities, Equation (5.10) is multiplied by the volume fraction of the electrolytic solution, shown in Equation (5.11).

$$\phi_l \boldsymbol{i}_l = -\phi_l \sigma \nabla \Phi_l \tag{5.11}$$

where: ϕ_l | Volume fraction of electrolytic solution [−]

Thus, by calling the volume fraction of the electrolytic solution from the two-phase flow aspect a coupling is ensured. Since it is assumed that there are no concentration gradients in the electrolytic solution the electrical conductivity can be assumed to be constant. Therefore, by knowing the amount of salt added to the solution the electrical conductivity can be determined. In Appendix B it is stated that 30 g of salt is added for every 1 L of water. Hence, the electrical conductivity of the electrolytic solution is 4.2 S/m [National Physical Laboratory, 2015].

In the following the electrochemical reactions, electrode kinetics and kinetics data are described.

5.1.3 Electrochemical reactions, electrode kinetics, and kinetics data

Four electrode reactions are taken into account [C.Y. Cheng, 2007]; Reactions (C 5.1) and (C 5.2) occur at the anode, while Reactions (C 5.3) and (C 5.4) occur at the cathode.

$$2\,\mathrm{Cl^-} \longrightarrow \mathrm{Cl_2} + 2\,\mathrm{e^-} \qquad \text{(Anode)} \qquad \text{(C 5.1)}$$

$$2\,\mathrm{H_2O} \longrightarrow \mathrm{O_2} + 4\,\mathrm{H^+} + 4\,\mathrm{e^-} \qquad \text{(Anode)} \qquad \text{(C 5.2)}$$

$$2\,\mathrm{H_2O} + 2\,\mathrm{e^-} \longrightarrow \mathrm{H_2} + 2\,\mathrm{OH^-} \qquad \text{(Cathode)} \qquad \text{(C 5.3)}$$

$$\mathrm{OCl^-} + \mathrm{H_2O} + 2\,\mathrm{e^-} \longrightarrow \mathrm{Cl^-} + 2\,\mathrm{OH^-} \qquad \text{(Cathode)} \qquad \text{(C 5.4)}$$

Each of the reactions contribute with a local current density. Hence, the current density normal to the electrode is determined as the sum of all the local current densities for the reactions occurring at the given electrode, as shown in Equation (5.12) [Newman, 1991].

$$\boldsymbol{i}_l \bullet \boldsymbol{n} = \sum_m i_{loc,m} \qquad (5.12)$$

where:			
	$i_{loc,m}$	Local current density for the m'th electrode reaction occurring at the given electrode	[A/m^2]
	$\boldsymbol{n}$	Normal vector to the boundary surface	[–]

The local current density due to a reaction occurring at the surface of the electrode can be determined using the Butler-Volmer equation [Newman, 1991]. This is given by Equation (5.13).

$$i_{loc,m} = i_{0,m}\left[k_{R,m}\exp\left(\frac{\alpha_{a,m}F\eta_m}{\mathcal{R}T}\right) - k_{O,m}\exp\left(\frac{-\alpha_{c,m}F\eta_m}{\mathcal{R}T}\right)\right] \qquad (5.13)$$

where:			
	$i_{0,m}$	Exchange current density for the m^{th} reaction	[A/m^2]
	$\alpha_{a,m}$	Anodic transfer coefficient for the m^{th} reaction	[–]
	$\alpha_{c,m}$	Cathodic transfer coefficient for the m^{th} reaction	[–]
	$k_{R,m}$	Reduced species coefficient for the m^{th} reaction	[–]
	$k_{O,m}$	Oxidized species coefficient for the m^{th} reaction	[–]
	η_m	Activation overpotential for the m^{th} reaction	[V]
	T	Temperature	[K]
	$\mathcal{R}$	Universal gas constant	[J/(mol K)]

The Butler-Volmer equation is analogous to the expression for the rate of a heterogeneous reaction not involving any electrochemistry. The first exponential term can thus be seen as the forward rate term, anodic process, and the second exponential term as the reverse rate term, cathodic process. Equation (5.13) shows that the local current density for a reaction occurring at the surface of the electrode depends on the activation overpotential [Newman, 1991]. The activation overpotential accounts for the additional energy required by Reactions (C 5.1) to (C 5.4) for transferring electrons between the electrode and the electrolytic solution [Péra et al., 2013]. Thus, this can be seen as the activation energy required for the reactions to take place at the electrodes. The activation overpotential is defined as the difference between the electrode potential, the potential at the interface between the electrode and electrolytic solution, and equilibrium potential for the given reaction [Newman, 1991]. This is given by Equation (5.14).

$$\eta_m = \Phi_s - \Phi_l - E_{eq,m} \tag{5.14}$$

where:		
Φ_s	Electrode potential. Here $\Phi_{anode} = 3\,\mathrm{V} \wedge \Phi_{cathode} = 0\,\mathrm{V}$	[V]
$E_{eq,m}$	Equilibrium potential for the m'th reaction	[V]

Reactions occurring at the same electrode share the same potential of the electrolytic solution at the interface between the electrode and electrolytic solution. The equilibrium potential of every reaction is generally dependent on the pH value of the electrolytic solution close to the electrode surface. However, for pH values of 2 and 12 at the anode and cathode, respectively, C.Y. Cheng [2007] has shown that the equilibrium potentials only vary slightly from the values at a pH value of 7. Thus, it is assumed that the equilibrium potentials are independent of the pH value of the electrolytic solution. This means that there should be a fixed difference, given by the differences in equilibrium potentials, between the overpotentials for the reactions occurring at the same electrode. Table 5.1 lists the constant equilibrium potentials for Reactions (C 5.1) to (C 5.4).

Table 5.1. List of equilibrium potentials applied in the modelling of the electrochemistry [A.J. Bard and L.R. Faulkner, 2002; Black and Veatch Corporation, 2010].

Reaction	(C 5.1)	(C 5.2)	(C 5.3)	(C 5.4)
$E_{eq,m}$ [V]	1.36	1.23	-0.83	0.88

Returning to Equation (5.13), it is concentration dependent ($k_{R,m}$ and $k_{O,m}$) in order to ensure that a reaction does not occur if the species are not actually present at the given electrode. This ensures a coupling to the transport of species aspect from which the concentration of participating species is called and evaluated at the electrode surface. For the reactions occurring at the anode, Reactions (C 5.1) and (C 5.2), it is assumed that the species produced in the anodic process do not limit the current density, $k_{O,m} = 1$. The same is assumed for the reactions at the cathode, Reactions (C 5.3) and (C 5.4), in the cathodic process, $k_{R,m} = 1$.

For the electrolytic solution, 30 g of salt are dissolved in 1 L of water. Since the amount of salt is less than 10% of the amount of water it is considered to be a dilute electrolytic solution. Consequently, there is abundance of water compared to the other species in the electrolytic solution. It is therefore assumed that water is always present at the electrodes for Reactions (C 5.2) and (C 5.3) to occur in the anodic and cathodic processes, respectively. Due to these assumptions, Equation (5.13) reduces to the traditional Butler-Volmer equation ($k_{R,m} = k_{O,m} = 1$) for Reactions (C 5.2) and (C 5.3).

In order for Reaction (C 5.1) to occur chloride ions have to be present at the anode. Thus, to ensure that this requirement is upheld Reaction (C 5.1) is made concentration dependent in the anodic process. This concentration dependency is done by evaluating the concentration of chloride ions at the anode surface to that in the bulk flow. At the same time for Reaction (C 5.4) to occur hypochlorite has to be present at the cathode. The concentration dependency is done by evaluating the concentration of hypochlorite at the cathode surface to a reference concentration of $1\,\mathrm{mol/m^3}$. Hence, Reaction (C 5.4) is made concentration dependent in the cathodic process. Equation (5.15) and Equation (5.16) show the concentration dependency in the anodic and cathodic processes for Reactions (C 5.1) to (C 5.4).

$$k_{R,m} = \begin{cases} \dfrac{c_{\mathrm{Cl^-},s}}{c_{\mathrm{Cl^-},\infty}} & \text{for Reaction (C 5.1)} \\ 1 & \text{for Reactions (C 5.2), (C 5.3) and (C 5.4)} \end{cases} \tag{5.15}$$

$$k_{O,m} = \begin{cases} 1 & \text{for Reactions (C 5.1), (C 5.2) and (C 5.3)} \\ \dfrac{c_{\mathrm{OCl^-},s}}{1\,\mathrm{mol/m^3}} & \text{for Reaction (C 5.4)} \end{cases} \tag{5.16}$$

where:			
	$c_{\mathrm{Cl^-},s}$	Concentration of chloride ions at the anode surface	$[\mathrm{mol/m^3}]$
	$c_{\mathrm{OCl^-},s}$	Concentration of hypochlorite at the cathode surface	$[\mathrm{mol/m^3}]$
	$c_{\mathrm{Cl^-},\infty}$	Concentration of chloride ions in the bulk flow	$[\mathrm{mol/m^3}]$

Again returning to Equation (5.13), it is seen that this depends on the anodic and cathodic transfer coefficients. By knowing the Tafel slope for the given reaction the transfer coefficients in the anodic and cathodic processes can be determined [Newman, 1991]. Note that Equations (5.17a) and (5.17b) usually are defined for Tafel slopes using the natural logarithm. Thus, a correction coefficient, $k_{\log}$, has been added to account for Tafel slopes which are defined using the common logarithm.

$$\alpha_{c,m} = k_{\log}\left(\frac{\mathcal{R}T}{n_{\mathrm{e^-},m}F\gamma_m}\right) \qquad k_{\log} = \begin{cases} 1.0 & \text{for the natural logarithm} \\ 2.3 & \text{for the common logarithm} \end{cases} \tag{5.17a}$$

$$\alpha_{a,m} = 1 - \alpha_{c,m} \tag{5.17b}$$

where:			
	γ_m	Tafel slope for the m'th reaction	[V/decade]
	$n_{\mathrm{e^-},m}$	Number of participating electrons in the rate determining step of the m'th reaction. Here $n_{\mathrm{e^-},m} = 1$ in all cases.	[−]
	$k_{\log}$	Correction coefficient	[−]

Equation (5.17a) is applicable for an elementary one-electron transfer step involving the simultaneous release or uptake of one electron by the electrode, $n_m = 1$ [Guldelli et al., 2014]. The release or uptake of more than one electron is highly improbable and is therefore not considered to be occurring in this case [Guldelli et al., 2014].

The applied Tafel slopes and correction coefficients as well as the resulting anodic and cathodic transfer coefficients and the exchange current densities for the considered electrochemical reactions are listed in Table 5.2.

Table 5.2. List of computed anodic and cathodic tranfer coefficients as well as Tafel slopes and exchange current densities for the considered electrochemical reactions. Note: *Natural logarithm and *Common logarithm.

Reaction	α_a [−]	α_c [−]	γ_m [V/decade]	$k_{\log}$ [−]	i_0 [A/m^2]	
(C 5.1)	0.63	0.37	0.040	1.0*	1	[C.Y. Cheng, 2007]
(C 5.2)	0.63	0.37	0.040	1.0*	10^{-2}	[Gaur et al., 1994]
(C 5.3)	0.18	0.82	0.140	1.0*	10^{-6}	[Couper et al., 1990]
(C 5.4)	0.56	0.44	0.103	2.3*	10^{-10}	[Wu, 1987]

In the following the modelling of the chemical reactions occurring in the electrolytic solution is described.

5.2 Modelling of chemical reactions

As seen in Chapter 5.1 two electrochemical reactions take place at each of the two electrodes. The species formed at the electrodes travel into the electrolytic solution where new reactions take place. The products of these reactions react further within the electrolytic solution, producing, amongst others, the desired hypochlorite, OCl^-, used for disinfecting purposes.

First the chemical reactions considered to be occurring in the electrolytic solution are described and then kinetics data for the reactions are described.

5.2.1 Chemical reactions occurring in the electrolytic solution

The chlorine produced at the anode diffuses away from the electrode and into the bulk flow, where it hydrolyses and disproportionates according to Reaction (C 5.5).

$$Cl_{2(aq)} + H_2O \underset{k_r}{\overset{k_f}{\rightleftharpoons}} HOCl + Cl^- + H^+ \tag{C 5.5}$$

The rate of production for the species on the right side of Reaction (C 5.5) is given by Equation (5.18).

$$\dot{R} = k_f c_{Cl_2} - k_r c_{HOCl} c_{Cl^-} c_{H^+} \tag{5.18}$$

where:

$\dot{R}$	Rate of production of species i	[mol/(m^3 s)]
k_f	Forward rate constant	[s^{-1}]
k_r	Backward rate constant	[m^6/(mol^2 s)]
c_i	Concentration of species i	[mol/m^3]

Due to the abundance of water in the cell during operation it is assumed that the concentration of water remains constant. The rate of production of the species on the left side of Reaction (C 5.5) is the opposite version of Equation (5.18).

The hypochlorous acid produced during Reaction (C 5.5) dissociates to its ions [C.Y. Cheng, 2007]. This is given by Reaction (C 5.6).

$$HOCl \underset{k_r}{\overset{k_f}{\rightleftharpoons}} H^+ + OCl^- \tag{C 5.6}$$

The rate of production for the species on the right side of Reaction (C 5.6) is given by Equation (5.19).

$$\dot{R} = k_f c_{\mathrm{HOCl}} - k_r c_{\mathrm{H^+}} c_{\mathrm{OCl^-}} \tag{5.19}$$

From Reaction (C 5.6) it is seen that the dissociation of hypochlorous acid produces the water disinfecting hypochlorite.

Furthermore, the homogeneous Reactions (C 5.7), (C 5.8) and (C 5.9) may occur to some extent in the electrolytic solution and thereby decrease the concentration of hypochlorite.

$$2\,\mathrm{OCl^-} \rightleftharpoons 2\mathrm{Cl^-} + \mathrm{O_2} \tag{C 5.7}$$

$$2\,\mathrm{HOCl} + \mathrm{OCl^-} \rightleftharpoons \mathrm{ClO_3}^- + 2\,\mathrm{Cl^-} + 2\,\mathrm{H^+} \tag{C 5.8}$$

$$\mathrm{OCl^-} + \mathrm{H_2} \rightleftharpoons \mathrm{H_2O} + \mathrm{Cl^-} \tag{C 5.9}$$

However, these can be considered to have insignificant rates at temperatures around 293 K [C.Y. Cheng, 2007]. Thus, these three reactions will not be taken into account, in this study.

The last reaction which is considered to be occurring in the electrochlorination cell is the dissociation of water, given by Reaction (C 5.10).

$$\mathrm{H_2O} \underset{\mathrm{k_r}}{\overset{\mathrm{k_f}}{\rightleftharpoons}} \mathrm{H^+} + \mathrm{OH^-} \tag{C 5.10}$$

The rate of production for the species on the right side of Reaction (C 5.10) is given by Equation (5.20).

$$\dot{R} = k_f c_{\mathrm{H_2O}} - k_r c_{\mathrm{H^+}} c_{\mathrm{OH^-}} \tag{5.20}$$

As can be seen from Reaction (C 5.10) this reaction will balance the concentrations of hydrogen ions and hydroxide such that when evaluating these inside the electrochlorination cell the pH values everywhere in the cell will not exceed the pH range from 0 to 14. This is due to the reaction being favoured strongly to the left. However, this reaction is not considered here due to convergence issues as the difference between the forward and backward rate constants is very significant. This means that the kinetics for Reactions (C 5.5) and (C 5.6) cannot be made pH dependent. Instead considerations are to be made about the approximate pH values at different locations inside the electrochlorination cell and assumptions about the reaction kinetics are made accordingly.

In the following the kinetics data for these reactions are treated.

5.2.2 Kinetics data for chemical reactions

Spalding [1962] studied reaction kinetics for the hydrolysis of chlorine, Reaction (C 5.5). This was done for pH values from 1 to 14. Spalding [1962] showed that the hydrolysis of chlorine is reversible for pH values below 3, and irreversible for pH values from 3 to 11.

Due to the secondary electrochemical reaction occurring, Reaction (C 5.2), positively charged hydrogen ions are produced. The production of positive hydrogen ions results in the pH value close to the anode being lowered. Thus, close to the anode the pH value is expected to be lower than 3, which in turn makes the reaction kinetics for hydrolysis of chlorine reversible, as given by Reaction (C 5.5). According to Wang and Margerum [1993] the reaction kinetics are given by $k_f = 15.0\,\mathrm{s}^{-1}$ and $k_r = 1.82 \times 10^{-2}\,\mathrm{m}^6/(\mathrm{mol}^2\,\mathrm{s})$ at 293 K, thus resulting in an equilibrium constant of $824\,\mathrm{mol}^2/\mathrm{m}^6$.

In the bulk flow the pH value is expected to be between 3 and 11, hence making the reaction kinetics for hydrolysis of chlorine irreversible. The irreversible reaction occurring in the bulk flow is given by Reaction (C 5.11).

$$\mathrm{Cl}_{2(\mathrm{aq})} + \mathrm{H_2O} \xrightarrow{k_f} \mathrm{HOCl} + \mathrm{Cl}^- + \mathrm{H}^+ \tag{C 5.11}$$

The rate of production for Reaction (C 5.11) is given by Equation (5.21).

$$\dot{R} = k_f c_{\mathrm{Cl}_2} \tag{5.21}$$

With an apparent forward rate constant of $k_f = 20.9\,\mathrm{s}^{-1}$ at a temperature of 298 K according to Spalding [1962].

The dissociation of hypochlorous acid is highly dependent on the pH value of the electrolytic solution. At pH values below 6, Reaction (C 5.6) is strongly favoured to the left, while for pH values above 9 the reaction is strongly favoured to the right, as seen in Figure 5.1 [Sawyer et al., 2003; O'Brien et al., 2005].

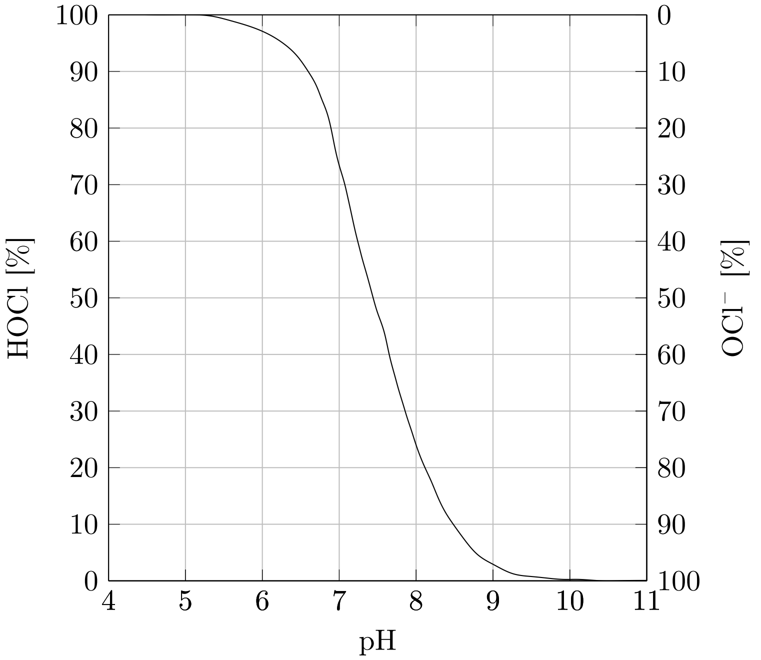

Figure 5.1. Effect of pH value on the distributions of hypochlorous acid and hypochlorite in water at 293 K [Sawyer et al., 2003].

Due to the hypochlorous acid being produced close to the anode in accordance with Reaction (C 5.5) the pH value is expected to be lower than 6 in this region and thus very small amounts of hypochlorite are produced in this region. Due to the forced flow through the cell gap the unreacted hypochlorous acid flows to the top part of the electrochlorination cell where the pH value is considered to be either around the neutral point of 7 or alkaline, as the production of hydroxide is expected to be greater than that of hydrogen ions. At a pH value of about 7 hypochlorous acid and hypochlorite exist in equal amounts [Sawyer et al., 2003; O'Brien et al., 2005]. Close to the cathode the pH value is expected to be above 9, which means that if any hypochlorous acid is capable of diffusing to this region, all is dissociated into hypochlorite and hydrogen ions [Sawyer et al., 2003; O'Brien et al., 2005]. The dissociation of hypochlorous acid is only considered in the region close to the anode, due to convergence issues when specifying this anywhere else in the electrochlorination cell in accordance with the considerations made above.

For the dissociation of hypochlorous acid, at pH values below 6, the equilibrium constant has been reported to be in the range from $2.7 \times 10^{-5}\,\mathrm{mol/m^3}$ to $3.5 \times 10^{-5}\,\mathrm{mol/m^3}$ at a temperature of 293 K [Sawyer et al., 2003; O'Brien et al., 2005; Spasojevic et al., 2015]. An equilibrium constant of $3.0 \times 10^{-5}\,\mathrm{mol/m^3}$ is chosen for Reaction (C 5.6). From the equilibrium constant the forward or backward rate constants can be calculated if one of these are known. This is given by Equation (5.22).

$$K_{eq} = \frac{k_f}{k_r} \tag{5.22}$$

where: K_{eq} | Equilibrium constant

As the kinetics of Reaction (C 5.6) are very fast and thus can be considered to be at equilibrium, C.Y. Cheng [2007] chose the backward rate constant to be $1.0 \times 10^2\,\mathrm{m^3/(mol\,s)}$, whereby the forward rate constant was calculated according to Equation (5.22). Increasing the backward rate constant further was shown to have insignificant effect. It is chosen to use the backward rate constant stated by C.Y. Cheng [2007], whereby the forward rate constant is found to be $3.0 \times 10^{-3}\,\mathrm{s^{-1}}$.

From Equations (5.18), (5.19) and (5.21) it is seen that the concentrations of several species are required in order to determine the rates of production or consumption. These concentrations are called from the transport of species aspect, thus creating a coupling between the two modelling aspects.

In the following the modelling of species transport is described.

5.3 Modelling of species transport

From Reactions (C 5.1) to (C 5.4), shown in Section 5.1.3, and Reactions (C 5.5), (C 5.6) and (C 5.11), shown in Section 5.2.1, it is seen that a number of different chemical species, besides water, are present in the cell during operation. These species, that is Cl^-, Cl_2, O_2, H_2, H^+, OH^-, OCl^-, HOCl, and Na^+, dissolve in the electrolytic solution and hence, create a dilute electrolytic solution since there is abundance of water compared to all other species.

This section describes, the assumptions applied to the modelling of the transport of species, followed by the governing equations for the modelling of species transport and finally the boundary conditions are treated.

5.3.1 Assumptions for species transport

Three species are likely to go to the gaseous phase, Cl_2, O_2 and H_2, if their local concentrations exceed their solubility in water, from which supersaturation would drive the formation of gas bubbles until the local concentrations no longer exceed their solubility in water [C.Y. Cheng, 2007]. The solubility of each of these species in water at 1 atm and 293 K is:

- Cl_2: 7.2900 g per 1000 g of water [Wired Chemist, 2016]
- O_2: 0.0430 g per 1000 g of water [Wired Chemist, 2016]
- H_2: 0.0016 g per 1000 g of water [Wired Chemist, 2016]

As seen from these solubilities very small amounts of O_2 and H_2 can be dissolved in the electrolytic solution, which contains mostly water, before supersaturation drives the formation of gas bubbles, compared to the amount of Cl_2. Thus, the produced O_2 and H_2 is assumed to go to the gaseous phase, whereas the produced Cl_2 is assumed to go to the liquid phase.

The concentrations of the produced O_2 and H_2 gas bubbles are of the same order of magnitude, meaning that one species is not dilute compared to the other. It is assumed that the bubbles of the produced O_2 and H_2 do not meet and interact with each other, and hence do not form bubbles containing mixtures of O_2 and H_2. Thus, transport of concentrated species does not need to be taken into account.

Based on these assumptions only transport of dilute liquid phase species is considered in this study. Due to the liquid species being dilute compared to the amount of water in the cell it is assumed that diffusion of one species into another species can be neglected and therefore only diffusion of every species into water is considered [Newman, 1991]. The diffusion coefficients of every species, considered to be present in the cell, into water are listed in Table 5.3.

Table 5.3. List of diffusion coefficients of every species in the liquid phase into water [C.Y. Cheng, 2007].

Species	Cl^-	Cl_2	H^+	OH^-
D_i [m^2/s]	$2.03 \cdot 10^{-9}$	$1.83 \cdot 10^{-9}$	$9.31 \cdot 10^{-9}$	$5.62 \cdot 10^{-9}$
Species	OCl^-	HOCl	Na^+	
D_i [m^2/s]	$1.10 \cdot 10^{-9}$	$1.28 \cdot 10^{-9}$	$1.33 \cdot 10^{-9}$	

The following describes the governing equations used to model the transport of dilute liquid species.

5.3.2 Dilute species transport

The motion, and hence molar flux, of dissolved species in an electrolytic solution is given by Nernst-Planck equation, which was given in Equation (5.1) and repeated below [Newman, 1991].

$$\boldsymbol{N}_i'' = -\underbrace{D_i \nabla c_i}_{\text{diffusion}} - \underbrace{z_i u_{m,i} F c_i \nabla \Phi_l}_{\text{migration}} + \underbrace{c_i \boldsymbol{u}}_{\text{convection}} \tag{5.1}$$

where:			
	$\boldsymbol{N}_i''$	Molar flux of species i	$[\mathrm{mol/(m^2\,s)}]$
	D_i	Diffusion coefficient of species i	$[\mathrm{m^2/s}]$
	c_i	Concentration of species i	$[\mathrm{mol/m^3}]$
	z_i	Valence of species i	$[-]$
	$u_{m,i}$	Mobility of species i	$[\mathrm{(s\,mol)/kg}]$
	F	Faraday's constant	$[\mathrm{C/mol}]$
	Φ_l	Electrolytic solution potential	$[\mathrm{V}]$
	$\boldsymbol{u}$	Velocity vector, $\boldsymbol{u} = (u, v)$	$[\mathrm{m/s}]$

The concentration gradient means that species will diffuse from regions of high concentration to regions of low concentration, charged particles will migrate due to the potential gradient across the electrolytic solution and the forced flow of the solution will make species follow the bulk motion [Newman, 1991].

A material balance for every species in the electrolytic solution is needed. This material balance is given by Equation (5.23) [Newman, 1991].

$$\frac{\partial c_i}{\partial t} = -\nabla \bullet \boldsymbol{N}_i'' + \dot{R}_i \tag{5.23}$$

where:			
	c_i	Concentration of species i	$[\mathrm{mol/m^3}]$
	$\dot{R}_i$	Rate of production or consumption of species i	$[\mathrm{mol/m^3\,s}]$

Equation (5.23) states that the accumulation of species i equals the net input of species i, inflow minus outflow, plus the rate of production of species i [Newman, 1991]. The net input of species i is the gradient of the Nernst-Planck equation given by Equation (5.1) and the rate of production of species i is given by the rates of production for Reactions (C 5.5), (C 5.6) and (C 5.11) stated in Section 5.2.1.

In order to take into account the gas bubbles occupying some volume in the cell, which influences the transport of liquid species, the species transport is treated as transport in a porous media. Hence, Equation (5.23) is multiplied by the volume fraction of the electrolytic solution, which is called from the two-phase flow aspect. This is given by Equation (5.24).

$$\frac{\partial c_i \phi_l}{\partial t} = -\phi_l \nabla \bullet \boldsymbol{N}_i'' + \phi_l \dot{R}_i \tag{5.24}$$

At the same time the velocity of the electrolytic solution is called from the modelling of the two-phase flow, due to this being a part of the convective term in Nernst-Planck equation given by Equation (5.1). Moreover, the potential across the electrolytic solution is called from the modelling of the electrochemistry, due to this being a part of the migrational term in Nernst-Planck, Equation (5.1). Finally, the rate of production or consumption of each species is called from the modelling of the chemical reactions in order to take into account species being produced and consumed in the bulk flow.

In the following the boundary conditions are treated.

5.3.3 Boundary conditions

Due to the electrochemical reactions, Reactions (C 5.1) to (C 5.4), at the anode and cathode, mass fluxes of species being produced or consumed are occurring. These fluxes are given by Faraday's law of electrolysis according to Equation (5.26) [Newman, 1991].

$$N''_{0,i} = \frac{\nu_{i,m} i_{loc,m}}{n_{\mathrm{e}^-,m} F} \tag{5.25}$$

$$-\boldsymbol{n} \bullet \boldsymbol{N}''_i = N''_{0,i} \tag{5.26}$$

where:			
	$N''_{0,i}$	Molar boundary flux of species i	[mol/(m^2 s)]
	$\nu_{i,m}$	Stoichiometric coefficient of species i in reaction m	[–]
	$i_{loc,m}$	Local current density for reaction m	[A/m^2]
	$n_{\mathrm{e}^-,m}$	Number of electrons participating in the m'th reaction, see Reactions (C 5.1) to (C 5.4).	[–]

Knowing the local current density for the m^{th} reaction, the molar flux of species i is known due to the stoichiometric coefficients and number of electrons being known for all the reactions occurring at the anode and cathode. The local current density is called from the modelling of the electrochemistry.

At the inlet a boundary condition of constant concentration of each species is applied and at the outlet a zero concentration gradient is applied. The applied inflow and outflow expressions are shown in Equations (5.27) and (5.28), respectively.

$$c_i = c_{0,i} \tag{5.27}$$

$$-\boldsymbol{n} \bullet D_i \nabla c_i = 0 \tag{5.28}$$

where:			
	$c_{0,i}$	Inlet concentration of the i'th species	[mol/m^3]

The salt used is known to be sodium chloride and when dissolved in water it dissociates into positively charged sodium and negatively charged chloride ions, as shown in Reaction (C 5.12).

$$\mathrm{NaCl} \longrightarrow \mathrm{Na^+} + \mathrm{Cl^-} \tag{C 5.12}$$

From Reaction (C 5.12) it is seen that for every mole of dissolved sodium chloride one mole positively charged sodium ions and one mole negatively charged chloride ions are formed. 30 g/L of salt are added for every 1 L of water, as stated in Appendix B. Thus, it is found that the constant inlet concentrations of sodium and chloride ions are:

$$c_{0,Na^+} = c_{0,Cl^-} = 513.3\,\mathrm{mol/m^3} \tag{5.29}$$

There are no inlet concentrations for the remaining dilute species since these species are produced by the chemical reactions in the electrolytic solution and the electrochemical reactions taking place at the anode and cathode.

In the following the modelling of the two-phase flow is described.

5.4 Modelling of bubbly two-phase flow

As stated in Section 5.3.1, the O_2 and H_2 produced at the anode and cathode, respectively, go to the gaseous phase, whereas the rest of the species are in the liquid phase. Hence, a two-phase flow has to be treated. From Section 4.4 it is seen that the flow occurring in the cell is a dispersed flow, meaning that the gas phase is dispersed in the continuous phase, electrolytic solution.

First considerations about modelling approaches are described, followed by the governing equations for the modelling, the simplifications used for the modelling of the dispersed two-phase flow, and finally the boundary conditions are treated.

5.4.1 Two-phase flow considerations

In order to model the phases a reference frame has to be chosen for each phase, Eulerian or Lagrangian. For the electrolytic solution an Eulerian reference frame is typically chosen due to this usually being the most computationally efficient approach [Crowe, 2006]. In the Eulerian reference frame the domain is divided into a number of spatial discretizations, which stay fixed to external coordinates. In each of these spatial discretizations the properties of the flow are evaluated as a function of time. The electrolytic solution can as well generally be considered to be a continuum, meaning that the properties of the flow have gradual transition from one value to another without sudden changes [Crowe, 2006].

For the gas bubbles both Eulerian and Lagrangian reference frames can be applied depending on the number of particles that need to be modelled [Crowe, 2006]. In the Lagrangian reference frame every gas bubble is tracked through the domain, and hence every particle is treated as an individual entity, and the properties of the particles are updated along their paths. For many particles, and hence high volume fractions of particles, tracking of the gas bubbles becomes too computational expensive and may cause convergence issues [Crowe, 2006]. In the Eulerian reference frame the particles are considered to constitute an additional fluid, which can be treated as a continuum, thus following the modelling approach as for the electrolytic solution and averaging the gas bubbles in every control volume [Crowe, 2006]. From the images of Section 4.4 it is seen that considerable amounts of bubbles are produced. Hence, it is assessed that tracking of each individual bubble will be too computational expensive and thus, the gas bubbles are treated as a continuum. This means that the electrolytic solution and gas bubbles are treated as interpenetrating continua and thus an Euler/Euler approach is used.

Apart from the reference frame, considerations also have to be made about the shape of the bubbles in order to estimate whether these can be assumed to be spherically shaped or not. This can be estimated by calculating the Eötvös and Reynolds numbers of the flow [Crowe, 2006]. Knowing these numbers a shape-map can be used to determine the shape region for the flow, and hence the shape of the bubbles.

The schematic diagrams of bubbles in motion and shape-map for bubbles at different Eötvös and Reynolds numbers are shown in Figure 5.2 [Crowe, 2006].

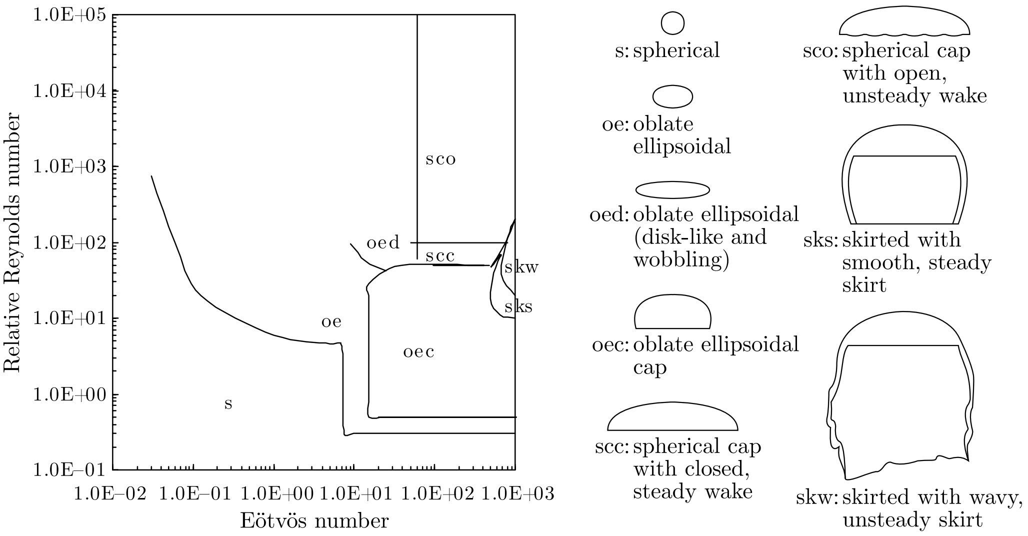

Figure 5.2. Schematic diagrams of bubbles in motion and shape-map for bubbles at different Eötvös and Reynolds numbers.

The Eötvös and Reynolds numbers are given by Equations (5.30) and (5.31), respectively.

$$\mathrm{Eo} = \frac{|\boldsymbol{g}|\,(\rho_l - \rho_g)\,d_b^2}{\varsigma} \tag{5.30}$$

$$\mathrm{Re} = \frac{\rho_l d_b v_t}{\mu_l} \tag{5.31}$$

where:	Eo	Eötvös number	[–]
	Re	Reynolds number	[–]
	$\lvert\boldsymbol{g}\rvert$	Magnitude of the gravitational acceleration	[m/s^2]
	ρ	Density	[kg/m^3]
	d_b	Diameter of gas bubbles	[m]
	ς	Surface tension	[N/m]
	v_t	Terminal velocity of gas bubbles	[m/s]
	μ_l	Dynamic viscosity of electrolytic solution	kg/(m s)]
	l	Denotes electrolytic solution	
	g	Denotes gas bubbles	

From the schematic diagrams and shape-map shown in Figure 5.2 it is seen that there are 8 possible shapes of the bubbles. Using the data presented in Appendix B it is found that the bubbles have a mean size of 62.4 µm. At the same time it is visualised that almost all bubbles are produced at the cathode. Thus, the density of hydrogen can be used as that of the gas bubbles for estimation of the Eötvös number. As stated in Section 5.1.3 there is abundance of water compared to all other liquid phase species occurring in the cell. Thus, it is assessed that the density, surface tension and dynamic viscosity of water can be used as those for the electrolytic solution. The terminal velocity of the bubbles can be difficult to estimate due to changes as the bubbles rise through the cell [Celata et al., 2006]. Closely packed bubbles may influence each other due to the wake formed by the preceding bubble, thus influencing the terminal velocity of the bubble following behind [Celata et al., 2006]. A Eötvös number of about 0.0005 is found. As seen from the shape-map in Figure 5.2 such a Eötvös number will result in a Reynolds number over 1×10^5. This results in a terminal velocity of the bubbles of several hundred m/s in order for the bubbles not to be spherical, using the bubble size of 62.4 µm and the properties of water. From this it is assessed that the bubbles will be spherical at all times, and thus spherical bubbles can be used for the modelling of the two-phase flow.

Furthermore, considerations also have to be put into how the flow of bubbles is compared to the electrolytic solution, i.e. whether the bubbles follow the flow of the solution or not. This can be estimated by calculating the Stokes number. The Stokes number is defined as the ratio between response time of the bubble, τ_b, to that of the flow, τ_f. This is given by Equation (5.32) [Crowe, 2006].

$$\mathrm{Stk} = \frac{\tau_b}{\tau_f} \tag{5.32}$$

where:			
	Stk	Stokes number	[−]
	τ	Response time of bubble or flow	[s]

The response times of the particle and flow are given by Equations (5.33) and (5.34) [Crowe, 2006], respectively.

$$\tau_v = \frac{\rho_g d_b^2}{18\mu_l} \tag{5.33}$$

$$\tau_f = \frac{w_{gap}}{\boldsymbol{u}_l} \tag{5.34}$$

where:			
	w_{gap}	Width of cell gap	[m]
	$\boldsymbol{u}_l$	Velocity of electrolytic solution	[m/s]

Again using the properties of hydrogen for the gas bubbles, the properties of water for the electrolytic solution as well as a bubble diameter of 62.4 mm, a cell gap of 7.68 mm between the electrodes, a gap depth of 40 mm and an inlet flow of 2 L/h it is found that the Stokes number of the flow between the electrodes is 4.71×10^{-9}. Due to the Stokes number being much less than 1, Stk << 1, the bubbles have plenty of time to respond to changes in the flow and thus the bubbles should follow the flow of the electrolytic solution [Crowe, 2006]. However, comparing the densities of the electrolytic solution, water, and the gas bubbles, hydrogen, it is seen that there is a considerable difference in densities between the phases and thus a significant buoyancy force is expected to be acting on the gas bubbles. This will in turn result in a slip velocity between the phases, which results in a drag force being exerted on the gas bubbles by the electrolytic solution.

The following describes the governing equations for the Euler/Euler approach for the modelling of the two-phase flow.

5.4.2 Governing equations for two-phase flow modelling

As stated in Section 5.4.1 the electrolytic solution and gas bubbles are treated as interpenetrating continua in the Euler/Euler approach, which means that the two-phase equations are like their single-phase counterparts [Kuzmin and Turek, 2000]. These are coupled by the transfer of mass and momentum from one phase to the other [Kuzmin and Turek, 2000].

The continuity equations for the gas bubbles and electrolytic solution are given by Equations (5.35) and (5.36), respectively [Kuzmin and Turek, 2000].

$$\frac{\partial}{\partial t}\left(\phi_g \rho_g\right) + \nabla \bullet \left(\phi_g \rho_g \boldsymbol{u}_g\right) = -\dot{m}_{gl}''' \tag{5.35}$$

$$\frac{\partial}{\partial t}\left(\phi_l \rho_l\right) + \nabla \bullet \left(\phi_l \rho_l \boldsymbol{u}_l\right) = \dot{m}_{gl}''' \tag{5.36}$$

where:	ϕ_i	Volume fraction of phase i.	[–]
	$\boldsymbol{u}_i$	Velocity vector of phase i	[m/s]
	$\dot{m}_{gl}'''$	Mass transfer rate between the gas and liquid phases	[kg/(m^3 s)]

The volume fraction of the gas bubbles and the electrolytic solution should sum up to 1 everywhere in the cell, which is given by Equation (5.37) [Kuzmin and Turek, 2000].

$$\phi_l + \phi_g = 1 \tag{5.37}$$

Due to $\dot{m}_{gl}'''$ being defined as the transfer of mass from the gas bubbles to the electrolytic solution it is negative for the continuity equation of the gas bubbles and positive for the continuity equation of the electrolytic solution [Kuzmin and Turek, 2000].

The momentum equations for the gas bubbles and electrolytic solution are given by Equations (5.38) and (5.39), respectively [Kuzmin and Turek, 2000].

$$\phi_g \rho_g \left(\frac{\partial \boldsymbol{u}_g}{\partial t} + \left(\boldsymbol{u}_g \bullet \nabla\right)\boldsymbol{u}_g\right) = -\phi_g \nabla p + \phi_g \rho_g \boldsymbol{g} + f_{int} \tag{5.38}$$

$$\begin{aligned} \phi_l \rho_l \left(\frac{\partial \boldsymbol{u}_l}{\partial t} + \left(\boldsymbol{u}_l \bullet \nabla\right)\boldsymbol{u}_l\right) &= -\phi_l \nabla p + \phi_l \rho_l \boldsymbol{g} \\ &\quad + \nabla \bullet \left(\phi_l \mu_l \left[\nabla \boldsymbol{u}_l + \left(\nabla \boldsymbol{u}_l\right)^T - \frac{2}{3}\left(\nabla \boldsymbol{u}_l\right)\boldsymbol{I}\right]\right) - f_{int} \end{aligned} \tag{5.39}$$

where:	p	Pressure	[Pa]
	f_{int}	Force contributions from drag, virtual mass and lift	[N/m^3]
	$\boldsymbol{I}$	Identity matrix	[–]

Momentum transfer due to dissolution of the gas bubbles is generally neglected due to its small contribution [Kuzmin and Turek, 2000]. Just as for the mass transfer between phases, the force contributions have opposite signs for the gas and liquid phases, respectively [Kuzmin and Turek, 2000]. The interaction forces, f_{int}, occur due to a relative motion between the gas bubbles and electrolytic solution. This relative motion creates local pressure and shear stress variations [Sokolichin et al., 2004]. Due to the model being a two-fluid model these forces have to be modelled using empirical correlations or approximations. Several forces are generally considered to be contributing, the buoyancy force f_B, the drag force f_D, the added mass force f_{AM}, the lift force f_L, etc. [Sokolichin et al., 2004].

The following describes the simplifications used for the two-phase flow modelling.

5.4.3 Simplifications for two-phase modelling

By inserting Equation (5.36) into Equation (5.35) a combined continuity equation for the two phases can be obtained [Sokolichin et al., 2004]. This is given by Equation (5.40).

$$\frac{\partial}{\partial t}\left(\phi_l \rho_l + \phi_g \rho_g\right) + \nabla \bullet \left(\phi_l \rho_l \boldsymbol{u}_l + \phi_g \rho_g \boldsymbol{u}_g\right) = 0 \tag{5.40}$$

Thus, in order to keep track of the gas distribution in the cell, Equation (5.35) can be used [Sokolichin et al., 2004]. As stated in Section 5.4.1 the Stokes number indicates that the gas bubbles should follow the electrolytic solution, meaning that the velocities of these two phases should be approximately equal. This is known as the homogeneous slip model [Sokolichin et al., 2004]. However, as stated previously, there is a considerable difference in densities between the two phases, expected to be causing a slip velocity between the phases. The velocity of the gas bubbles is then related to that of the electrolytic solution through Equation (5.41) [Kuzmin and Turek, 2000].

$$\boldsymbol{u}_g = \boldsymbol{u}_l + \boldsymbol{u}_{slip} \tag{5.41}$$

where:			
	$\boldsymbol{u}_{slip}$	Slip velocity	[m/s]

The slip velocity defines the relative velocity between the gas bubbles and electrolytic solution [Kuzmin and Turek, 2000]. The slip velocity between the phases can be estimated by considering the momentum equation for the gas bubbles. As stated in Section 5.4.1, the density of water is used for the electrolytic solution and the density of hydrogen for the gas bubbles. Comparing these densities at the operating temperature and pressure of 293 K and 1 bar, respectively, it is seen that the density of water is much greater than that of hydrogen. Hence, the inertia and gravity terms in the momentum equation for the gas bubbles can be omitted [Kuzmin and Turek, 2000]. Thus, the momentum equation for the gas bubbles reduces to Equation (5.42).

$$0 = -\phi_g \nabla p + f_{int} \tag{5.42}$$

In the literature it is generally argued that the dominant contribution to the interaction forces is that of the drag force [Sokolichin et al., 2004; Kuzmin et al., 2005]. However, due to the large difference in densities the buoyancy force is expected to have a significant effect on the slip velocity between the phases [Legendre and Magnaudet, 1998]. Considering a single spherical bubble the drag and buoyancy forces can be seen to orient themselves as seen in Figure 5.3.

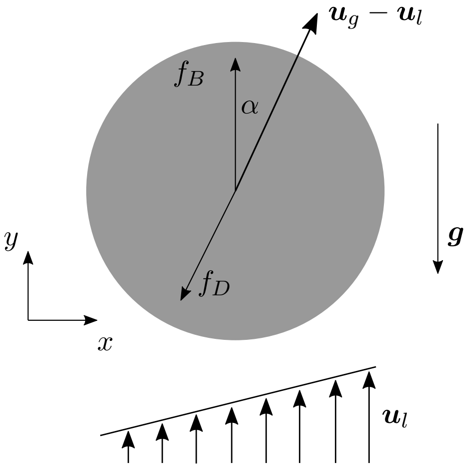

Figure 5.3. Representation of forces on a bubble rising in a linear shear flow, indicating the direction of drag and buoyancy. Angle α is the instantaneous angle between y-axis and direction of motion. Inspired by [Dijkhuizen et al., 2010].

By considering these forces to be acting on every bubble in the flow Equation (5.42) can be rewritten into Equation (5.43).

$$0 = -\phi_g \nabla p + f_D + f_B \tag{5.43}$$

Where the drag and buoyancy forces are given by Equations (5.44) and (5.45), respectively [Dijkhuizen et al., 2010].

$$f_D = -\phi_g C_W \boldsymbol{u}_{slip} \tag{5.44}$$

$$f_B = \phi_g \boldsymbol{g}(\rho_l - \rho_g) \tag{5.45}$$

where:			
	f_D	Drag force	[N/m^3]
	f_B	Buoyancy force	[N/m^3]
	C_W	Linearisation parameter	[kg/(m^3 s)]

Inserting Equations (5.44) and (5.45) into Equation (5.43) the momentum equation for the gas bubbles can be written as Equation (5.46).

$$0 = -\phi_g \nabla p - \phi_g C_W \boldsymbol{u}_{slip} + \phi_g \boldsymbol{g}(\rho_l - \rho_g) \tag{5.46}$$

From Equation (5.46) the slip velocity can be found, as shown in Equation (5.47).

$$\boldsymbol{u}_{slip} = \frac{-\nabla p + \boldsymbol{g}(\rho_l - \rho_g)}{C_W} \tag{5.47}$$

The linearisation parameter is given by Equation (5.48) [Kuzmin et al., 2005].

$$C_W = \frac{3}{4} C_D \frac{\rho_l}{d_b} |\boldsymbol{u}_{slip}| \tag{5.48}$$

where:			
	C_D	Drag coefficient	[–]

Due to the diameter of the gas bubbles being less than 2 mm the following expressions for the drag coefficient and Reynolds number can be used, Equations (5.49) and (5.50) [Crowe et al., 1998].

$$C_D = \frac{16}{\text{Re}_g} \tag{5.49}$$

$$\text{Re}_g = \frac{d_b \rho_l |\boldsymbol{u}_{slip}|}{\mu_l} \tag{5.50}$$

If turbulence occurs in the cell, the gas bubbles are subject to 'bubble path dispersion' [Kuzmin et al., 2005]. Due to this dispersion a drift velocity is occurring, which then should be added to the equation for the gas velocity, Equation (5.41) [Kuzmin et al., 2005]. The drift velocity is given by Equation (5.51) [Kuzmin et al., 2005].

$$\boldsymbol{u}_{drift} = -\frac{\mu_l}{\rho_l}\frac{\nabla \phi_g}{\phi_g} \tag{5.51}$$

As seen from Equation (5.51) the drift velocity is proportional to the gradient of the volume fraction of the gas bubbles and is directed opposite to it [Kuzmin et al., 2005]. However, here it is assumed that the turbulence induced by the gas bubbles can be neglected, and hence the drift velocity due to this turbulence is not considered. Inserting Equation (5.41) into Equation (5.35) the following continuity equation for the gas bubbles is obtained, Equation (5.52).

$$\frac{\partial \rho_g \phi_g}{\partial t} + \nabla \bullet \left(\rho_g \phi_g \left(\boldsymbol{u}_l + \boldsymbol{u}_{slip}\right)\right) = -\dot{m}'''_{gl} = 0 \tag{5.52}$$

Equation (5.52) is thus used for keeping track of the gas distribution through the cell [Kuzmin et al., 2005]. Equation (5.52) equals zero due to no transfer of mass between the gas bubbles and the electrolytic solution, as the bubbles rise through the electrochlorination cell.

Equation (5.42) can be added to Equation (5.39) whereby a combined momemtum equation for the two phases is obtained [Kuzmin and Turek, 2000]. This is given by Equation (5.53).

$$\phi_l \rho_l \left(\frac{\partial \boldsymbol{u}_l}{\partial t} + \left(\boldsymbol{u}_l \bullet \nabla\right)\boldsymbol{u}_l\right) = -\nabla p + \phi_l \rho_l \boldsymbol{g} + \nabla \bullet \left(\phi_l \mu_l \left[\nabla \boldsymbol{u}_l + \left(\nabla \boldsymbol{u}_l\right)^T - \frac{2}{3}\left(\nabla \boldsymbol{u}_l\right)\boldsymbol{I}\right]\right) \tag{5.53}$$

At the same time it is assumed that the gas bubbles and electrolytic solution share the same pressure field, $p = p_g = p_l$. This is a common assumption used for two-phase gas-liquid modelling [Kuzmin and Turek, 2000].
Thus, the modelling of the two-phase flow is given by Equations (5.37), (5.40), (5.41), (5.47), (5.52) and (5.53) in which the properties of water can be used for the electrolytic solution and the properties of hydrogen for the gas bubbles, as stated in Section 5.4.1.

In the following the boundary conditions are treated.

5.4.4 Boundary conditions

As stated in Section 5.3.1 O_2 and H_2 are produced at the anode and cathode, respectively, due to the electrochemical reactions occurring. Thus, mass fluxes of these gas species, at the anode and cathode, can be determined by using Faraday's law of electrolysis, just as for the production and consumption of liquid phase species, defined by Equation (5.25) in Section 5.3.3. The mass fluxes at the electrodes as well as the gas boundary condition at the walls of the cell are shown in Equations (5.54) and (5.55), respectively.

$$\dot{m}''_{0,i} = \frac{\nu_{i,m} i_{loc,m}}{n_{\mathrm{e}^-,m} F} \cdot M_i \tag{5.54}$$

$$-\boldsymbol{n} \bullet \dot{m}''_i = \begin{cases} 0 & \text{for walls} \\ \sum \dot{m}''_{0,i} & \text{for electrodes} \end{cases} \qquad \text{(Gas flux condition)} \tag{5.55}$$

where:			
$\dot{m}''_i$	Mass flux of species i		$[\mathrm{kg/(m^2\,s)}]$
$\dot{m}''_{0,i}$	Mass boundary flux of species i		$[\mathrm{kg/(m^2\,s)}]$
$\nu_{i,m}$	Stoichiometric coefficient of species i in reaction m		[–]
$i_{loc,m}$	Local current density for reaction m		$[\mathrm{A/m^2}]$
$n_{\mathrm{e}^-,m}$	Number of electrons participating in the m'th reaction, see Reactions (C 5.1) to (C 5.4).		[–]
F	Faraday's constant		[C/mol]
M_i	Molar mass of the i^{th} species		[kg/mol]

The local current density is called from the modelling of the electrochemistry, thus ensuring a coupling between these two modelling aspects. Due to the electrochemistry being concentration dependent, couplings to the modelling of chemical reactions and transport of species are ensured indirectly as well.

As stated in Section 5.3.3 a liquid mixture of water, and dissolved sodium and chloride ions is pumped through the cell. For this electrolytic solution an inlet boundary condition as well as a boundary condition at the walls of the cell have to be given. These boundary conditions are given by Equations (5.56) and (5.57), respectively.

$$\boldsymbol{u}_l = -\boldsymbol{u}_0\boldsymbol{n} \qquad \text{(Inlet velocity condition)} \tag{5.56}$$

$$\boldsymbol{u}_l = \boldsymbol{0} \qquad \text{(No slip condition)} \tag{5.57}$$

where		
$\boldsymbol{u}_0$	Inlet velocity of the electrolytic solution	[m/s]
$\boldsymbol{0}$	Zero vector	[–]

At the outlet both the gas bubbles and electrolytic solution are exiting. A relative pressure, p_0, of 0 is used, leading to the pressure at the outlet being that of the surroundings. For the gas bubbles a symmetry boundary is applied, which states that the effective density of the gas bubbles just outside the cell should equal that just inside the cell. The outlet pressure and gas condition are given by Equations (5.58) and (5.59), respectively.

$$p_0 = 0 \qquad \text{(Outlet pressure condition)} \tag{5.58}$$

$$\phi_g \rho_g = \phi_{g0} \rho_g \qquad \text{(Outlet gas condition)} \tag{5.59}$$

Due to the density of the gas bubbles being constant Equation (5.59) also shows that the gas volume fraction just outside the cell equals that just inside the cell. Thus, a build-up of gas bubbles is prevented in the cell.

In the following the couplings between each modelling aspect are summarised.

5.5 Couplings between modelling aspects

The modelling of each aspect is done in COMSOL Multiphysics. Several studies state problems with convergence using the preprogrammed modules integrated in COMSOL Multiphysics [Ipek et al., 2006, 2008]. However, due to the easy applicability of the preprogrammed modules it is decided to apply these modules to the problem at hand. The modules integrated in COMSOL Multiphysics used to model each modelling aspect are:

- Electrochemistry → Secondary Current Distribution (SCD)
- Chemical reactions → Chemistry (CHEM)
- Transport of species → Transport of Dilute Species (TDS)
- Two-phase flow → Bubbly Flow (BF)

Table 5.4 summarises and shows the couplings between the aspect being modelled and the variables called from other modelling aspects as well as the equations through which these couplings are achieved.

Table 5.4. Tabulation of called variables and coupled equations through which the couplings are achieved.

	Called Variable and Coupled Equation			
Aspect	SCD	CHEM	TDS	BF
SCD			c_i (Eqn. 5.13)	ϕ_l (Eqn. 5.11)
CHEM			c_i (Eqns. 5.18,5.19 and 5.21)	
TDS	Φ_l and $i_{loc,m}$ (Eqns. 5.24 - 5.25)	$\dot{R}_m$ (Eqn. 5.24)		ϕ_l and $\boldsymbol{u_l}$ (Eqn. 5.24)
BF	$i_{loc,m}$ (Eqn. 5.54)			

This concludes the modelling of the aspects occurring in the electrochlorination cell. In Chapter 6 considerations about the numerical simulations conducted in COMSOL Multiphysics are described.

Sixth Chapter

Numerical simulations in COMSOL Multiphysics

This chapter serves to describe how simulations are conducted using COMSOL Multiphysics, which uses the Finite Element Method (FEM) to numerically solve the governing partial differential equations (PDE), as exemplified in Appendix F. Simulations are performed with the same general geometry for two different cell gaps, 2 mm and 7.68 mm, where the geometry with a cell gap of 7.68 mm is used for validation against experimental data in Chapter 7. Further investigations are then conducted using the 2 mm cell gap geometry in Chapter 8. In order to obtain reliable results considerations have to be made about solution strategy, numerical stabilisation, mesh topology and density. These considerations are done in the following using the geometry with 7.68 mm cell gap, however, these are also applied for the geometry with 2 mm cell gap. Many of the considerations are based on guidelines given in the COMSOL Multiphysics Manual [COMSOL, 2015b]. Furthermore, mesh independence analyses are performed for both geometries in order to ensure that the obtained solutions are independent of the mesh element size.

The geometry used in the modelling and throughout this chapter is given by the zoom shown in Figure G.2a in Appendix G. By comparing the model geometry, Figure G.2a, to the two-dimensional of the constructed electrochlorination cell, Figure G.1a, it is seen that the bottom and much of the top part is not considered in the modelling. The bottom part is left out due to no phenomena, except single-phase liquid flow, occurring here. A plug flow is given at the inlet of the cell gap. In terms of much of the top part, initial numerical experimentations showed that a significant accumulation of bubbles is occurring in the right corner towards the outlet. This accumulation continued until the solution started to diverge and eventually failed. Due to the formulation of the bubbly two-phase flow bubbles do not have anywhere to go beneath walls where the forces acting on the bubbles force them upward and no term in the formulation prevents the gas volume fraction from growing [COMSOL, 2015b]. Thus, it is decided to leave much of the top part out, such that the bubbles do not accumulate in the domain.

6.1 Solution strategy

Modelling of the species transport and especially the two-phase flow results in highly non-linear PDEs and hence a highly non-linear problem, to which there might not exist a unique solution [COMSOL, 2015b]. COMSOL Multiphysics uses an iterative Newton method to solve the non-linear set of PDEs. This iterative method is reported to be sensitive to the initial guesses of the solution [COMSOL, 2015b]. This means that if the initial guesses are too far from the solution, convergence to a stationary solution might be difficult or even impossible.

In order to obtain a solution to the highly non-linear problem it is, thus, decided to obtain time-dependent solutions to the problem, resulting in better and smoother convergence [COMSOL, 2015b]. In order to obtain a sufficient steady-state solution a sufficient long simulation time has to be used for the time-dependent problem. Such a time-dependent solution is expected to be very close to the solution of the stationary problem. Based on much numerical experimentation it is assessed that a total simulation time of 125 s is needed for the geometry with 7.68 mm cell gap and 40 s for the geometry with 2 mm cell gap, in order for the time-dependent problem to reach a sufficiently steady solution. These time-dependent solutions thus, constitute the steady-state solutions used for studying the behaviour in the electrochlorination cell.

As described in Section 5.5 the phenomena occurring in the electrochlorination cell are highly coupled. Thus, a solution has to be obtained for a highly coupled and non-linear problem, for which a coupled solver is generally recommended [COMSOL, 2015b]. However, as also reported by Ipek et al. [2006, 2008], using a coupled solver failed to give a converged solution. In order to obtain a converged solution to the system of equations the problem is solved in a segregated fashion, similar to that reported by Ipek et al. [2006], where the electric potential across the electrolytic solution is solved first, followed by the effective gas density, pressure and liquid velocity field and finally the species transport.

In order to ensure that the time-dependent solution is accurate the tolerance of the solution should be sufficiently low. COMSOL Multiphysics uses a relative tolerance between the present and previous iteration in order to describe the precision of the obtained solution. In order to achieve an accurate solution without being too computational expensive the difference between the present and previous iteration should be under 1%, thus resulting in a relative tolerance of 10^{-2}.

In the following considerations about the stabilisation of the numerical simulations are described.

6.2 Stabilisation of numerical simulations

The FEM approach is quite straightforward for transport phenomena dominated by diffusion. However, transport phenomena driven mainly by convection are known to cause numerical instabilities, or oscillations, in the numerical solution [COMSOL, 2015b]. The convection-diffusion transport equation for an unknown parameter h, whether it is mass transport (Transport of Dilute Species) or transport of momentum given by Navier-Stokes equations (Laminar Bubbly Flow), takes the form of Equation (6.1) [COMSOL, 2015b].

$$\frac{\partial h}{\partial t} + \boldsymbol{u} \cdot \nabla h = \nabla \cdot (D \cdot \nabla h) + \Lambda \tag{6.1}$$

where:			
	h	Unknown parameter to be solved for	
	$\boldsymbol{u}$	Velocity vector	[m/s]
	D	Diffusion coefficient	[m^2/s]
	Λ	Source term	

Literature states that the instabilities in the solution are caused by the element Peclet number exceeding 1 [COMSOL, 2015b]. The Peclet number relates the convective and diffusive effects as shown by Equation (6.2).

$$\text{Pe}_{el} = \frac{\Delta x |\boldsymbol{u}|}{2D} \tag{6.2}$$

where:			
	Pe_{el}	Element Peclet number	[–]
	Δx	Mesh element size	[m]

From Equation (6.2) it is seen that large convective and/or small diffusive effects require a small element size in order to ensure that the element Peclet number does not exceed 1. As stated in Section 5.4.4 an inlet velocity of 1.8 mm/s is given as input for a cell gap of 7.68 mm. Furthermore, Table 5.3 in Section 5.3.1 shows that the smallest diffusion coefficent is that of OCl^-, which is in the order of 10^{-9}. Using these values and the fact that the Peclet number should not exceed 1, the mesh element size in order to ensure this can be found using Equation (6.3).

$$\Delta x \leq \frac{2D}{|\boldsymbol{u}|} = \frac{1.8 \cdot 10^{-9}\,\text{m}^2/\text{s}}{0.002\,\text{m/s}} \approx 10^{-6}\,\text{m} \tag{6.3}$$

From Equation (6.3) it is seen that a maximum mesh element size of 10^{-6} m is required in order to ensure that the Peclet number does not exceed 1. Using this mesh element size in the entire domain would result in an extremely high number of mesh elements and hence make the computational efforts impossible to overcome. Thus, some stabilisation is required to stabilise the solution for a coarser mesh.

This stabilisation is performed by adding artificial diffusion, thus lowering the element Peclet number. This is done by defining an artificial diffusion coefficient, D_{art}, which is added to the actual diffusion coefficient and the convection-diffusion equation. The artificial diffusion coefficient is given by Equation (6.4) [COMSOL, 2015b].

$$D_{art} = \zeta \Delta x |\boldsymbol{u}| \tag{6.4}$$

where:			
	D_{art}	Artificial diffusion coefficient	[m^2/s]
	ζ	Tuning parameter	[–]

The tuning parameter, ζ, is used to control the amount of artificial diffusion needed to sufficiently stabilise the solution. By adding Equation (6.4) to the original diffusion coefficient the Peclet number given by Equation (6.2) can be rewritten into Equation (6.5)

$$\mathrm{Pe}_{el} = \frac{\Delta x|\boldsymbol{u}|}{2\left(D + D_{art}\right)} = \frac{\Delta x|\boldsymbol{u}|}{2D + 2\zeta\Delta x|\boldsymbol{u}|} \tag{6.5}$$

From Equation (6.5) it is seen that a tuning parameter of $\zeta = 0.5$ will ensure that the element Peclet number does not exceed 1. However, a smaller value is often sufficient to stabilise the solution [COMSOL, 2015b]. Furthermore, adding much artificial diffusion also leads to significant deviation from the exact solution, since the modified transport equation in these cases will deviate significantly from the original, as seen from Equation (6.6) [COMSOL, 2015b].

$$\frac{\partial h}{\partial t} + \boldsymbol{u} \cdot \nabla h = \nabla \cdot \left(\left(D + D_{art}\right) \cdot \nabla h\right) + F \tag{6.6}$$

Thus, a compromise has to be made between the mesh element size and artificial diffusion such that the correct physical behaviour is captured in the electrochlorination cell model without being too computationally expensive.

In the following considerations about mesh topology, density and thus, the required amount of stabilisation are described.

6.3 Mesh topology and density

Figure 6.1 shows the two-dimensional representations of the electrochlorination cell to be meshed.

Due to electrochemical reactions occurring at the electrodes as well as chemical reactions occurring in the electrolytic solution, diffusion layers occur at the anode and cathode. These diffusion layers are considerably smaller than the hydrodynamic boundary layer and thus a much denser mesh is required in the regions close to the electrodes in order to adequately resolve these diffusion layers [Ipek et al., 2006, 2008]. The thickness of the diffusion layers can be estimated using Equations (6.7) and (6.8) [C.Y. Cheng, 2007].

$$\delta_a = \frac{D_{\mathrm{Cl}^-}}{k_{m,a}} \tag{6.7}$$

$$\delta_c = \frac{D_{\mathrm{OCl}^-}}{k_{m,c}} \tag{6.8}$$

where:			
	δ_a	Anode diffusion layer thickness	[m]
	δ_c	Cathode diffusion layer thickness	[m]
	$k_{m,a}$	Anode mass transfer coefficient	[m/s]
	$k_{m,c}$	Cathode mass transfer coefficient	[m/s]

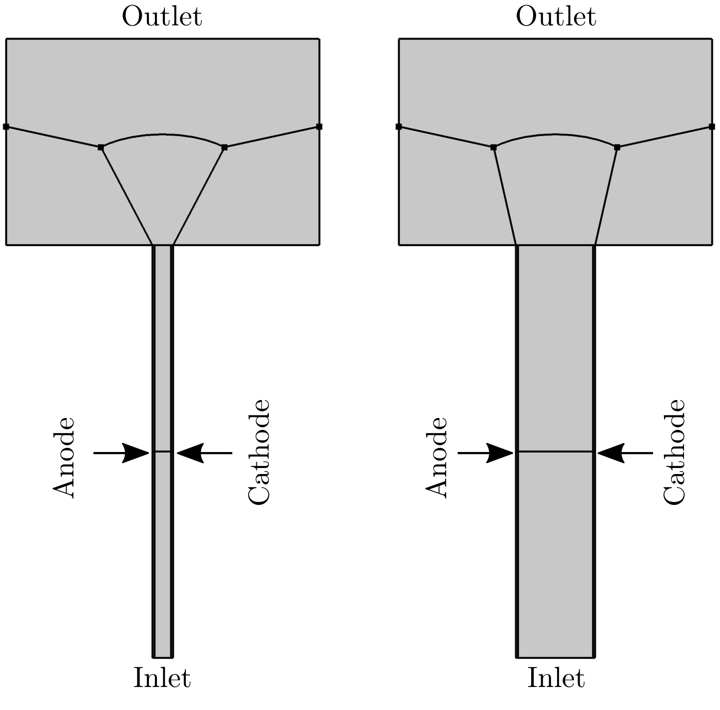

(a) $w_{gap} = 2.0\,\text{mm}$. ***(b)*** $w_{gap} = 7.68\,\text{mm}$.

Figure 6.1. 2D representations of electrochlorination cell for cell gaps of 2 mm and 7.68 mm.

The mass transfer coefficient at the hydrogen evolving cathode can be estimated using Equation (6.9) [Gijsberg and Janssen, 1989].

$$k_{m,c} = a_{factor}\left(1.3 + 1.7\boldsymbol{u}_0^{0.71}\right) \cdot 10^{\left(-5+24\left(\frac{i_{loc,\mathrm{H}_2}}{1000}\right)^{0.38}\right)} \tag{6.9}$$

where:			
	a_{factor}	Electrode surface factor	[–]
	$\boldsymbol{u}_0$	Inlet velocity	[m/s]
	i_{loc,H_2}	Local current density for hydrogen evolving electrochemical reaction	[A/m^2]

In Equation (6.9) a_{factor} is a factor that depends on the nature of the electrode surface. The nature of the electrode surface influences the mass transfer to an electrode evolving gas bubbles. For aged electrodes $a_{factor} = 1.0$, whereas for new electrodes $a_{factor} = 1.5$ [Gijsberg and Janssen, 1989], which means that the mass transfer to the hydrogen evolving electrode is the highest for a new electrode. To the best of the authors' knowledge no such expression exists for an oxygen evolving electrode, and thus it is assumed that Equation (6.9) can be used to estimate the thickness of the anode diffusion layer as well. The mass transfer coefficient at the anode is thus given by Equation (6.10).

$$k_{m,a} = a_{factor}\left(1.3 + 1.7\boldsymbol{u}_0^{0.71}\right) \cdot 10^{\left(-5+24\left(\frac{i_{loc,\mathrm{O}_2}}{1000}\right)^{0.38}\right)} \tag{6.10}$$

where:			
	i_{loc,O_2}	Local current density for oxygen evolving electrochemical reaction	[A/m^2]

In order to estimate the thickness of the diffusion layers it is estimated that the average current density will be around 100 A/m^2. At the cathode two electrochemical reactions are occurring, which produce hydrogen and consume hypochlorite. The cell is operated with a cell gap of 7.68 mm and hypochlorite is produced through chemical reactions involving species produced at or very close to the anode. Thus, due to the cell gap and the forced flow of the electrolytic solution it is assumed that the convective transport dominates and thus very small amounts of hypochlorite will be able to diffuse to the cathode. Hence, it is assumed that the cathode efficiency is 1, meaning that no hypochlorite is consumed at the cathode and all current is used to generate hydrogen bubbles. Using Equations (6.8) and (6.9), the inlet velocity of 1.8 mm/s and the fact that the electrodes are aged, since this will result in the largest diffusion layer, the thickness of the cathode diffusion layer is around 70 µm.

In industrial applications 2 to 4 % of the current density at the anode typically goes to the loss reaction resulting in the evolution of oxygen bubbles [Byrne et al., 2001]. Assuming that 3 % of the current density goes to the anode loss reaction as well as using Equations (6.7) and (6.10), the inlet velocity of 1.8 mm/s and aged electrodes, $a_{factor} = 1.0$, the anode diffusion layer is found to be around 150 µm. In order to ensure sufficiently resolution of these layers it is assumed that both the anode and cathode diffusion layers are around 200 µm and at least 10 mesh elements are placed in these layers, which increase in size moving towards the bulk flow in order to ensure smooth mesh transition.

Figures 6.2a and 6.2b show the very coarse versions of the mesh topologies used in the electrochlorination cell for 2 mm and 7.68 mm cell gaps, respectively.

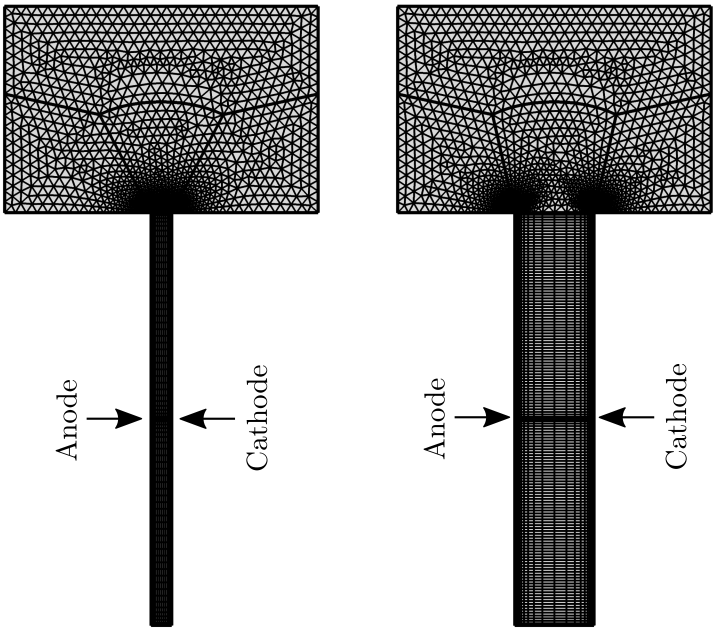

(a) $w_{gap} = 2.0\,\text{mm}$.   ***(b)*** $w_{gap} = 2.0\,\text{mm}$.

Figure 6.2. Very coarse mesh topologies used in the electrochlorination cell for cell gaps of 2 mm and 7.68 mm.

In the region between the electrodes, the cell gap, a structured mesh consisting of quadrilateral mesh elements is used due to the cell gap having a constant width, and hence not resulting in skewed mesh elements. Furthermore, the forced flow between the electrodes results in significantly steeper gradients across the channel compared to along it, especially along the electrodes. Thus, quadrilateral mesh elements with high aspect ratios are used in this region instead of having more mesh elements with aspect ratios close to unity. Finally, the use of quadrilateral mesh elements ensures great control of the mesh design in this region and hence the resolution of the diffusion layers and smooth mesh transition from these layers into the bulk flow.

The resolution of the diffusion layers and smooth mesh transition in the cell gap result in a quite large number of mesh elements in this region. Due to the design of the electrochlorination cell, the use of quadrilateral mesh elements in the entire domain means that this dense mesh between the electrodes are expropriating through the rest of the domain. This will result in an unnecessary amount of mesh elements, even in a too computational expensive mesh, in regions where much smaller gradients are occurring, and thus regions where a much smaller mesh density is required. Ipek et al. [2006, 2008] constructed two meshes, one unstructured and one structured, for the same geometry each consisting of the same number of mesh elements, 150,000. The structured mesh of quadrilateral mesh elements resulted in 2.9 million degrees of freedom, whereas the unstructured mesh consisting of triangular mesh elements resulted in 1 million degrees of freedom, thus, clearly showing the structured mesh to be significantly more computational expensive. Hence, an unstructured mesh consisting of triangular mesh elements is used in the top part of the electrochlorination cell. At the same time this mesh will ensure that not too skewed mesh elements occur, especially at the mesh expansion occurring at the top of the electrodes, when transforming the dense mesh between the electrodes into a less dense mesh above the electrodes.

As stated in Section 6.2 a compromise has to be made between the amount of stabilisation and the density of the mesh such that the correct physical behaviour is still captured in the electrochlorination cell without being too computational expensive. Based on much numerical experimentation it is assessed that for both cell gaps a minimum of about 40,000 mesh elements, resulting in approximately 400,000 degrees of freedom, is required in the entire domain with a tuning parameter, ζ, of at least 0.25 in order to obtain a consistent and convergent solution without at the same time being too computationally expensive. In this case 60 mesh elements are placed along the width of the cell gap, with 10 elements placed in each of the diffusion layers occurring at the anode and cathode. Furthermore, 360 mesh elements are placed along the height of the electrodes, thus resulting in a total of 21,600 mesh elements in the cell gap. Figure 6.3 shows the solutions for the gas volume fraction at 125 s for a cell gap of 7.68 mm with 50,000 mesh elements and tuning parameters of 0.25, 0.30 and 0.33, where in order to show the development in gas volume fraction throughout the domain the legend only goes to 5×10^{-3}.

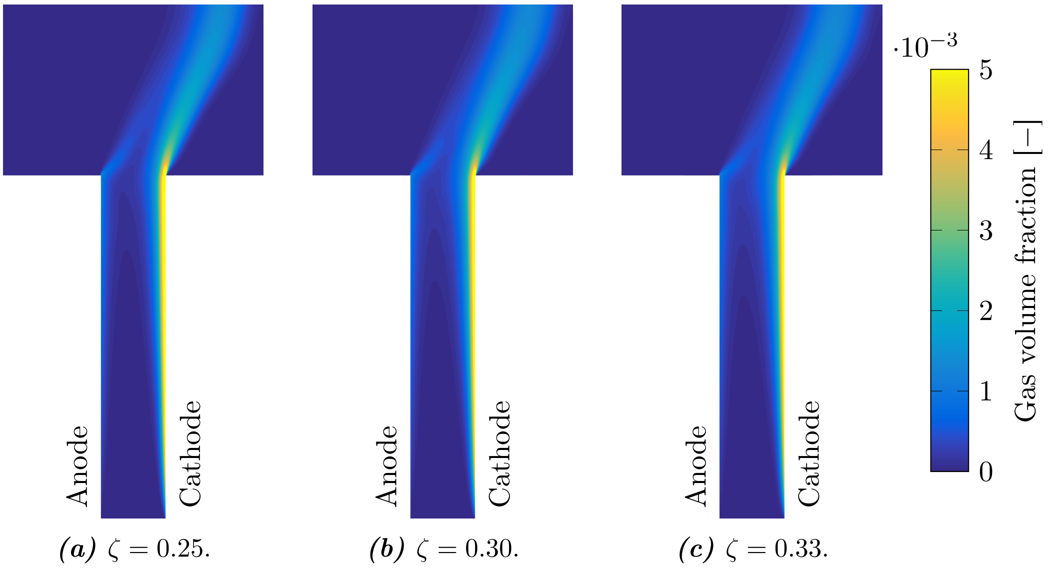

(a) $\zeta = 0.25$. ***(b)*** $\zeta = 0.30$. ***(c)*** $\zeta = 0.33$.

Figure 6.3. Time-dependent solutions at 125 s for 50,000 elements mesh with tuning parameters of 0.25, 0.30 and 0.33.

As seen from Figure 6.3 only small differences occur between the solutions. It is seen that increasing the tuning parameter increases the size of the bubble zone occurring between and above the electrodes and at the same time decreases the gas volume fraction slightly along the electrodes. Furthermore, the computational time for all three tuning parameters is between 1.5 to 2.5 hours with the highest computational time being that for $\zeta = 0.25$ and lowest for $\zeta = 0.33$. Based on the small differences between the solutions and the relative small differences in computational time it is decided to use a tuning parameter of 0.25 since this lower value brings the modified transport equation, Equation (6.6), closer to the original transport equation, Equation (6.1) and thus represents the exact solution better.

The mesh independence analyses are described in the following.

6.4 Mesh independence analyses

To ensure that the solutions obtained are reliable and do not depend on the size of the mesh elements resolving the phenomena occurring in the electrochlorination cell, mesh independence analyses are performed. In these analyses the mesh obtained in Section 6.3 makes up the coarse mesh for both cell gaps, 2 mm and 7.68 mm. Two additional meshes are constructed and included in the analysis for the large cell gap, whereas three additional meshes are included in the analysis for the small cell gap. The characteristics of each mesh is shown in Tables 6.1 and 6.2 for the large and small cell gaps, respectively.

Table 6.1. Characteristics of meshes constructed for the mesh independence analysis of the large cell gap.

Parameter	Coarse	Medium	Fine
Total number of cells in the entire domain	40000	50000	60000
Number of cells in top part	18400	20600	21600
Number of cells in cell gap	21600	29400	38400
Cells along cell gap	60	70	80
Cells in each diffusion layer	10	12	13
Cells along electrode height	360	420	480
Approximate computational time [h]	2	2.5	3
Stabilisation tuning parameter, ζ	0.25	0.25	0.25

Table 6.2. Characteristics of meshes constructed for the mesh independence analysis of the small cell gap.

Parameter	Coarse	Medium	Fine	Extra Fine
Total number of cells in the entire domain	40000	50000	60000	65000
Number of cells in top part	18400	20600	21600	22664
Number of cells in cell gap	21600	29400	38400	42336
Cells along cell gap	60	70	80	84
Cells in each diffusion layer	10	12	13	14
Cells along electrode height	360	420	480	504
Approximate computational time [h]	9	10.5	12	14
Stabilisation tuning parameter, ζ	0.25	0.25	0.25	0.25

6.4.1 Large cell gap geometry

Figures 6.4 and 6.5 show the concentration of hydroxide ions and gas phase velocity, which both are evaluated as function of time and at two positions inside the electrochlorination cell. These parameters are evaluated in order to investigate how accurate the concentrations are resolved compared to the hydrodynamic aspects. Position 1 evaluates variables very close to the cathode and Position 2 evaluates variables in the center of the bubble structure occurring above the cathode. The bubble structure is here defined as the flow of bubbles occurring above the electrodes.

From Figure 6.4 it is seen that considerable differences occur between the coarse mesh and the other constructed meshes at both positions. However, less significant differences are seen between the medium and fine meshes, thus indicating that the concentration of hydroxide ions is sufficiently resolved by the medium mesh at both positions in the electrochlorination cell.

From Figure 6.5a it is seen that significant differences occur between the coarse mesh and the other constructed meshes at Position 1, whereas relative small differences exist between the medium and fine meshes, thus indicating that the medium mesh likewise sufficiently resolves the gas velocity. Similarly, Figure 6.5b shows considerable differences in gas velocity between the coarse mesh and the other meshes at Position 2, and likewise less differences between the medium and fine meshes.

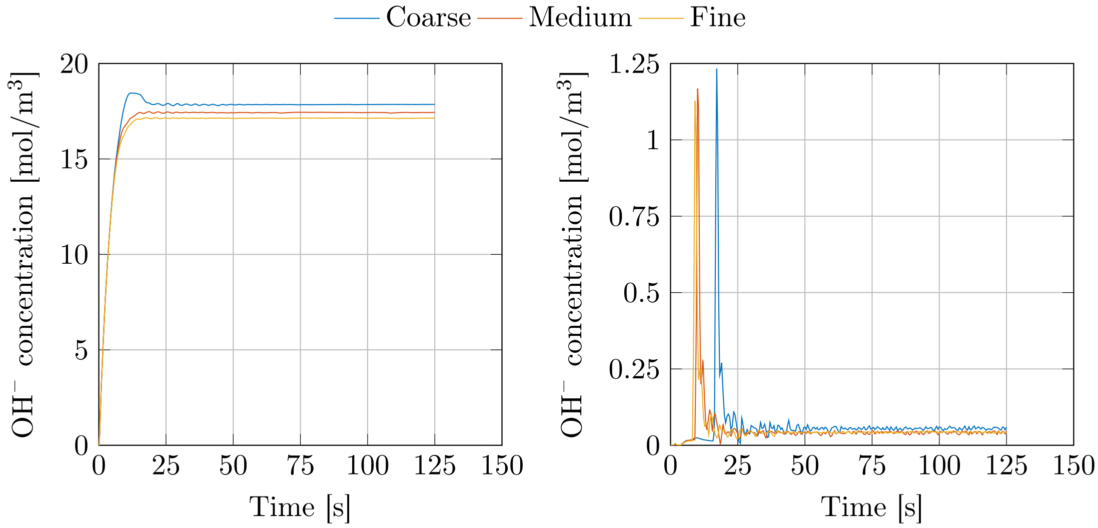

(a) Position 1.

(b) Position 2.

Figure 6.4. Hydroxide concentration as function of time at two positions in the electrochlorination cell.

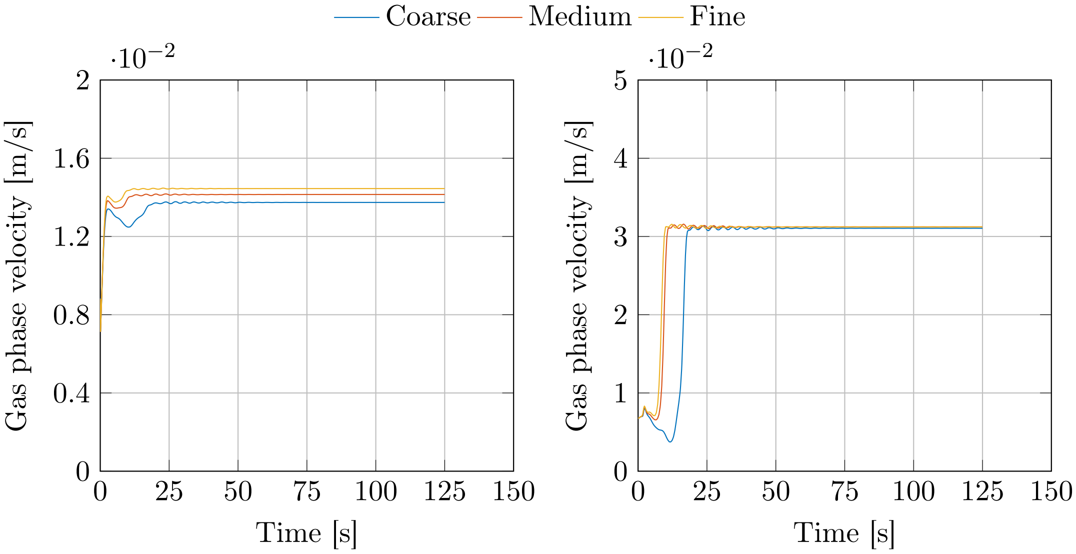

(a) Position 1.

(b) Position 2.

Figure 6.5. Gas phase velocity as function of time at two positions in the electrochlorination cell.

Figures 6.4 and 6.5, thus indicate that the resolution of the concentrations is like that of the gas velocity. Based on this analysis it is assessed that the medium mesh consisting of 50,000 mesh elements provides sufficiently accurate results with a reasonable computational time.

6.4.2 Small cell gap geometry

Figures 6.6 and 6.7 show the concentration of hydroxide ions and the velocity of the gas phase, which just like in the case of the large cell gap, are evaluated at two positions inside the electrochlorination cell. Position 1 evaluates variables very close to the cathode, whereas Position 2 evaluates variables in the center of the bubble structure.

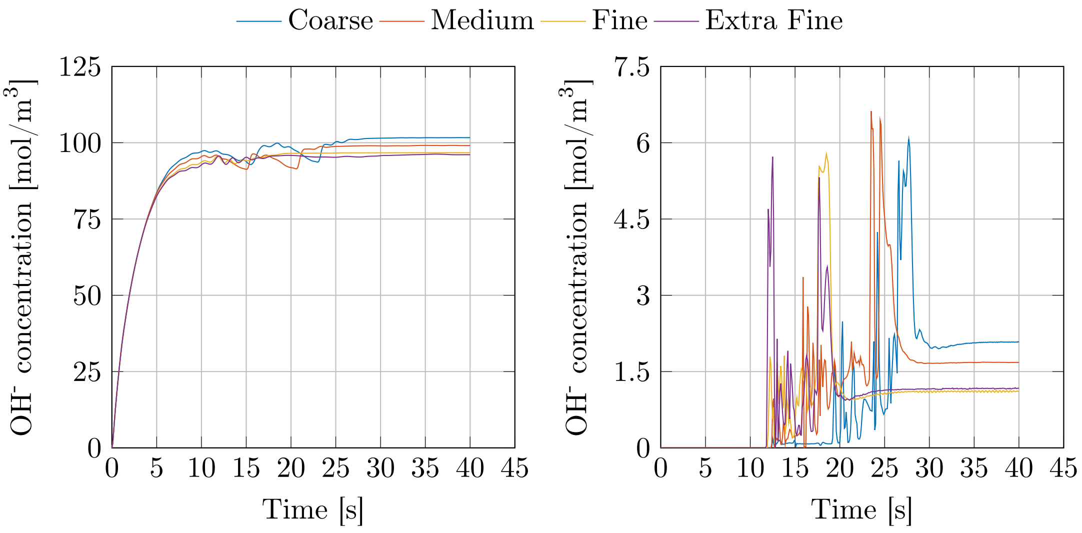

(a) Position 1. ***(b)*** Position 2.

Figure 6.6. Hydroxide concentration as function of time at two positions in the electrochlorination cell.

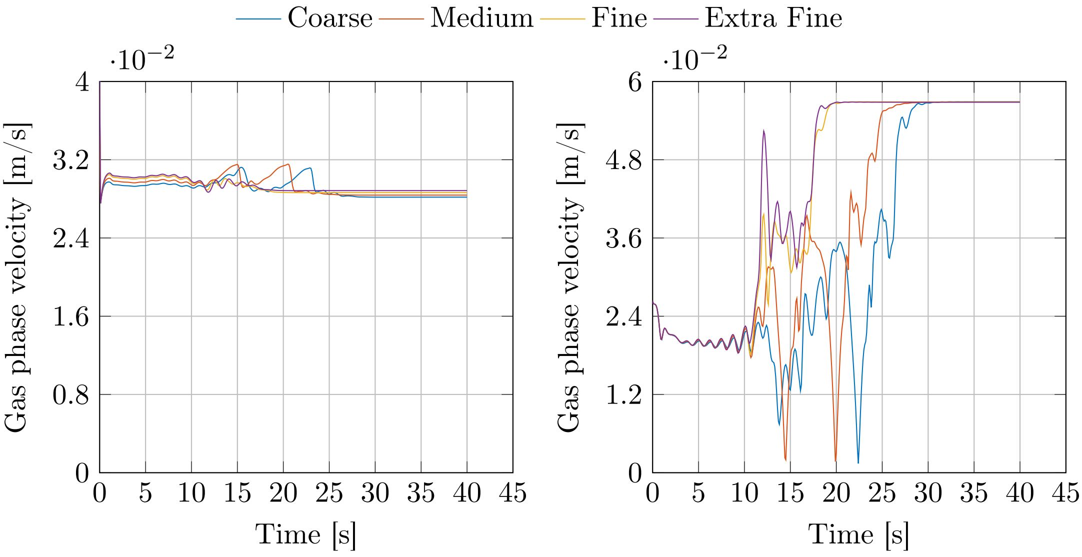

(a) Position 1. ***(b)*** Position 2.

Figure 6.7. Gas phase velocity as function of time at two positions in the electrochlorination cell.

From Figure 6.6a it is seen that significant deviations occur between the coarser meshes, coarse and medium, and the finer meshes, fine and extra fine. Moreover, it is observed that very small deviations occur between the fine and extra fine meshes, thus indicating that the concentrations at Position 1 are sufficiently resolved by the fine mesh. At Position 2, Figure 6.6b, very significant differences are likewise seen between the coarser meshes and finer meshes. Furthermore, it was observed that differences occur between the fine and extra fine meshes for simulation times between 12 to 20 s after which the two meshes are seen to predict almost the same concentration. Comparing the computational times it is assessed that the concentrations are sufficiently resolved by the fine mesh at Position 2, since almost no differences are seen between the fine and extra fine meshes at 40 s.

From Figure 6.7a it is likewise seen that considerable differences occur between the coarser and finer meshes. Very small differences are observed between the fine and extra fine meshes, thus showing that the resolution of the velocity of the gas phase is sufficient at Position 1 using the fine mesh. At Position 2, Figure 6.7b, very significant differences are observed between the coarser and finer meshes. Moreover, small differences are seen between the fine and extra fine meshes. However, almost the same development in gas phase velocity is predicted using the fine mesh compared to that predicted using the extra fine mesh. Comparing the computational time it is assessed that the gas phase velocity is sufficiently resolved by the fine mesh.

Based on this analysis it is assessed that the fine mesh consisting of 60,000 mesh elements provides sufficiently accurate results with a reasonable computational time compared to the others. The models made in COMSOL Multiphysics are found in the folder containing digital copies of the files, that can be received by contacting Anders Christian Olsen and Henrik Sørensen whose emails can be found in the Preface.

The small cell gap geometry with the fine mesh will be used for further investigations in Chapter 8, after the modelling has been validated using the large cell gap geometry with the medium mesh in the following chapter.

Seventh Chapter

Model validation

In order to test the validity, as well as discover any weaknesses of the model, model results obtained using the geometry with 7.68 mm cell gap are compared to experimental data obtained using the setup and procedures described in Appendix B. After comparing the model to the experimental data a sensitivity analysis is conducted to investigate and validate the behaviour of the model as the inputs are varied. The validation of the modelling is done for the geometry with 7.68 mm cell gap as useful experimental data cannot be acquired for high current densities due to bubble clouding in the actual electrochlorination cell, which would generally be the case when the cell gap is lowered. Using the experimental data presented in Appendix B a mean bubble size of 62.4 µm is found, which is used for the modelling. Comparisons are made between polarisation curves, bubble structure in the electrolytic solution, true bubble velocities and gas volume fraction. Comparisons of true bubble velocity and gas volume fraction are made at different horizontal positions inside the electrochlorination cell. Firstly, comparisons are made between the polarisation curves since significant deviations between these have a great influence on the current density predicted by the model, which in turn influences the amount of gas bubbles produced. If such deviations are observed between the model and the electrochlorination cell, the model is fitted by adjusting parameters influencing the electrochemistry. Should the production of gas bubbles in the model considerably exceed that in the cell significant deviations can be expected for comparisons of bubble structure and true velocities as well as gas volume fractions.

In this chapter comparisons between the model and experimental data will be made in the zooms shown in Figure G.2a and Figure G.2b in Appendix G.

7.1 Polarisation curve comparisons

Figure 7.1 shows the polarisation curves obtained for the model and the electrochlorination cell in the experimental setup. For the model the cell potential is given as input and thus the current density is an output. For the cell, the current density has been set and the corresponding cell potential read off.

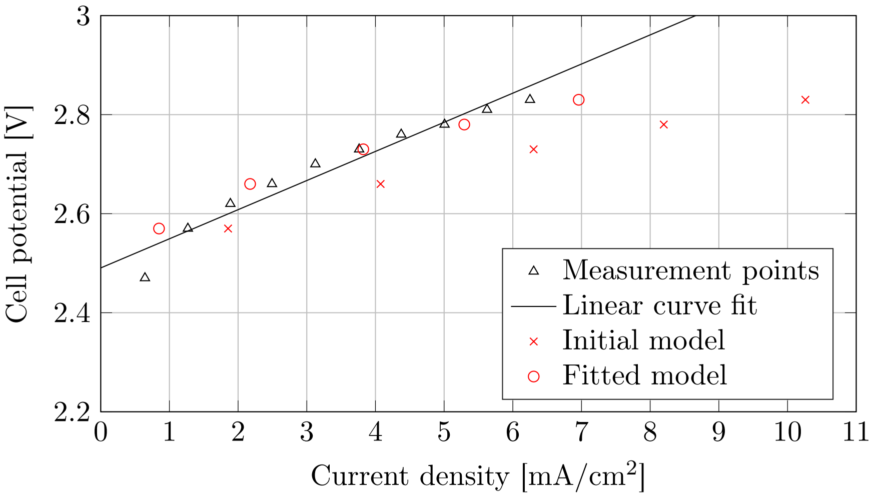

Figure 7.1. Measured polarisation curve for the electrochlorination cell along with the corresponding curve predicted by the model with the equilibrium potentials stated in Section 5.1.3 and by C.Y. Cheng [2007].

As seen from Figure 7.1, there are considerable differences between the polarisation curves, where the initial model overestimates the current density at a given cell potential. As stated above such a deviation will result in significant deviations between the model and the experimental data regarding bubble velocities and structure, as well as gas volume fraction. In order to fit the polarisation curve of the model to that of the experimental data, inputs influencing the electrochemistry of the model are to be changed. As stated in Section 5.1.3, C.Y. Cheng [2007] showed that the pH values close to the anode and cathode are around 2 and 12, respectively. At these pH values the equilibrium potentials were shown not to vary much from those at a pH value of 7. However, in order to try and fit the polarisation curve of the model to that measured, the equilibrium potentials stated by C.Y. Cheng [2007] are implemented. The equilibrium potentials used in Section 5.1.3 and those found by C.Y. Cheng [2007] are given in Table 7.1.

Table 7.1. List of equilibrium potentials used in Section 5.1.3 and found by C.Y. Cheng [2007].

Electrochemical Reaction	(C 5.1)	(C 5.2)	(C 5.3)	(C 5.4)
Section 5.1.3	1.36 V	1.23 V	−0.83 V	0.88 V
[C.Y. Cheng, 2007]	1.46 V	1.10 V	−0.80 V	0.75 V

As seen from Figure 7.1, the equilibrium potentials found by C.Y. Cheng [2007] result in a better fit between the model and the experimental data. In this case only slight differences occur between the model and experimental data. This seems to indicate that the pH values close to the anode and cathode in the electrochlorination cell are around 2 and 12, respectively. Due to the better fit between the model and experimental data, it is decided to use the equilibrium potentials found by C.Y. Cheng [2007] and this fitted model will be used in the further validation described in the following sections.

7.2 Bubble structure and velocity comparisons

Figure 7.2 shows the contours of the bubble velocity magnitude predicted by the model and measured with the flow visualisation technique described in Appendix B.2.

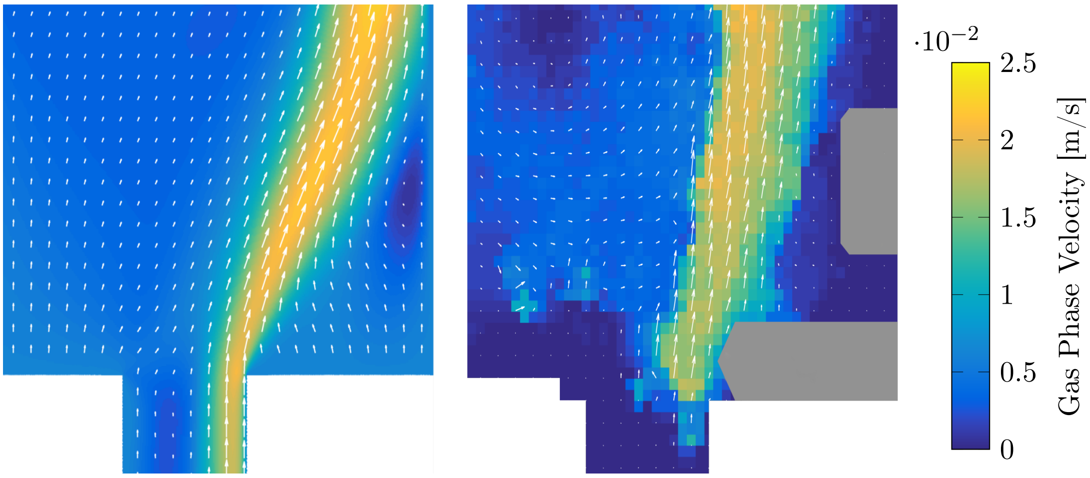

(a) Model. ***(b)*** Flow visualisation.

Figure 7.2. Bubble velocity magnitudes predicted by the model for a bubble size of 62.4 µm and obtained by the flow visualisation technique, at a cell voltage of 2.66 V and an inlet liquid flow rate of 2 L/h.

Comparing the velocity magnitudes in Figures 7.2a and 7.2b, it is seen that the predicted bubble structure occurring above the cathode resembles that occurring in the actual small scale electrochlorination cell, where the bubbles are seen to flow to the right side of the cell. However, this displacement of the bubble structure is predicted by the model to be greater than that visualised in the constructed electrochlorination cell. As stated in the Conference Paper (Appendix A), the bubble structure occurring in the actual cell consists of bubbles of different sizes, which are seen to grow in size moving from the right side of the cell and towards the cathode surface plane and bulk flow. This means that the larger bubbles closer to the cathode surface plane will move faster and are less affected by the liquid flow, thus making the bubble structure in the actual electrochlorination cell displace less to the right than that predicted by the model, where a constant bubble size is used.

Furthermore, comparing velocities in the bubble structure it is seen that the velocity predicted by the model resembles that in the constructed electrochlorination cell. In much of the predicted bubble structure a velocity of approximately 22×10^{-3} m/s is occurring, whereas a velocity of about 20×10^{-3} m/s occurs in much of the bubble structure captured by the flow visualisation technique. Moreover, in both cases it is seen that the bubble velocity increases from the bottom of the bubble structure towards the outlet.

In the left side of the electrochlorination cell as well as the bottom right corner the model predicts the velocity magnitude of the bubbles to be upwards, which does not agree with the velocity magnitudes obtained by the flow visualisation technique. The reason for this behaviour is found in the way that the slip velocity between the two phases is formulated for the bubbly two-phase flow model. Evaluating Equations (5.47) to (5.50) described in Section 5.4 the following formulation for the slip velocity can be derived:

$$\boldsymbol{u}_{slip} = \frac{\left[\boldsymbol{g}\left(\rho_l - \rho_g\right) - \nabla p\right] {d_b}^2}{12\mu_l} \tag{7.1}$$

It can be observed that the slip velocity is defined in terms of the buoyancy force and the pressure gradient. Having a slip velocity pointing in the positive y-direction shows that the pressure gradient inside the cell is dominated by the buoyancy force, whose high magnitude is given by the large density difference between the two phases. Figure 7.3 visually proves that the slip velocity between the two phases is constant, with a magnitude of 0.63×10^{-2} m/s and directed in the positive y-direction throughout the domain, regardless of the presence of gas bubbles.

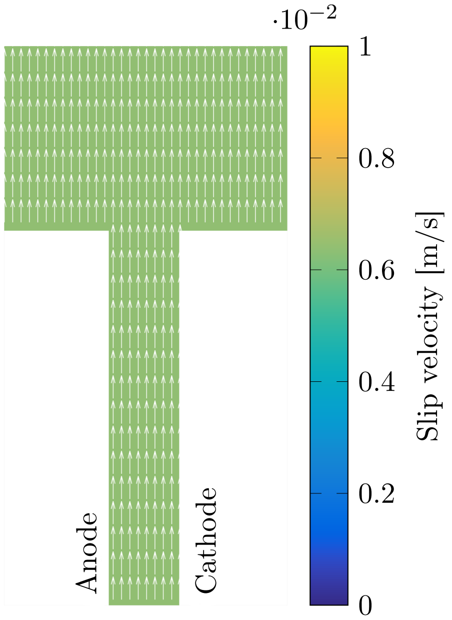

Figure 7.3. Slip velocity magnitude (0.63×10^{-2} m/s) and direction predicted by the model.

Further velocity comparisons are made between the model and the bubble tracking procedure described in Section 4.5, which is used for estimation of the y-component of the bubble velocity. As described in Section 4.2, the FOD of the telecentric lens is placed above and in parallel with the plane of the cathode. Thus, only comparisons are made between the y-components of the bubble velocity. Figure 7.4 shows the y-component of the bubble velocity predicted by the model in the entire domain and within the FOD of the telecentric lens at four horizontal positions, moving from the cathode surface plane to the right in the electrochlorination cell, A/E = 0.10, 0.16, 0.22 and 0.28. Figure 7.5 shows the y-component of the mean bubble velocity estimated by the bubble tracking procedure for a size group of 50 to 75 µm at the same horizontal positions. Each horizontal position is located in the centre of the coloured rectangles, which each indicates the FOD of the applied telecentric lens, at each position.

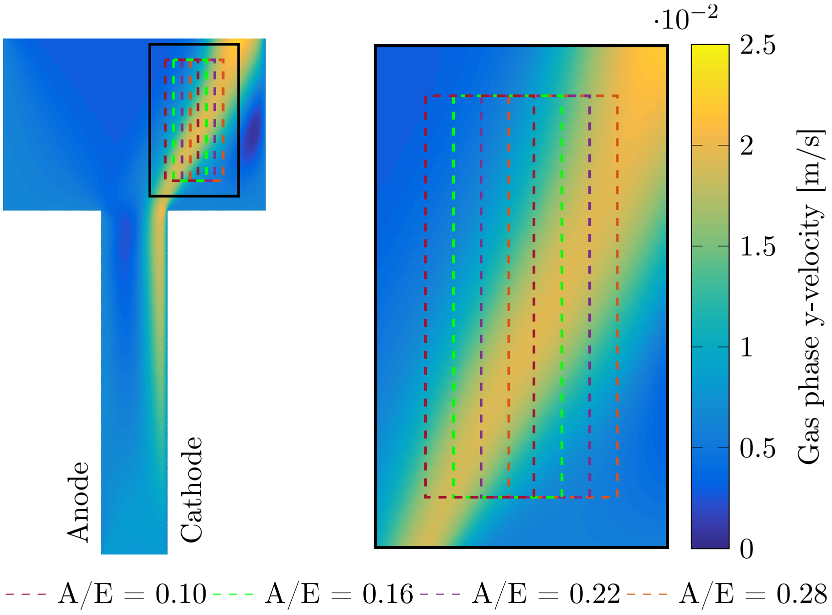

Figure 7.4. y-component of the bubble velocity predicted by the model in the entire domain and within the FOD, the coloured rectangles, of the telecentric lens at a cell voltage of 2.66 V and four horizontal positions across the bubble structure using a mean bubble size of 62.4 µm and an inlet liquid flow rate of 2 L/h.

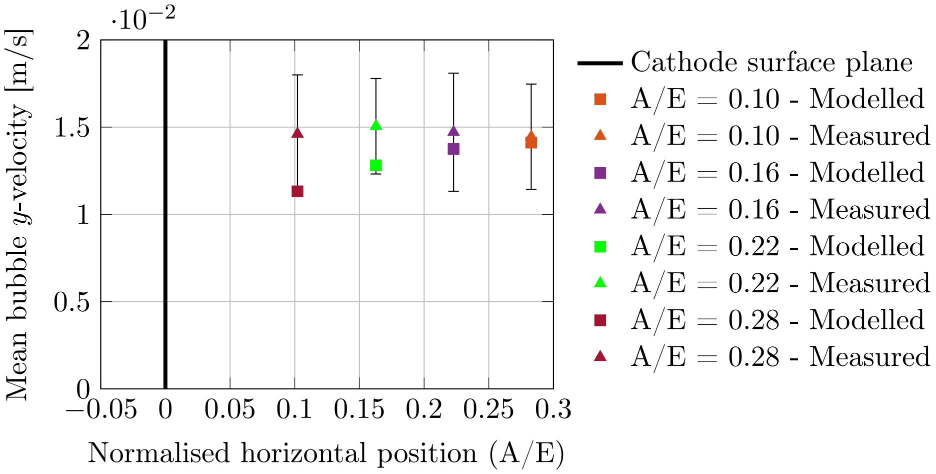

Figure 7.5. Mean y-component of the bubble velocity predicted by the model for a mean bubble size of 62.4 µm and estimated by the bubble tracking procedure for a size group of 50 to 75 µm at four horizontal positions across the bubble structure, a cell voltage of 2.66 V and an inlet liquid flow rate of 2 L/h. The vertical line intervals indicate the standard deviations at each horizontal position.

From Figure 7.4 it is seen that the y-component of the bubble velocity predicted by the model varies approximately between 1×10^{-2} to 2×10^{-2} m/s across all horizontal positions. This is in good agreement with the measured y-component of the bubble velocity in Figure 7.5, where a mean velocity of approximately 1.5×10^{-2} m/s with a standard deviation of about 0.3×10^{-2} m/s is found.

Averaging over each coloured rectangle, FOD, the mean y-component of the bubble velocity predicted by the model at each horizontal position is found. As seen from

Figure 7.5 the mean y-component of the bubble velocity predicted by the model lies within the standard deviations of the mean velocities obtained by the bubble tracking procedure at all four horizontal positions. However, it is seen that the mean y-component of the bubble velocity predicted by the model deviates more and more from that estimated by the bubble tracking procedure, when moving towards the cathode surface plane. As shown in Figure 7.2 the bubble structure predicted by the model is displaced more to the right compared to that visualised in the electrochlorination cell. This means that larger regions of higher velocity appear in the FODs closer to the cathode surface plane for the bubble tracking procedure compared to the same FODs for the model. Thus, resulting in higher mean y-components of the bubble velocity for the bubble tracking procedure at horizontal positions close to the cathode surface plane.

In the following, comparisons are made between the gas volume fractions predicted by the model and those obtained using the digital image processing method described in Section 4.4.

7.3 Gas volume fractions comparisons

Comparisons of gas volume fraction are made at two cell voltages, 2.57 V and 2.66 V, both at an inlet liquid flow rate of 2 L/h. Figure 7.6 shows the gas volume fraction predicted by the model in the entire domain and within the FODs of the telecentric lens at a cell voltage of 2.57 V and four horizontal positions. Figure 7.7 shows the gas volume fraction estimated by the digital image processing method at the same cell voltage and horizontal positions. Likewise, Figures 7.8 and 7.9 show the gas volume fraction obtained by the model and digital image processing method at a cell voltage of 2.66 V and the same four horizontal positions, respectively.

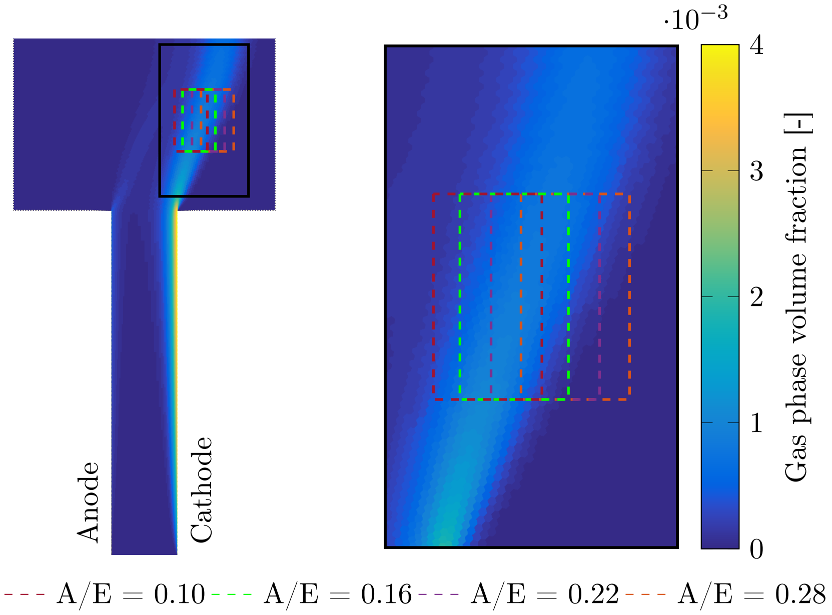

Figure 7.6. Gas volume fraction predicted by the model in the entire domain and within the FOD, coloured rectangles, of the telecentric lens at a cell voltage of 2.57 V, an inlet liquid flow rate of 2 L/h and four horizontal positions across the bubble structure using a bubble size of 62.4 µm.

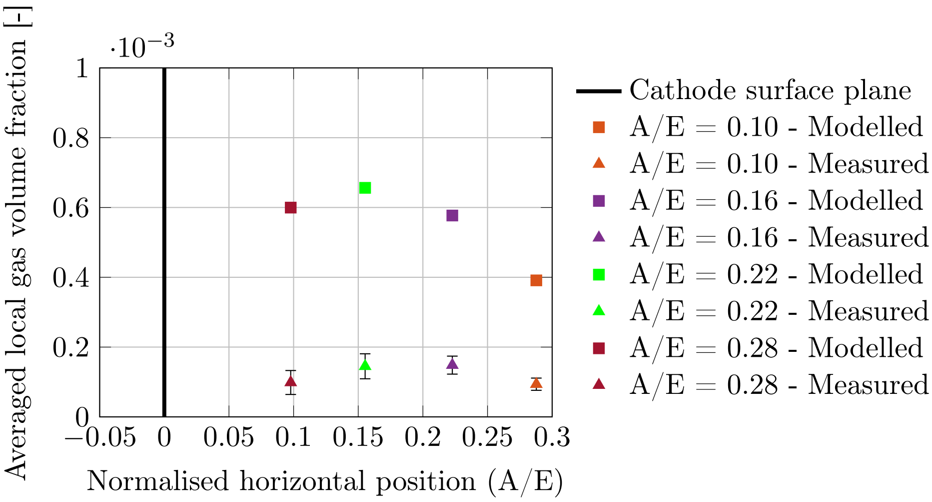

Figure 7.7. Averaged gas volume fraction predicted by the model using a bubble size of 62.4 µm and estimated by digital image processing method at a cell voltage of 2.57 V, an inlet liquid flow rate of 2 L/h and four horizontal positions across the bubble structure. The vertical line intervals indicate the standard deviations at each horizontal position.

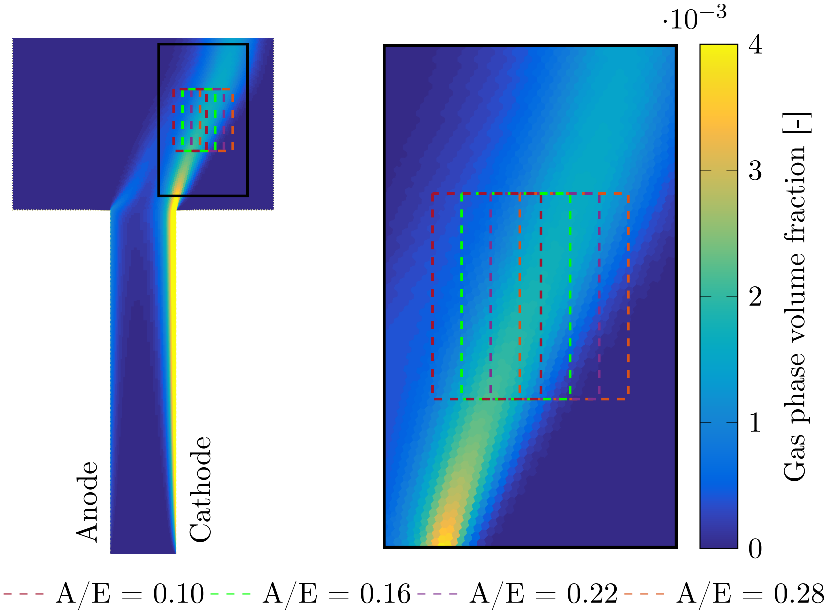

Figure 7.8. Gas volume fraction predicted by the model in the entire domain and within the FOD, the coloured rectangles, of the telecentric lens at a cell voltage of 2.66 V, an inlet liquid flow rate of 2 L/h and four horizontal positions across the bubble structure using a bubble size of 62.4 µm.

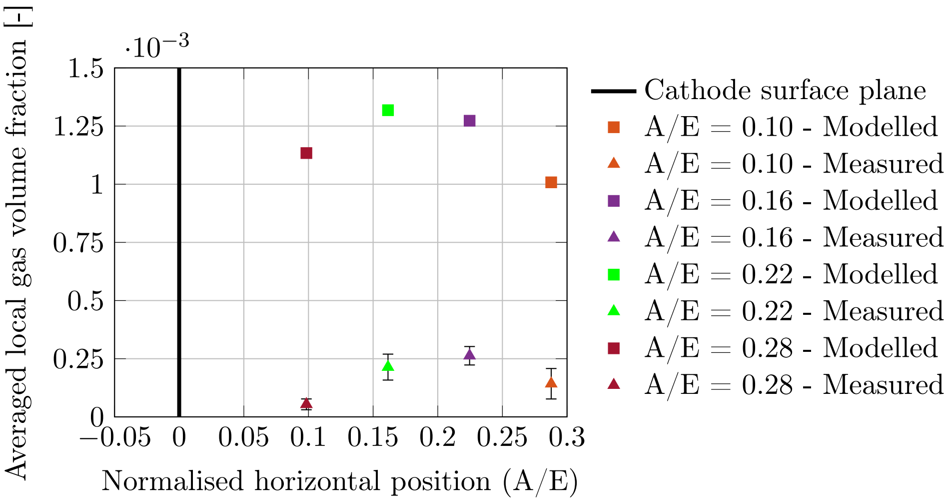

Figure 7.9. Averaged gas volume fraction predicted by the model using a bubble size of 62.4 µm and estimated by digital image processing method at a cell voltage of 2.66 V, an inlet liquid flow rate of 2 L/h and four horizontal positions across the bubble structure. The vertical line intervals indicate the standard deviations at each horizontal position.

As seen from Figures 7.7 and 7.9, similar behaviour exists between the model and the actual electrochlorination cell, where the gas volume fraction increases until reaching a horizontal position of 0.16 or 0.22 after which the gas volume fraction is seen to decrease again. However, the model is seen to significantly overestimate the gas volume fraction compared to that obtained by the digital image processing method. One possible reason for these significant deviations is believed to be the digital image processing method applied in this study. As stated in Section 4.4.2, in the processing of the images captured of the bubbles occurring inside the electrochlorination cell at the different horizontal positions overlapping bubbles are taken out since a method of including these without breaking the edges of these bubbles and other bubble contours have not been found. Thus, bubbles which would contribute to the gas volume fraction at a given horizontal position are taken out and not accounted for, hence lowering the gas volume fraction at the given horizontal position. A second reason is believed to be the material of the cathode inserted in the constructed electrochlorination cell. If the nature of the cathode surface makes some of the formed hydrogen bubbles stick to the cathode surface these bubbles will grow further due to coalescence with smaller bubbles or supersaturated zones close to the bubbles [Boissonneau and Byrne, 2000; Abdelouahed et al., 2014]. As the bubble reaches a certain size it detaches from the surface, and due to its size it ascends through the electrochlorination cell at a high velocity. As described in Section 4.2 an image is captured every 10 s in order to ensure that the same bubble does not appear in the data set twice. This means that the mass going into the production of the larger bubbles, getting stuck on the surface of the cathode, is not necessarily captured due to the 10 s dead time between each image. Such phenomena is not included in the model, which means that every bubble produced instantly detaches from the surface. This, in turn, results in the gas volume fraction predicted by the model to appear to be significantly higher than that estimated by the digital image processing method if the larger surface detaching bubbles are not captured.

Further investigations with respect to gas volume fraction can be made to better understand the difference between measured and modelled data. The gas volume fraction is determined at the exit of the cell gap, under the main assumption that the gas bubbles do not stick to the surface. The gas volume fraction is calculated according to Equation (7.2):

$$\phi_g = \frac{\bar{u}_{g,sf}}{\bar{V}_g} \tag{7.2}$$

where:			
	$\bar{V}_g$	Average true velocity of gas phase	[m/s]
	$\bar{u}_{g,sf}$	Average superficial velocity of gas phase	[m/s]

The true velocity of the gas phase is estimated at the exit of the cell gap using the data shown in Figure 7.2. The superficial velocity is expressed by Equation (7.3), where the mass flow of the gas phase is determined from Faraday's law of electrolysis, Equation (5.54), repeated below.

$$\bar{u}_{g,sf} = \frac{\dot{m}_{\mathrm{H}_2}}{\rho_{\mathrm{H}_2} A_{electrode}} \tag{7.3}$$

$$\dot{m}_{\mathrm{H}_2} = \frac{\boldsymbol{i}_l A_{gap} \nu}{n_{\mathrm{e}^-} F} \cdot M_{\mathrm{H}_2} \tag{5.54}$$

where:			
	$\dot{m}_{\mathrm{H}_2}$	Mass flow of hydrogen	[kg/s]
	ρ_{H_2}	Density of hydrogen	[kg/m^3]
	$A_{electrode}$	Electrode area	[m^2]
	$\boldsymbol{i}_l$	Electrode current density	[A/m^2]
	A_{gap}	Cell gap area in the xz-plane (See Figure 4.3)	[m^2]
	ν	Stoichiometric coefficient. Here $\nu = 1$	[–]
	n_{e^-}	Number of electrons. Here $n_{\mathrm{e}^-} = 2$.	[–]
	F	Faraday's constant	[C/mol]
	M_{H_2}	Molar mass of hydrogen	[kg/mol]

At the exit of the cell gap an average gas volume fraction of 4.9×10^{-3} is estimated from the flow visualisation, whereas the model predicts a volume fraction of 2.2×10^{-3} for the same gap width. Hence, it is observed that the model underpredicts the gas volume fraction in this case. However, this estimated average gas volume fraction is in much better agreement with that predicted by the model, than the volume fractions measured by the TDIM. The mean true velocity of 14 mm/s predicted by the model is higher than the measured mean true velocity of 12.6 mm/s. The higher true velocity predicted by the model, thus results in a lower gas volume fraction as given by the combined continuity equation for the model. The model and experimental data of Figure 7.2 are both obtained at a cell voltage of 2.66 V. Comparing the current densities at this cell voltage in the polarisation curve, shown in Figure 7.1, it is seen that the current density predicted by the model is less than that measured in the actual electrochlorination cell. This means that the mass flux of hydrogen from the cathode predicted by the model is less than that in the actual cell, which in turn could explain some of the differences between the estimated and predicted gas volume fractions. This estimation, however, supports the possible reasons stated earlier, regarding the image method applied and the nature of the cathode surface.

In the following a sensitivity analysis is performed in order to investigate and validate the behaviour of the model as the inputs are varied.

7.4 Sensitivity analysis

For the sensitivity analysis it is chosen to vary the bubble size, electrical conductivity of the electrolytic solution, inlet flow rate and salt concentration. These are parameters influencing the bubbly two-phase flow and electrochemistry.

7.4.1 Bubble size

Figure 7.10 shows solutions for the gas phase velocity for bubble sizes of 50.0 µm, 62.4 µm and 75.0 µm at 125 s.

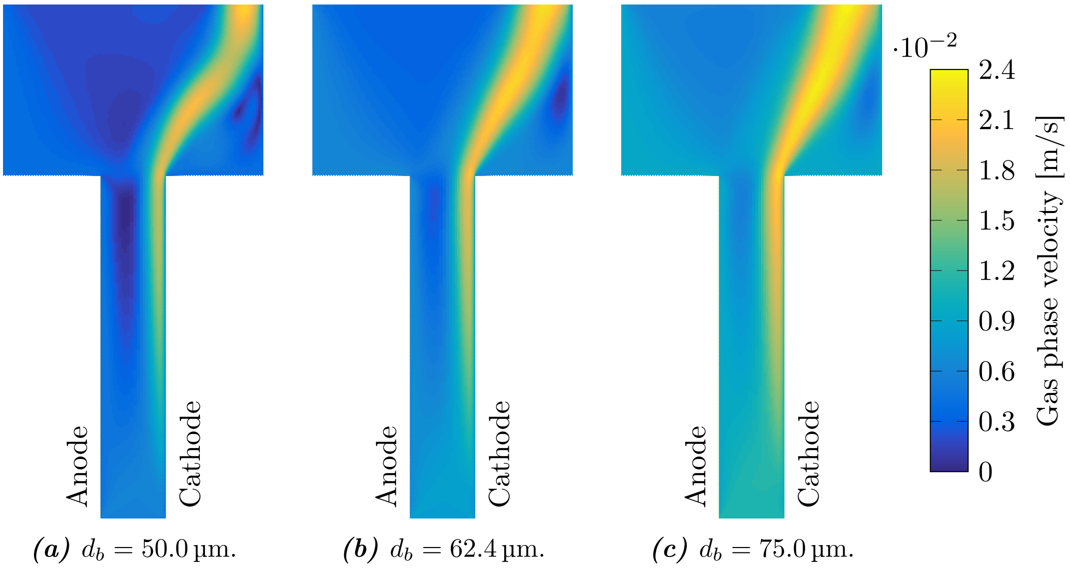

(a) $d_b = 50.0\,\mu\text{m}$. ***(b)*** $d_b = 62.4\,\mu\text{m}$. ***(c)*** $d_b = 75.0\,\mu\text{m}$.

Figure 7.10. Time-dependent solutions at 125 s for gas phase velocities with bubble sizes of 50.0 µm, 62.4 µm and 75.0 µm.

Comparing the contours of Figure 7.10 it is seen that the gas phase velocity increases with increasing bubble size. This behaviour is consistent with that expected for increasing bubble sizes. The reason for the behaviour shown by the model can be explained by the slip velocity, shown in Equation (7.1) and given again below for easy reference.

$$\boldsymbol{u}_{slip} = \frac{\left[\boldsymbol{g}\left(\rho_l - \rho_g\right) - \nabla p\right] {d_b}^2}{12\mu_l} \tag{7.1}$$

Equation (7.1) shows that the slip velocity indeed increases with increasing bubble size as observed from Figure 7.10. At the same time, it is seen that the displacement to the right of the bubble structure becomes less significant for an increasing bubble size. This behaviour is consistent with the bubble behaviour described in the Conference Paper by the authors, Appendix A, where it is seen that the mean bubble size increases moving across the bubble structure from the right side of the electrochlorination cell towards the cathode surface plane for a stagnant flow. This means that small bubbles are displaced furthest to the right, thus being farthest from the cathode surface plane and large bubbles are displaced the least, hence staying closer to the cathode surface plane.

7.4.2 Conductivity of solution

Figure 7.11 shows the potential in the electrolytic solution across the cell gap for three different conductivities.

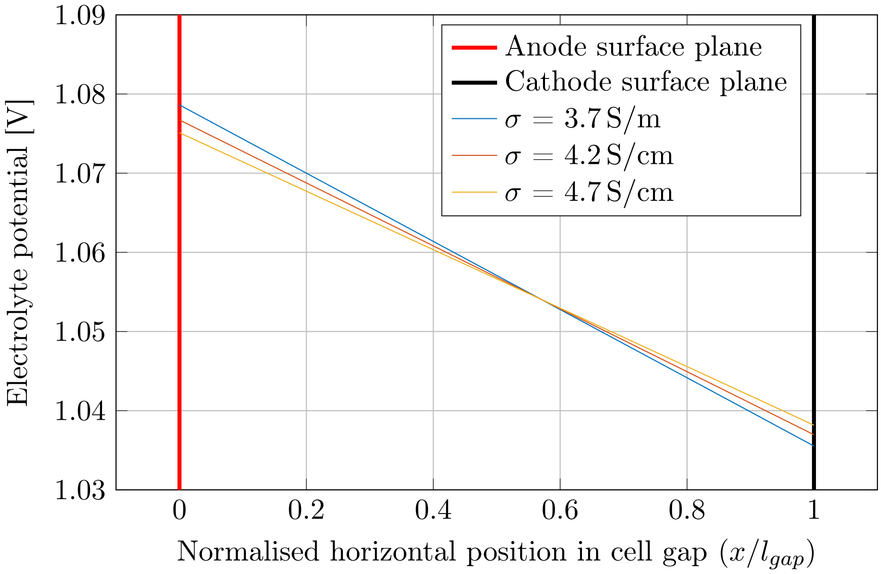

Figure 7.11. Potential in electrolytic solution as function of cell distance between the electrodes for different conductivities of the electrolytic solution.

As seen from Figure 7.11 the potential gradient decreases linearly through the electrolytic solution moving across the cell gap, from the anode surface plane to that of the cathode, for increasing conductivities of the electrolytic solution, 3.7 to 4.7 S/m. An expression similar to Ohm's law, given by Equation (5.10), relates the current density to the conductivity of the electrolytic solution and potential gradient across the solution.

$$\boldsymbol{i}_l = -\sigma \nabla \Phi_l \tag{5.10}$$

As seen from Equation (5.10), as the conductivity of the electrolytic solution decreases, the potential gradient across the solution increases for a constant current density. This behaviour is consistent with that expected for increasing salt concentrations, since an increase in salt concentration will reduce the ohmic losses in the electrolytic solution, thus enhancing the electrical conductivity through the solution.

7.4.3 Inlet flow rate

Figure 7.12 shows the liquid flow structure and velocity magnitude, as the inlet flow rate is varied from 1 to 3 L/h.

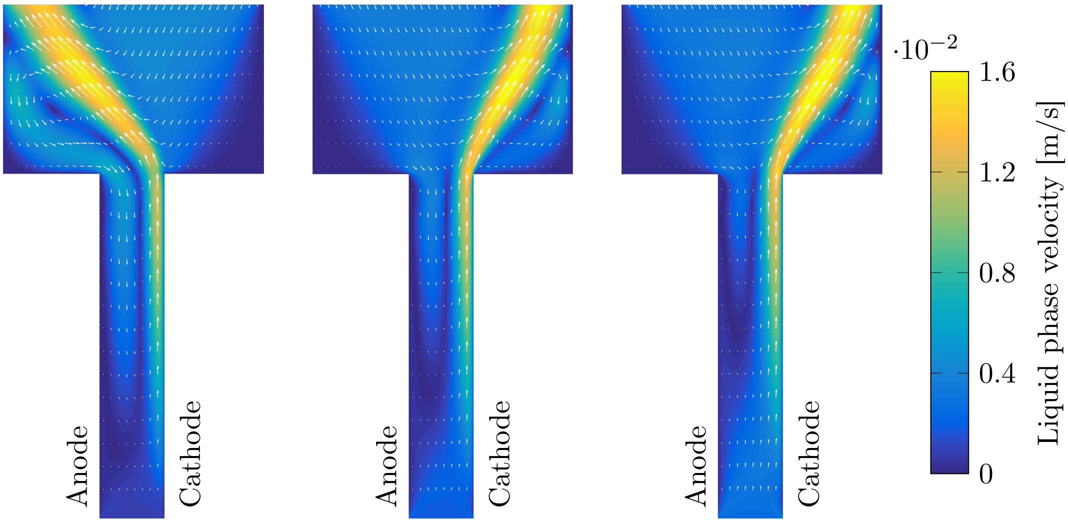

(a) $\dot{Q} = 1\,\mathrm{L/h}$. *(b)* $\dot{Q} = 2\,\mathrm{L/h}$. *(c)* $\dot{Q} = 3\,\mathrm{L/h}$.

Figure 7.12. Liquid phase velocity magnitude for different inlet flow rates.

An increased input flow rate dictates a higher inlet velocity of the liquid phase. This can be observed in Figure 7.12, where at the bottom of the cell gap the magnitude of the velocity is higher and the higher velocity region is extended more towards the anode in the cell with a flow rate of 3 L/h, compared to the cases for 1 and 2 L/h. The same pattern is seen further up the cell gap, where the liquid phase velocity decreases towards the anode, but keeps a higher magnitude compared to the case of 2 L/h. As a consequence of an increased velocity, the recirculation zone inside the cell gap is reduced. The opposite is observed in the cell for an inflow rate of 1 L/h, where the velocity at the inlet of the cell is lower, allowing the recirculation zone to grow towards the inlet of the cell.

Furthermore, the model predicts a shift in the liquid flow structure for an inlet flow rate of 1 L/h. This is expected to be caused by the lower momentum of the liquid phase. The momentum of the gas phase, thus, has the possibility of shifting the flow to the left side of the cell when leaving the cell gap.

7.4.4 Sodium chloride concentration

Figure 7.13 shows the changes in Cl^- concentration as the NaCl concentration of the electrolytic solution is changed to values below and above the value of $513.3\,\mathrm{mol/m^3}$ originally implemented in the model. The concentrations have been normalised in terms of the maximum chloride ion concentration occurring in each investigated case.

For a Cl^- concentration of $100\,\mathrm{mol/m^3}$ the Cl^- concentration decreased from its bulk value towards the anode, reaching a value of $73\,\mathrm{mol/m^3}$. For the same chloride ion concentration C.Y. Cheng [2007] reported a similar behaviour and moreover, the concentration was observed to decrease rapidly along the height of the anode. Looking at Figure 7.13a the same phenomena is predicted by the model, the oxidation of Cl^- occurring at a greater extent towards the top of the anode.

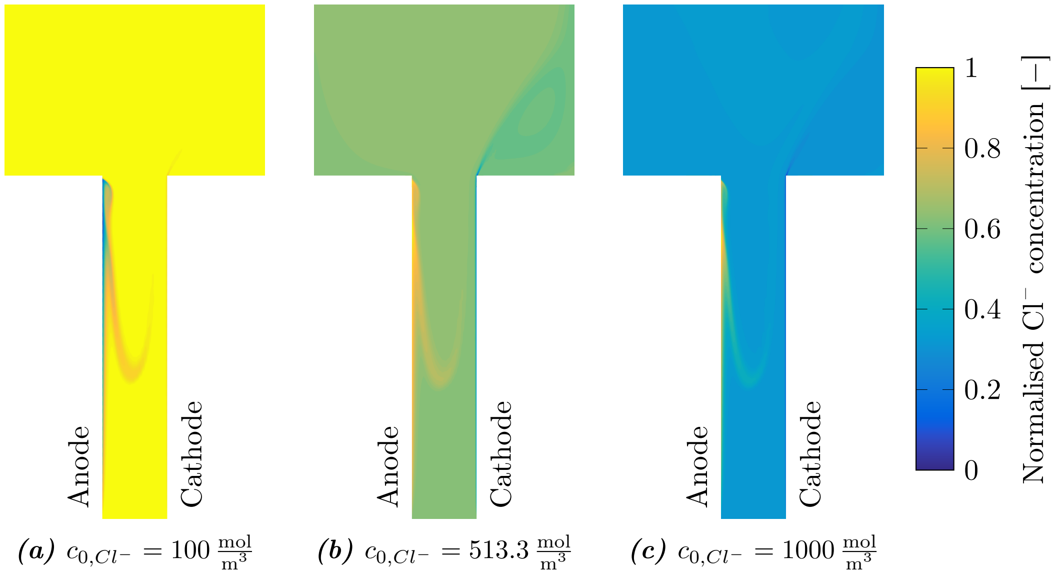

(a) $c_{0,Cl^-} = 100\,\frac{\mathrm{mol}}{\mathrm{m}^3}$ ***(b)*** $c_{0,Cl^-} = 513.3\,\frac{\mathrm{mol}}{\mathrm{m}^3}$ ***(c)*** $c_{0,Cl^-} = 1000\,\frac{\mathrm{mol}}{\mathrm{m}^3}$

Figure 7.13. Normalised Cl$^-$ concentration for different NaCl inlet concentrations.

As the concentration of NaCl is increased, the concentration of dissociation products, Na$^+$ and Cl$^-$, is expected to increase as well. The chloride ions, being negatively charged, migrate towards the positive anode. Although at the anode an oxidation of chloride ions occurs, the mass flux of consumed chloride ions is exceeded by the mass flux of chloride ions transported towards the anode surface by a combined effect of migration, diffusion and convection, causing an accumulation of chloride ions. As the chloride ions accumulate, the Cl$^-$ concentration at the anode increases and exceeds the Cl$^-$ bulk concentration, thus a diffusion of chloride ions takes place towards the bulk flow. Having concentration-dependent current densities, the accumulation with electrode height increases the current density for the electro-oxidation of chloride ions. As shown in Figures 7.13b and 7.13c, this accumulation occurs for inlet chloride ion concentrations of 513.3 mol/m^3 and 1000 mol/m^3, where the Cl$^-$ concentration increases by 20% and 50%, respectively.

7.5 Summary

As seen in this chapter, the polarisation curve predicted by the fitted model resembles that obtained for the actual electrochlorination cell. Likewise, it was seen that similar bubble structures and velocities occur between the model and experimental methods used to obtain these. The gas volume fractions predicted by the model were observed to considerably exceed those obtained using the digital image processing method described in Chapter 4. As discussed, possible reasons for these deviations could be found in the processing of the acquired images and the nature of the cathode inserted in the actual electrochlorination cell. Finally, the sensitivity analysis showed correct behaviour of the model when bubble size, solution conductivity, inlet flow rate, and salt concentration were varied. Thus, it is concluded that the modelling of the electrochlorination cell is capable of capturing the phenomena occurring in the actual cell.

In the following investigations are conducted using the geometry with a cell gap of 2 mm.

Eighth Chapter

Small cell gap investigations

This chapter serves to describe and analyse the behaviour of the electrochlorination cell model for a cell gap of 2 mm. In Chapter 7 a mean bubble size of 62.4 µm was used to validate the model. This mean bubble size was found for a 7.68 mm cell gap and current densities of $1.25\,\mathrm{mA/cm^2}$ and $2.5\,\mathrm{mA/cm^2}$, corresponding to cell potentials of 2.57 V and 2.66 V, respectively. In order to resemble industrial applications the cell gap is lowered to 2 mm and operated at a cell potential of 3 V. Thus, resulting in the current density being considerably higher than that used to obtain the experimental data and used in the validation of the model in Chapter 7. The mean bubble size has been reported to increase with increasing current density [Dedigama et al., 2014; Abdelouahed et al., 2014]. Experimental data, confirming the mean bubble size, cannot be obtained with the TDIM applied in this study at these conditions due to bubble clouding in the actual electrochlorination cell. Thus, it is assumed that the mean bubble size is doubled in the following investigations, resulting in a bubble size of 125 µm.

In this chapter investigations of the phenomena occurring in the model geometry, shown in Figure G.2a in Appendix G, will be shown. First, the flow structures occurring in the electrochlorination cell are treated since these greatly influence the transport of species, and likewise influence the electrochemistry.

8.1 Flow structures

Figure 8.1 shows the true liquid velocity magnitude throughout the electrochlorination cell, where an inlet liquid velocity of 6.9 mm/s, corresponding to 2 L/h with a cell depth of 40 mm, is applied at the inlet.

As seen from Figure 8.1 the electrolytic solution is re-entering and recirculating through the right side of the outlet in order to fulfil the continuity equation. This recirculation occurs due to the liquid flow structure being displaced to the left when flowing out of the cell gap. Thus, exiting the electrochlorination cell through the left side of the outlet. Due to the displacement of the liquid flow structure a recirculation zone occurs in the bottom left corner of the top part of the electrochlorination cell. This recirculation occurs all the way to the top of the anode, where some of the electrolytic solution is seen to flow down along the anode. This recirculation zone along the anode results in a high velocity flow in the bulk region through the cell gap as well as close to the cathode.

Figure 8.2 shows the true gas velocity magnitude and gas volume fraction throughout the electrochlorination cell.

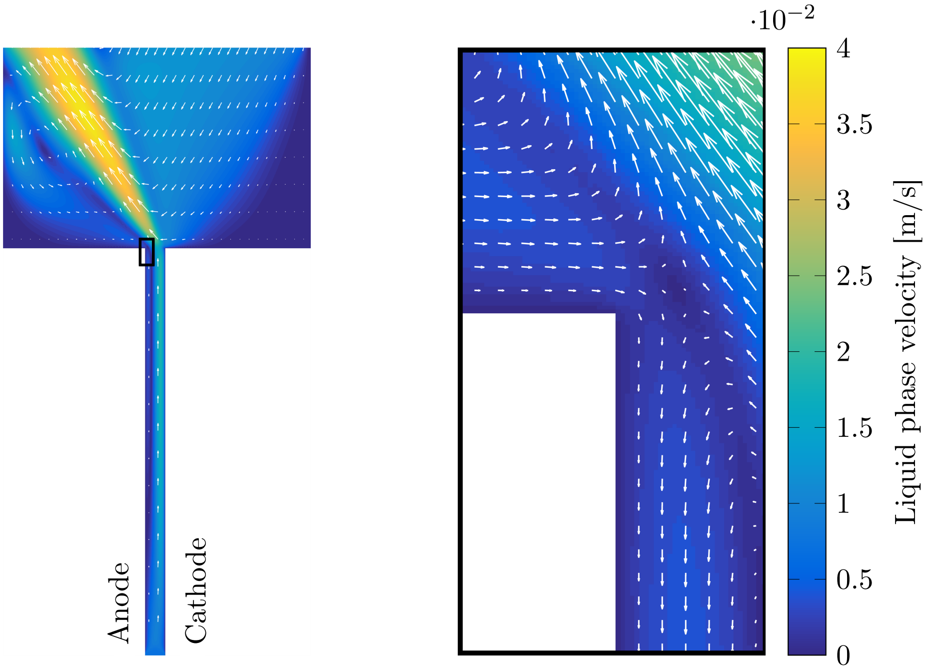

Figure 8.1. Velocity magnitude of liquid phase for an inlet liquid velocity of 6.9 mm/s, corresponding to an inlet liquid flow rate of 2 L/h. The right figure shows a zoom at the top of the anode.

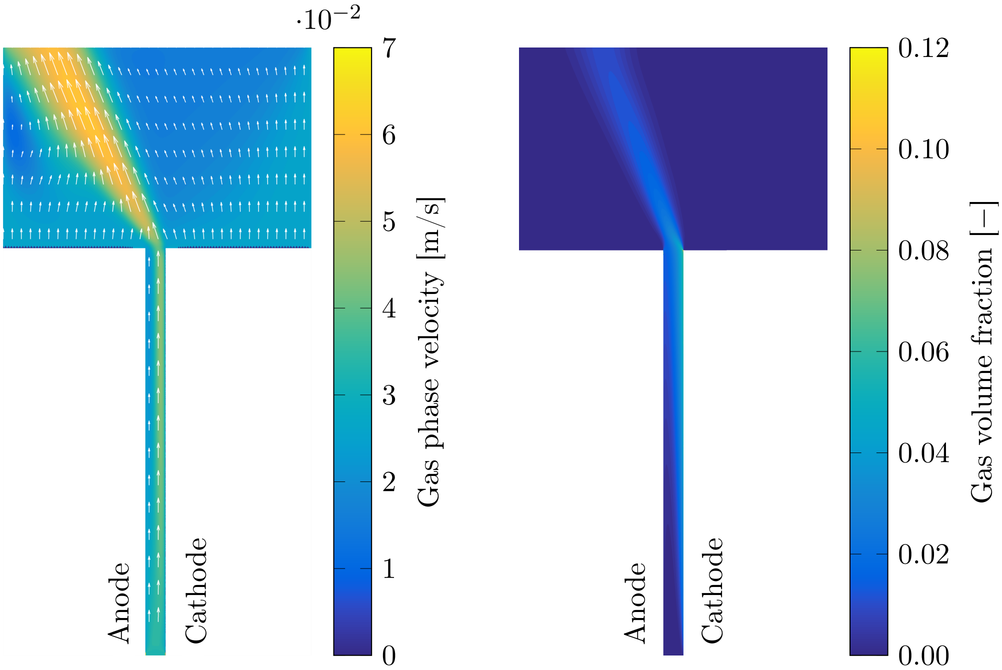

(a) Velocity magnitude. ***(b)*** Volume fraction.

Figure 8.2. Gas velocity magnitude and volume fraction throughout the electrochlorination cell.

As seen from Figure 8.2a the bubbles, like the electrolytic solution, are displaced to the left due to the formulation of the two-phase flow, where the gas velocity is related to the liquid velocity and the slip velocity between the phases. Moreover, it is seen that the bubbles exit the electrochlorination cell at a maximum velocity of about 60 mm/s. Comparing Figures 8.1 and 8.2a the slip velocity between the two phases is found to be approximately 20 mm/s. Furthermore, Figure 8.2b shows that the gas volume fraction and bubble layer increase along the cathode until the top, where a maximum gas volume fraction of approximately 11% occurs. This shows the importance of taking into account the volume occupied by the gas phase as the bubbles significantly hinder the electrochemical reactants access to the electrode surface. Finally, it is seen that almost all bubbles occurring are produced at the cathode.

In the following the distributions of hypochlorite and hypochlorous acid concentration throughout the electrochlorination cell are described.

8.2 Hypochlorite and hypochlorous acid concentrations

Figure 8.3 shows the concentrations of hypochlorite and hypochlorous acid throughout the electrochlorination cell.

As seen from Figure 8.3, a very low concentration of hypochlorite occurs in the modelled electrochlorination cell. However, a considerable concentration of hypochlorous acid occurs, especially in the region very close to the anode.

The reason for this is found in the kinetics data applied for modelling the dissociation of hypochlorous acid. For easy reference, the dissociation of hypochlorous acid, Reaction (C 5.6), is repeated below.

$$\mathrm{HOCl}\underset{\mathrm{k_r}}{\overset{\mathrm{k_f}}{\rightleftharpoons}}\mathrm{H^+} + \mathrm{OCl^-} \tag{C 5.6}$$

As stated in Section 5.2, the dissociation of hypochlorous acid is only taken into account in the anode diffusion layer due to convergence issues when specifying this reaction to occur in the bulk region and top part of the electrochlorination cell. The pH value is expected to be below 6 within the anode diffusion layer, which means that the dissociation of hypochlorous acid is favoured strongly to the left, towards hypochlorous acid [Sawyer et al., 2003; O'Brien et al., 2005]. However, around the neutral point, pH of 7.5, the percentage of hypochlorous acid equals that of hypochlorite and for pH values above 9 the dissociation of hypochlorous acid is strongly favoured to the right meaning that all hypochlorous acid dissociates into hypochlorite [Sawyer et al., 2003; O'Brien et al., 2005]. The concentration of hydroxide, produced through the primary cathodic electrochemical reaction. is expected to considerably exceed the concentration of hydrogen ions produced through the anodic loss reaction. Thus, the pH value in much of the top part of the electrochlorination cell and within the cathode diffusion layer is expected to be 9 or above. This means that much of the unreacted hypochlorous acid coming from the anode diffusion layer is expected to dissociate into hypochlorite, when entering the top part of the electrochlorination cell or if it diffuses into the cathode diffusion layer through the bulk region. Hence, resulting in a considerably higher hypochlorite output than that predicted by the model.

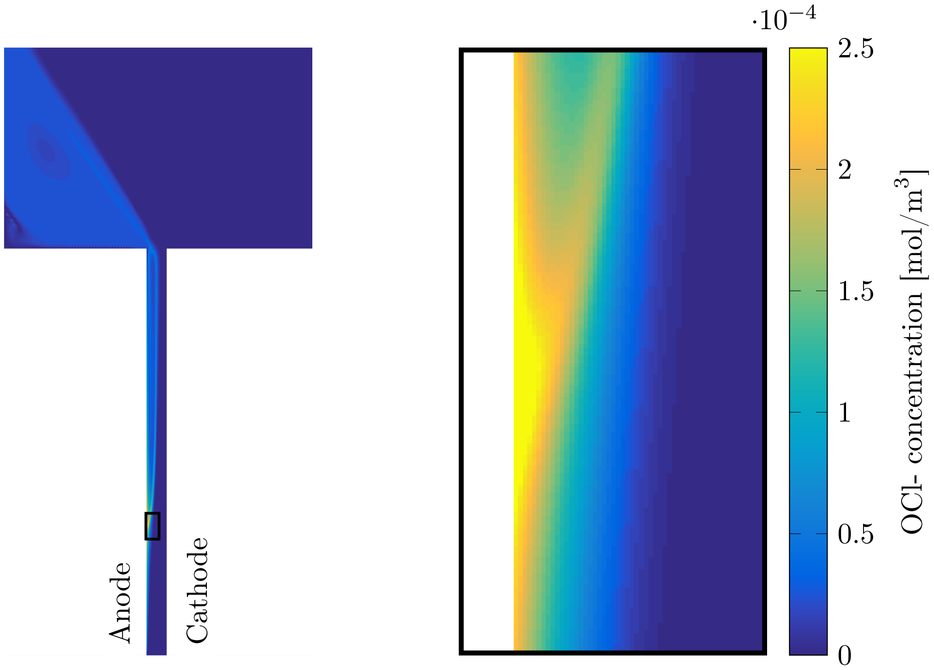

(a) Hypochlorite.

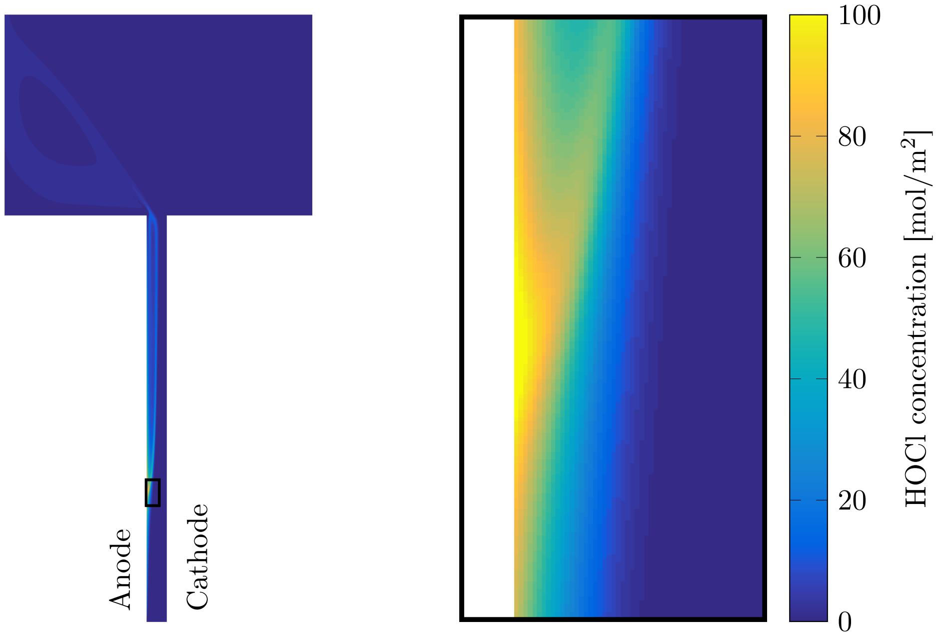

(b) Hypochlorous acid.

Figure 8.3. Hypochlorite and hypochlorous acid concentrations throughout the electrochlorination cell and zooms at high concentration points.

Moreover, Figures 8.3a and 8.3b, show that the highest hypochlorite and hypochlorous acid concentrations occur at approximately a third of the distance from the bottom to the top of the anode. From this point the species are seen to flow into the bulk region and out of the electrochlorination cell. The reason for this high concentration point can be found from the liquid flow structure presented in Figure 8.1, where it was observed that the electrolytic solution recirculates down along the anode. The high concentration point thus constitutes the point where the inertia of the recirculated flow equals that of the flow entering the electrochlorination cell through the inlet, thus creating a stagnation point in the flow.

Figure 8.4 shows the concentrations of hypochlorite and hypochlorous acid at the cathode surface.

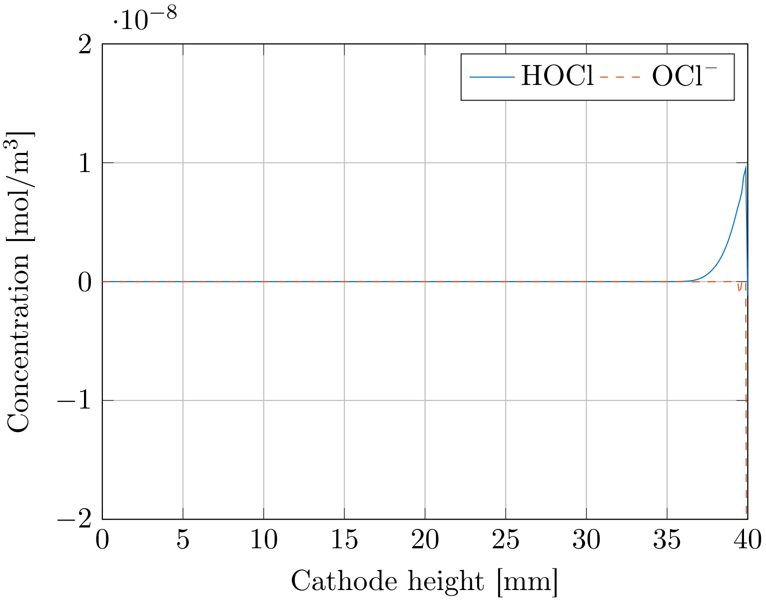

Figure 8.4. Concentrations of hypochlorite and hypochlorous acid at the cathode surface.

As seen from Figure 8.4 the concentrations of hypochlorite and hypochlorous acid are essentially zero at the surface of the cathode. The reason for this is found in Figure 8.1, where it is seen that a high velocity flow occurs in the bulk region and close to the cathode. Thus, the convective transport dominates the transport of hypochlorite and hypochlorous acid. Hence, resulting in basically none of these species diffusing into the cathode diffusion layer and to the cathode surface.

In the following the overpotentials and current densities for the electrochemical reactions are described.

8.3 Overpotentials and current densities

Figure 8.5 show the overpotentials and Figure 8.6 the current densities, for the electrochemical reactions considered in this study, Reactions (C 5.1) to (C 5.4). For easy reference the electrochemical reactions considered in this study are repeated below.

$$2\,\mathrm{Cl^-} \longrightarrow \mathrm{Cl_2} + 2\,\mathrm{e^-} \quad \text{(Primary anode reaction)} \tag{C 5.1}$$

$$2\,\mathrm{H_2O} \longrightarrow \mathrm{O_2} + 4\,\mathrm{H^+} + 4\,\mathrm{e^-} \quad \text{(Secondary anode reaction)} \tag{C 5.2}$$

$$2\,\mathrm{H_2O} + 2\,\mathrm{e^-} \longrightarrow \mathrm{H_2} + 2\,\mathrm{OH^-} \quad \text{(Primary cathode reaction)} \tag{C 5.3}$$

$$\mathrm{OCl^-} + \mathrm{H_2O} + 2\,\mathrm{e^-} \longrightarrow \mathrm{Cl^-} + 2\,\mathrm{OH^-} \quad \text{(Secondary cathode reaction)} \tag{C 5.4}$$

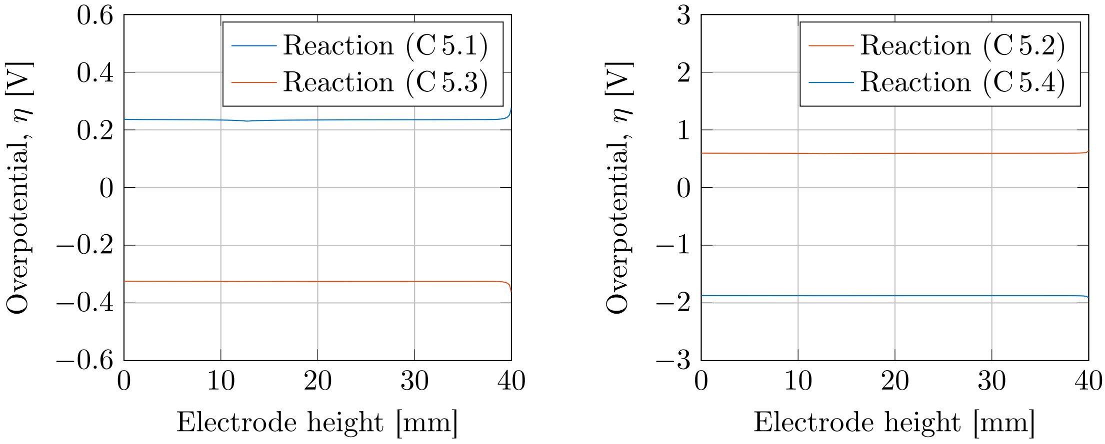

(a) Primary reactions. *(b)* Secondary reactions.

Figure 8.5. Overpotentials along the electrodes for the primary and secondary electrochemical reactions.

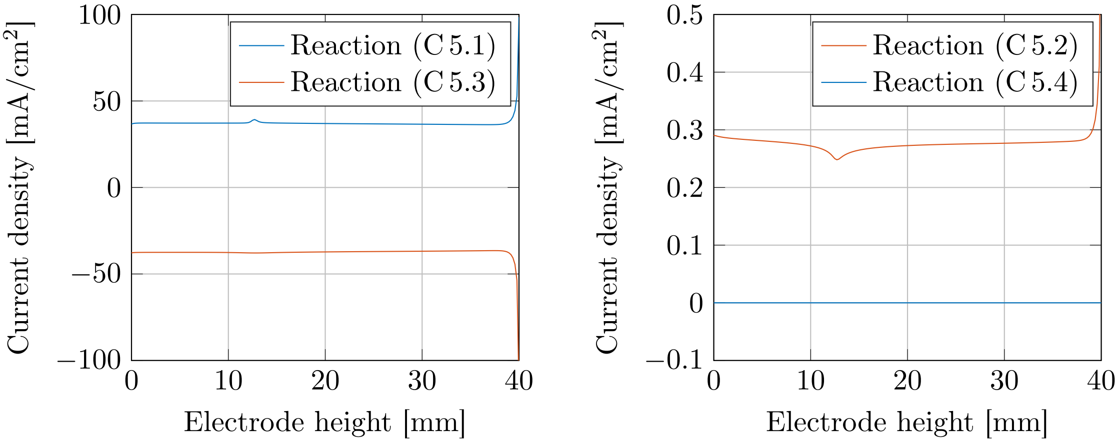

(a) Primary reactions. *(b)* Secondary reactions.

Figure 8.6. Current densities for the primary and secondary electrochemical reactions.

As seen from Figures 8.5a and 8.5b the overpotentials remain almost constant along the main part of the anode and cathode. The equilibrium potentials have been implemented as constant values due to the inability of implementing the dissociation of water reaction, as described in Section 5.2.1, which makes the evaluation of meaningful pH values possible.

As the electrode potentials at the anode and cathode are constant values as well, this means that the potentials at the electrode-electrolytic solution interfaces are almost constant along the anode and cathode. This behaviour can be seen from Equation (5.10) and Figure 8.7.

$$\eta_m = \Phi_s - \Phi_l - E_{eq,m} \tag{5.10}$$

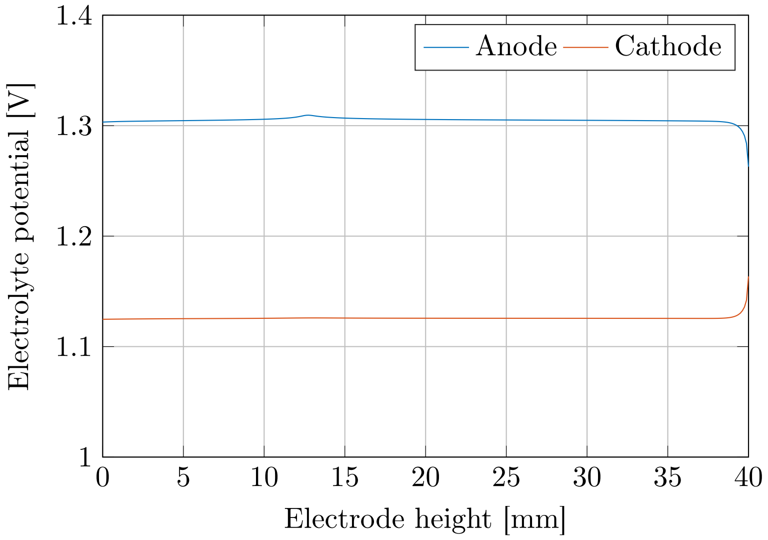

Figure 8.7. Potentials at the interfaces between electrodes and electrolytic solution.

The overpotentials predicted by the model are seen to slightly increase and decrease at the top of the anode and cathode, respectively, as a result of edge effects. If the dissociation of water reaction could have been implemented the equilibrium potentials could have been made pH dependent. The pH value is expected to vary along the electrodes due the flow occurring in the electrochlorination cell, as shown in Figure 8.1. This would in turn make the overpotentials vary as well, thus resulting in varying current densities along the electrodes in accordance with the Butler-Volmer equation.

Moreover, Figures 8.6a and 8.6b, show that the dominant electrochemical reactions are those evolving chlorine and hydrogen, i.e. the primary anode and cathode electrochemical reactions, Reactions (C 5.1) and (C 5.3), respectively. Both are seen to result in a current density of approximately 37 mA/cm^2. At the same time it is seen that the anode and cathode loss reactions essentially are not occurring. The anode loss reaction, Reaction (C 5.2), results in a current density of about 0.275 mA/cm^2, whereas the current density for the cathode loss reaction, Reaction (C 5.4), though hard to see, is at the order of 10^{-5} mA/cm^2. The reason for this low current density, for the cathodic loss reaction, is found in Figure 8.4, where a very low hypochlorite concentration is seen at the cathode surface. Due to the concentration dependency of Reaction (C 5.4), this reaction essentially does not occur. From this it is seen that less than 1% of the current density at the anode goes to the loss reaction, whereas even less goes to the loss reaction at the cathode. This means that the overall current efficiency of the electrochlorination cell essentially is 1, which can be seen from Equation (8.1).

$$\beta_{overall} = 1 - \cancelto{\approx 0}{\frac{i_{loc,\mathrm{O_2}}}{i_{loc,\mathrm{Cl_2}} + i_{loc,\mathrm{O_2}}}} - \cancelto{\approx 0}{\frac{i_{loc,\mathrm{OCl^-}}}{i_{loc,\mathrm{H_2}} + i_{loc,\mathrm{OCl^-}}}} \tag{8.1}$$

The large difference in current density between the oxygen and hydrogen evolving electrochemical reactions, Reactions (C 5.2) and (C 5.3), respectively, explains the much higher gas volume fraction occurring at the cathode compared to that at the anode, as shown in Figure 8.2b. Moreover, it confirms the expectation that the production of hydroxide is considerably higher than the production of hydrogen ion. Thus, supporting the possibility of the pH value being at or above 9 in much of the top part of the electrochlorination cell and within the cathode diffusion layer.

Furthermore, Figures 8.6a and 8.6b show that considerable increases in current densities occur at the top edge of the anode and cathode. The reason for these significant increases is found in the overpotentials predicted by the model at the edges. Figure 8.5 shows that a slight increase and decrease in overpotentials occur at the anode and cathode edges, respectively. When evaluating these in the Butler-Volmer equation a significant increase occur in the corresponding current density for the given electrochemical reaction.

At an anode height of about 13 mm, Figure 8.6a, an increase is seen in the current density for the chlorine evolving electrochemical reaction, Reaction (C 5.1), corresponding to the high concentration points seen in Figure 8.3. Figure 8.8 shows the concentration of chloride ions along the anode for 8 different time steps.

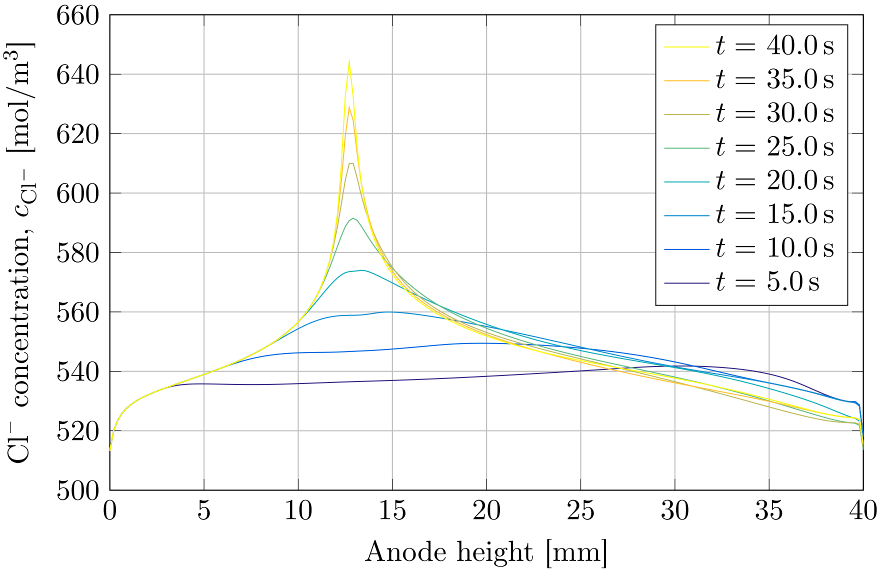

Figure 8.8. Concentration of chloride ions along the anode height for 8 different time steps.

As seen from Figure 8.8 chloride ions accumulate over time at the anode surface until a simulation time of 40 s at which point the concentration of chloride ions has reached a sufficient steady value. This accumulation means that the current density for the chlorine evolving electrochemical reaction must increase due to the concentration dependency of this reaction, as shown in Figure 8.9.

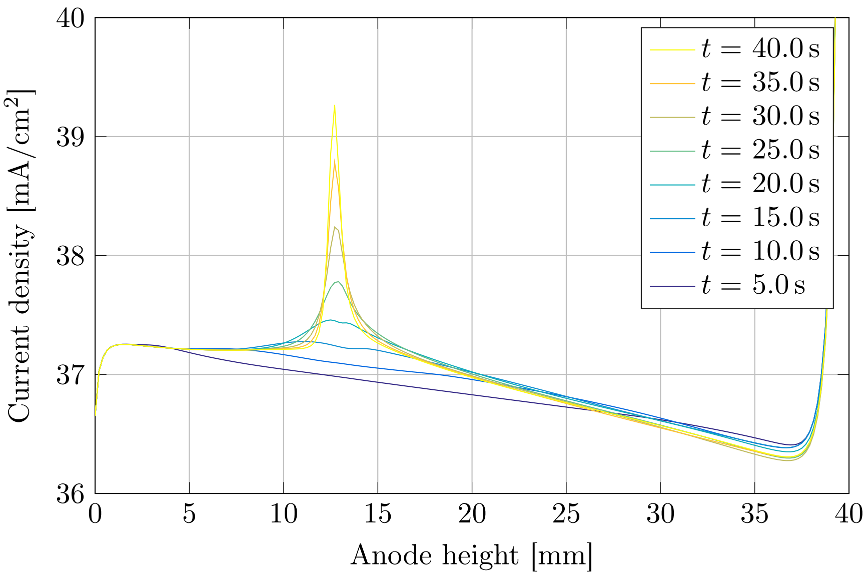

Figure 8.9. Current density for chlorine evolving electrochemical reaction along the anode height for 8 different time steps.

The accumulation of chloride ions at the anode surface ensures that very little of the current density at the anode goes to the loss reaction as the surface concentration exceeds the concentration in the bulk flow. This is confirmed by comparing the current densities for the chlorine and oxygen evolving electrochemical reactions, shown in Figures 8.6a and 8.6b, respectively. As observed in Section 7.4 an inlet chloride concentration of 100 mol/m^3, for the large cell gap geometry, results in the consumption of chloride ions at the anode surface being higher than that transported to the surface. Furthermore, it was seen that the chloride ion concentration decreased along the anode. Thus, a chloride ion concentration lower than the concentration in the bulk flow occurred at the surface of the anode. This results in less of the anode current density going to the production of chlorine and more to the loss reaction producing oxygen bubbles, hence lowering the overall current efficiency of the electrochlorination cell. For the oxygen evolving electrochemical loss reaction, Reaction (C 5.2), it is seen that an increase in current density for the chlorine evolving reaction at 13 mm, leads to a decrease in current density for this reaction, and thus impedes the loss reaction.

In the following the migrational and diffusional fluxes of chloride ions towards the anode are treated.

8.4 Migration and diffusion of chloride ions

The accumulation of chloride ions at the anode surface occurs due to the mass flux of chloride ions being consumed, at the given current density for the chlorine evolving electrochemical reaction, being less than the mass flux towards the anode surface by a combined effect of migration, diffusion and convection. As chloride ions are accumulating at the anode surface, the concentration of chloride ions is higher than that in the bulk region, hence, chloride ions are diffusing towards the bulk region.

Figure 8.10 shows the migrational and diffusional fluxes of chloride ions at the boundary of the anode diffusion layer, 200 µm from the anode surface.

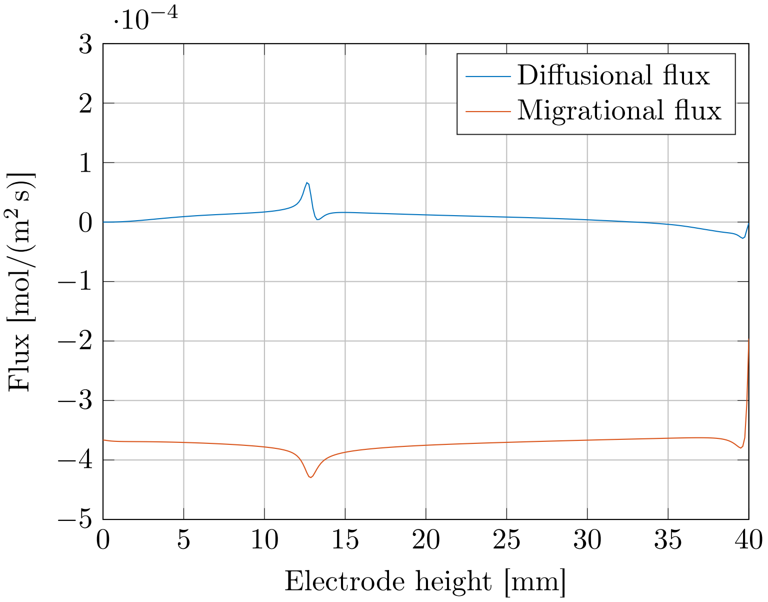

Figure 8.10. Migrational and diffusional fluxes of chloride ions at the boundary of the anode diffusion layer.

As seen from Figure 8.10 the migrational flux of chloride ions towards the anode surface considerably exceeds the diffusional flux away from the anode. Furthermore, it is seen that chloride ions are diffusing towards the anode at the top of the anode diffusion layer. The reason for this is found in the liquid flow structure. As shown in Figure 8.1, the electrolytic solution is recirculating down along the anode and as shown in Figure 8.8, a high concentration point is occurring from which a high concentration of chloride ions is flowing into the bulk. When reaching the top of the anode diffusion layer, the concentration in this high concentration flow exceeds the concentration of chloride ions within the diffusion layer, thus chloride ions are diffusing from the high concentration flow at the boundary of the anode diffusion layer into the anode diffusion layer.

Ninth Chapter

Conclusion

A study has been carried out concerning the numerical and experimental investigations of an undivided electrochlorination cell for generation of hypochlorite. A 2D model including the four main phenomena occurring during operation has been the purpose of this study. The four main phenomena are: electrochemistry, chemical reactions, species transport and two-phase, gas-liquid flow. The existing models presented in the literature have proven to be insufficient to incorporate one or more of the phenomena taking place in such cells. Their main deficiencies consisted in the lack of a two-phase flow, and thus the inability of predicting the effect of the generated gas bubbles on the current and concentration distributions. The study was done according to the problem statement formulated in Chapter 3.

In order to obtain reliable measurements of required model inputs and parameters for model validation a Telecentric Direct Image Method (TDIM) with two camera and telecentric lens configurations was applied. Each configuration constituted an experimental task. Task (A) was the determination of the mean bubble size and gas volume fraction, while Task (B) constituted the determination of y-component of the bubble velocities. The applied TDIM made it possible to acquire shadow images of the generated gas bubbles, thus giving the possibility of measuring size and hence gas volume fractions, as well as velocity of the bubbles after processing these images in MATLAB and LabVIEW. The method was verified by measuring polyamid particles with a known mean size of 50 µm, where the camera and telecentric lens configurations for Task (A) and (B) measured a mean size of 49.7 µm with a confidence interval of ± 0.9 µm and 47.8 µm with a confidence interval of ±0.7 µm, respectively. The method proved to be reliable for low gas volume fractions as it has not been possible to find a method of dividing overlapping bubbles without breaking the edges of these and other bubble contours. Thus, the experiments were conducted at reasonable low current densities in order to avoid too many overlapping bubbles, which would alter the gas volume fraction measurements used for model validation.

The electrochlorination cell was modelled in COMSOL Multiphysics in a two-dimensional framework and employed four preprogrammed modules, each modelling one of the identified phenomena occurring during operation:

- Electrochemistry → Secondary Current Distribution (SCD)
- Chemical reactions → Chemistry (CHEM)
- Transport of species → Transport of Dilute Species (TDS)
- Two-phase flow → Bubbly Flow (BF)

The couplings between modelling aspects were achieved by calling variables across the modules. Thus, ensuring that the generated gas bubbles influence the electrochemical aspects and transport of species by occupying some volume next to the electrodes and in the bulk flow, as well as ensuring that the electrochemical reactions do not occur without the reactants being present at the electrode surfaces.

The modelling of the electrochlorination cell was validated by comparing the measured and predicted polarisation curves, as well as the bubble flow structures and velocity magnitudes visualised and measured by a flow visualisation technique. Furthermore, mean y-components of the bubble velocities and gas volume fractions measured by the TDIM at four different positions inside the cell during operation were compared to those predicted by the model at the same positions. The comparisons showed reasonable consistency in terms of polarisation curves, bubble flow structures, velocity magnitudes and mean bubble velocity y-component. However, the predicted and measured gas volume fractions at the four different positions deviated significantly from each other. It was argued that possible reasons could be found in the issues with overlapping bubbles for the TDIM and in the nature of the cathode, causing bubbles to stick to the surface, which would not necessarily be captured when detached. Estimations of the gas volume fraction at the exit of the cell gap were obtained using the flow visualisation technique and showed to be in agreement with the predictions given by the model, and thus supporting the postulated reasons.

With the model validated, investigations were conducted with a small cell gap of 2 mm and a cell voltage of 3 V in order to resemble industrial applications. These investigations showed the importance of accounting for the two-phase flow occurring. It was seen that the generated gas bubbles had a great influence on the flow of the liquid solution, which in turn highly influenced the electrochemical aspects and concentration distributions throughout the electrochlorination cell. The overall current efficiency of the cell was found to be very close to 1, due to a high concentration of chloride ions at the anode surface and very little hypochlorite and hypochlorous acid diffusing to the cathode surface.

TENTH CHAPTER

Future work

This chapter serves to describe the future work which can be done, following the work performed in this study.

Concentration dependent electrochemistry

As stated in Section 5.1, it has been assumed that a current density only occurs in the electrolytic solution due to a potential gradient and charged species. As shown from Figure 7.1 in Chapter 7, the polarisation curve predicted by the fitted model fits reasonable with the measured curve. However, the slope of the polarisation curve predicted by the model is less steep than that measured, thus indicating that a considerable deviation can be expected at higher cell voltages. In order to try and adjust this, investigations could be carried out by making the current density through the electrolytic solution dependent on the concentration of charged species across the cell gap. However, as also stated by COMSOL [2015a] this will make the problem even more non-linear and could therefore lead to convergence issues.

Implementation of further chemical reactions

As stated in Section 5.2, the dissociation of water is not considered due to convergence issues when trying to take this reaction into account. Implementing this reaction will enable the possibility of evaluating the pH value throughout the electrochlorination cell. This would, in turn, give the possibility of making the reaction kinetics for the considered bulk reactions as well as the equilibrium potentials pH dependent. Successfully implementing this, would make the model more dynamic and applicable if model inputs affecting the pH value are changed, such as concentration inputs.

In Section 5.2 it was stated that the dissociation of hypochlorous acid is only considered in the anode diffusion layer due to convergence issues when specifying this reaction to be occurring anywhere else in the electrochlorination cell. In Chapter 8 it was seen that a very small amount of hypochlorite is being produced in the anode diffusion layer with the implemented kinetics. As argued, the hypochlorite output is expected to be significantly higher due to the expected pH values in much of the top part of the electrochlorination cell being above the neutral point of 7, hence favouring the dissociation of hypochlorous acid towards the desired hypochlorite. Thus, further implementation of this reaction, either based on assumptions of the pH value or pH dependency, would give an indication of the approximate hypochlorite output.

Supersaturation of chlorine

As stated in Section 5.3, chlorine is assumed to go to the liquid phase, whereas hydrogen and oxygen go to the gaseous phase due to their very small solubilities in water. However, for small cell gaps and at significant cell voltages the production of chlorine could result in the local concentration of chlorine exceeding its solubility in water and thus, supersaturation would drive the formation of chlorine bubbles. In Chapter 8 the importance of accounting for the generated bubbles was shown and thus, it is expected that the model could benefit from taking this aspect into account.

Experimental validation for small cell gap

The modelling done in this study has only been validated for a large cell gap, after which it was assumed that the modelling approach was suitable for small cell gaps as well. In order to confirm this, the modelling approach should be compared to experimental data obtained for a small cell gap as well. In this study comparisons have only been made between polarisation curves and hydrodynamic aspects. Further validation could constitute comparisons of parameters such as concentrations of species like chlorine or chloride ions. Implementing the dissociation of water and hypochlorous acid in the model would furthermore make comparisons of pH values and concentrations of hypochlorite and hypochlorous acid at the outlet possible.

Measurement methodologies

In order to obtain experimental data at small cell gaps, considerations have to be put into the applied measuring method, since the amount of generated bubbles is very significant at such cell gaps. As stated in Appendix B.3, the TDIM applied in this study is subject to significant limitations regarding the amount of generated bubbles, as it has not been possible to find a consistent method for distinguishing between overlapping bubbles, as explained in Section 4.4.2. As stated in Section 2.3, such a measuring method should ideally not involve a probe due to the possibility of significantly influencing the fluid dynamics and, hence the chemical characteristics of the electrochlorination cell.

Bibliography

Abdelouahed, Hreiz, Poncin, Valentin, and Lapicque, 2014. L. Abdelouahed, R. Hreiz, S. Poncin, G. Valentin, and F. Lapicque. *Hydrodynamics of gas bubbles in the gap of lantern blade electrodes without forced flow of electrolyte: Experiments and CFD modelling.* Chemical Engineering Science, 111, 255–265, 2014.

A.J. Bard and L.R. Faulkner, 2002. A.J. Bard and L.R. Faulkner. *Electrochemical Methods: Fundamentals and Applications.* 2^{nd} edition. John Wiley & Sons, Inc., 2002. ISBN 0-471-04372-9.

Aldas, Pehlivanoglu, and Mat, 2008. Kemal Aldas, Nur Pehlivanoglu, and Muhmat D. Mat. *Numerical and experimental investigation of two-phase flow in an electrochemical cell.* International Journal of Hydrogen Technology, 33, 3668–3675, 2008.

Arikawa, Murakami, and Takasu, 1998. T. Arikawa, Y. Murakami, and Y. Takasu. *Simultaneous determination of chlorine and oxygen evolving at* RuO_2/Ti *and* RuO_2-TiO_2/Ti *anodes by differential electrochemical mass spectroscopy.* Journal of Applied Electrochemistry, 28, 511–516, 1998.

Basler, 2016a. Basler. *acA1300-30um specifications.* URL: `http://www.baslerweb.com/en/products/cameras/area-scan-cameras/ace/aca1300-30um`, 2016. Accessed on: 07.03.2016.

Basler, 2016b. Basler. *acA1920-155um specifications.* URL: `http://www.baslerweb.com/en/products/cameras/area-scan-cameras/ace/aca1920-155um`, 2016. Accessed on: 07.03.2016.

Bengzon, 2009. Fredrik Bengzon. *Adaptive Finite Element Methods for Multiphysics Problems.* Doctoral Thesis. Umeå University, 2009.

Black and Veatch Corporation, 2010. Black and Veatch Corporation. *White's handbook of chlorination and alternative disinfectants.* 5^{th} edition. Wiley, 2010. ISBN 978-0-470-18098-3.

Boissonneau and Byrne, 2000. P. Boissonneau and P. Byrne. *An experimental investigation of bubble-induced free convection in a small electrochemical cell.* Journal of Applied Electrochemistry, 30, 767–775, 2000.

Bouguet, 1999. Jean-Yves Bouguet. *Pyramid Implementation of the Lucas Kanade Feature Tracker - Description of the algorithm.* Intel Corporation, Microprocessor Research Labs, 1999.

Boyer, Duquenne, and Wild, 2002. C. Boyer, A. Duquenne, and G. Wild. *Measuring techniques in gas-liquid and gas-liquid-solid reactor.* Chemical Engineering Science, 57, 3185–3215, 2002.

Busciglio, Grisafi, Scargiali, and Brucato, 2013. A. Busciglio, F. Grisafi, F. Scargiali, and A. Brucato. *On the measurement of local gas hold-up, interfacial area and bubble size distribution in gas-liquid contactors via light sheet and image analysis: Imaging technique and experimental results.* Chemical Engineering Science, 102, 551–566, 2013.

Byrne, Fontes, Parhammar, and Lindbergh, 2001. P. Byrne, E. Fontes, O. Parhammar, and G. Lindbergh. *A Simulation of the Tertiary Current Density Distribution from a Chlorate Cell.* Journal of Electrochemical Society, 148, 125–132, 2001.

Celata, D'Annibale, Marco, Memoli, and Tomiyama, 2006. G. P. Celata, F. D'Annibale, P. Di Marco, G. Memoli, and A. Tomiyama. *Measurements of rising velocity of a small bubble in a stagnant fluid in one- and two-component systems.* Experimental Thermal and Fluid Science, 31 No. 6, 609–623, 2006.

Chaira and Ray, 2010. Tamalika Chaira and Ajoy Kumar Ray. *Fuzzy Image Processing and Applications with MATLAB.* CRC Press, 2010. ISBN 978-1-4398-0708-8.

Christensen and Thomassen, 2014. Mads Smed Christensen and Peter Hedegaard Thomassen. *Experimental Determination of Bubble Size Distribution in a Water Column by Interferometric Particle Imaging and Telecentric Direct Image Method.* Master Thesis. Aalborg University, 2014.

COMSOL, 2015a. COMSOL. *Electrochemistry Module - User's Guide*, 2015. Version: COMSOL 5.1.

COMSOL, 2015b. COMSOL. *Reference Manual*, 2015. Version: COMSOL 5.1.

Couper, Pletcher, and Walshs, 1990. A. Mottram Couper, Derek Pletcher, and Frank C. Walshs. *Electrode Materials for Electrosynthesis.* Chemical Reviews, 90, 837–865, 1990.

Crowe, Sommerfeld, and Tsuji, 1998. C. Crowe, M. Sommerfeld, and Y. Tsuji. *Multiphase Flows with Droplets and Particles.* CRC Press, 1998. ISBN 0-8493-9469-4.

Crowe, 2006. Clayton T. Crowe. *Multiphase Flow Handbook.* Taylor & Francis Group, LLC, 2006. ISBN 978-0-8493-1280-9.

C.Y. Cheng, 2007. G.H. Kelsall C.Y. Cheng. *Models of Hypochlorite production in electrochemical reactors with plate and porous anodes.* Journal of Applied Electrochemistry, 37, 1203 – 1217, 2007.

Dahlkild, 2001. Anders A. Dahlkild. *Modelling the two-phase flow and current distribution along a vertical gas-evolving electrode.* J. Fluid Mech., 428, 249–272, 2001.

Dantec Dynamics A/S, 2015. Dantec Dynamics A/S. *DynamicStudio - User's Guide*, 2015. Version: DynamicStudio2015a.

Dedigama, Angeli, K. Ayers, Shearing, and D. Tsaoulidis, 2014. I. Dedigama, P. Angeli, J. B. Robinson K. Ayers, P. R. Shearing, and G. J. L. Brett D. Tsaoulidis. *In situ diagnostic techniques for characterisation of polymer electrolyte membrane water electrolysers - Flow visualisation and electrochemical impedance spectroscopy.* International Journal of Hydrogen Energy, 39, 4468–4482, 2014.

Devadhasan, Yoo, and Kim, 2015. Jasmine Pramila Devadhasan, In Sang Yoo, and Sanghyo Kim. *Overview of CMOS image sensor use in molecular diagnostics.* Current Applied Physics, 15, 402–411, 2015.

Dijkhuizen, Sint Annaland, and Kuipers, 2010. W. Dijkhuizen, M. van Sint Annaland, and J.A.M. Kuipers. *Numerical and experimental investigation of the lift force on single bubbles.* Chemical Engineering Science, 65, 1274–1287, 2010.

Edmund Optics, 2016a. Edmund Optics. *Depth of Field and Depth of Focus.* URL:`http://www.edmundoptics.eu/resources/application-notes/imaging/depth-of-field-and-depth-of-focus/`, 2016. Accessed on: 16.05.2016.

Edmund Optics, 2015a. Edmund Optics. *0.5X, 110mm WD Compact Telecentric Lens.* URL: `http://www.edmundoptics.com/imaging-lenses/telecentric-lenses/compact-telecentric-lenses/63729/`, 2015. Accessed on: 10.12.2015.

Edmund Optics, 2016b. Edmund Optics. *Optics and Optical Instruments Annual Catalog.* 2016 Master Source Book, 2016.

Edmund Optics, 2015b. Edmund Optics. *The Advantages of Telecentricity.* URL: `http://www.edmundoptics.eu/technical-resources-center/imaging/advantages-of-telecentricity/`, 2015. Accessed on: 10.12.2015.

Gaur, Singh, and Rao, 1994. B. Gaur, A. K. Singh, and N. J. Rao. *Corrosion of mild steel in hypochlorite solution - An electrochemical and weight-loss study.* Indian Journal of Chemical Technology, 1, 225–229, 1994.

Gijsberg and Janssen, 1989. H. Gijsberg and L. Janssen. *Distribution of mass transfer over a 0.5-m-tall hydrogen-evolving electrode.* Journal of Applied Electrochemistry, 19, 637–648, 1989.

Grundfos. Grundfos. *Selcoperm 125 - 2000.* URL: `http://www.grundfos.com/products/find-product/ses-195-selcoperm.html`. Accessed on: 08.12.2015.

Guldelli, Compton, Feliu, Gileadi, Lipkowski, Schmickler, and Trasatti, 2014. Rolando Guldelli, Richard G. Compton, Juan M. Feliu, Eliezer Gileadi, Jacek Lipkowski, Wolfgang Schmickler, and Sergio Trasatti. *Defining the transfer coefficient in electrochemistry: An assessment (IUPAC Technical Report).* Pure and Applied Chemistry, 86, 245–258, 2014.

Hornberg, 2006. Alexander Hornberg. *Handbook of Machine Vision.* Wiley - VCH, 2006. ISBN 978-3-527-40584-8.

Ibl and Landolt, 1968. *N. Ibl and D. Landolt.* Electrochemical Society, 115, 1968.

Ibl and Vogt, 1983. *N. Ibl and H. Vogt.* Comprehensive treatise of electrochemistry, 2. Plenum, 1983.

Ipek, Vynnycky, and Cornell, 2006. N. Ipek, M. Vynnycky, and A. Cornell. *A Mathematical Model for the Electrochemical Pickling of Steel.* Journal of Electrochemical Society, 154, 108–119, 2006.

Ipek, Vynnycky, and Cornell, 2008. N. Ipek, M. Vynnycky, and A. Cornell. *A Coupled Electrochemical and Hydrodynamical Two-Phase Model for the Electrolytic Pickling of Steel.* Journal of Electrochemical Society, 155, 33–43, 2008.

J. Choi, S. Shim, 2013. J. Yoon J. Choi, S. Shim. *Design and operating parameters affecting an electrochlorination system.* Journal of Industrial and Engineering Chemistry, 19, 215 – 219, 2013.

Jianu, Rosen, Naterer, and Wang, 2015. O.A. Jianu, M.A. Rosen, G.F. Naterer, and Z. Wang. *Two-phase bubble flow and convective mass transfer in water splitting processes.* International Journal of Hydrogen Energy, 40, 4047–4055, 2015.

Khelifa, Moulay, Hannane, Benslimene, and Hecini, 2004. A. Khelifa, S. Moulay, F. Hannane, S. Benslimene, and M. Hecini. *Application of an experimental design method to study the performance of electrochloriantion cells.* Desalination, 160, 91–98, 2004.

Kuzmin and Turek, 2000. D. Kuzmin and S. Turek. *Efficient numerical techniques for flow simulation in bubble column reactors.* Institute of Applied Mathematics, University of Dortmund, 2000.

Kuzmin, Turek, and Haario, 2005. D. Kuzmin, S. Turek, and H. Haario. *Finite Element Simulation of Turbulent Bubbly Flows in Gas-liquid Reactors.* Ergebnisberichte Angew, Math, 298, University of Dortmund, 2005.

Legendre and Magnaudet, 1998. D. Legendre and J. Magnaudet. *A note on the lift force on a spherical bubble in a viscous linear shear flow.* J. Fluid Mech., 368, 81–126, 1998.

Li and Nathan, 2005. Flora M. Li and Arokia Nathan. *CCD Image Sensors in Deep-Ultraviolet. Degradation Behavior and Damage Mechanisms.* Springer, 2005. ISBN 978-3-540-22680-2.

Menon and Landau, 1987. Murali M. Menon and Uziel Landau. *Modeling of Electrochemical Cells Including Diffusion, Migration, and Unsteady-State Effects.* J. Electrochem. Soc., 134, 2248–2253, 1987.

Nagai, Takeuchi, and Nakao, 2003. N. Nagai, M. Takeuchi, and M. Nakao. *Effects of Generated Bubbles Between Electrodes on Efficiency of Alkaline Water Electrolysis.* JSME International Journal, 46, 549–556, 2003.

National Instruments, **2016**. National Instruments. *NI USB-6215.* URL: `http://sine.ni.com/nips/cds/view/p/lang/da/nid/203483`, 2016. Accessed on: 05.04.2016.

National Instruments, **2015a**. National Instruments. *Connectivity.* NI Vision Concepts Help, 2015.

National Instruments, **2015b**. National Instruments. *Edge Detection.* NI Vision Concepts Help, 2015.

National Instruments, **2015c**. National Instruments. *Image processing.* NI Vision Concepts Help, 2015.

National Instruments, **2015d**. National Instruments. *Particle Measurements.* NI Vision Concepts Help, 2015.

National Physical Laboratory, **2015**. National Physical Laboratory. *Tables of Physical & Chemical Constants.* URL: `http://www.kayelaby.npl.co.uk/general_physics/2_7/2_7_9.html`, 2015. Acquired: 07-12-2015.

Newman, **1991**. John S. Newman. *Electrochemical Systems.* 2$^{\text{nd}}$ edition. Prentice-Hall, Inc., 1991. ISBN 0-13-248758-6.

O'Brien, Bommaraju, and Hine, **2005**. Thomas F. O'Brien, Tilak V. Bommaraju, and Fumio Hine. *Handbook of Chlor-Alkali Technology.* Springer, 2005. ISBN 0-306-48618-0.

Omega, **2016**. Omega. *Low Flow Sensor for Air and Water - FLR1000.* URL: `http://www.omega.com/pptst/FLR1000.html`, 2016. Accessed on: 11.04.2016.

Petrozzo and Singer, **2001**. Ronald A. Petrozzo and Stuart W. Singer. *Telecentric Lenses - simplify noncontact metrology.* URL: `https://www.schneideroptics.com/pdfs/industrial/telecentric_lenses.pdf`, 2001. Accessed on: 21.04.2016.

Péra, Hissel, Gualous, and Turpin, **2013**. Marie-Cécile Péra, Daniel Hissel, Hamid Gualous, and Christophe Turpin. *Electrochemical Components.* ISTE Ltd and John Wiley & Sons, Inc., 2013. ISBN 978-1-84821-401-9.

Sawyer, McCarty, and Parkin, **2003**. Clair N. Sawyer, Perry L. McCarty, and Gene F. Parkin. *Chemistry for Environmental Engineering and Science.* McGraw-Hill Higher Education, 2003. ISBN 0-07-248066-1.

Selman and Newman, **1971**. Jan Robert Selman and John Newman. *Free-Convection Mass Transfer with a Supporting Electrolyte.* J. Electrochem. Soc., 118, 1070–1078, 1971.

Sokolichin, Eigenberger, and Lapin, **2004**. A. Sokolichin, G. Eigenberger, and A. Lapin. *Simulation of buoyancy driven bubbly flow: Established simplifications and open questions.* A.I.Ch.E., 50 No. 1, 24–45, 2004.

Spalding, 1962. C. W. Spalding. *Reaction Kinetics in the Absorption of Chlorine into Aqueous Media*. A.I.Ch.E., 8 No. 5, 685–689, 1962.

Spasojevic, Krstajic, Spasojevic, and Ribic-Zelenovic, 2015. M. Spasojevic, N. Krstajic, P. Spasojevic, and L. Ribic-Zelenovic. *Modelling current efficiency in an electrochemical hypochlorite reactor*. Chemical Engineering Research and Design, 93, 591–601, 2015.

Thomas Condra and Erik Lund, 2016. Thomas Condra and Erik Lund. *Chapter 13. The Finite Element Method - 1D diffusion problems*. Finite Element Method Course at Aalborg University, 2016.

Wallgren, Bark, and Andersson, 1996. C. Fredrik Wallgren, Fritz H. Bark, and Bengt-Joel Andersson. *Electrolysis of a binary electrolyte in two-dimensional channel flow*. Electrochimica Acta, 41, 2909–2916, 1996.

Walpole, Myers, Myers, and Ye, 2011. Ronald E. Walpole, Raymond H. Myers, Sharon L. Myers, and Keying Ye. *Probability & Statistics for Engineers & Scientists*. 9th edition. Prentice Hall, 2011. ISBN 978-0-321-62911-1.

Wang and Margerum, 1993. Tian Xiang Wang and Dale W. Margerum. *Kinetics of Reversible Chlorine Hydrolysis: Temperature Dependence and General-Acid/Base-Assisted Mechanism*. Inorganic Chemistry, 33, 1050–1055, 1993.

Wired Chemist, 2016. Wired Chemist. *Solubilities of Gases in Water at 293 K*. URL: `http://www.wiredchemist.com/chemistry/data/solubilities-gases`, 2016. Accessed on: 10.04.2016.

Wolfson, 2012. Richard Wolfson. *Essential University Physics - Volume 2*. Second Edition, International Edition. Pearson, 2012. ISBN 978-1-4398-0708-8.

Wu, 1987. Jiann-Kuo Wu. *Kinetics of the Reduction of Hypochlorite Ion*. Journal of the Electrochemical Society, 134(6), 1462–1467, 1987.

Zienkiewicz, Taylor, and Nithiarasu, 2005. O.C. Zienkiewicz, R.L. Taylor, and P. Nithiarasu. *The Finite Element Method for Fluid Dynamics*. Sixth Edition. Elsevier, 2005. ISBN 0-7506-6322-7.

Zimmerman, 2006. William B.J. Zimmerman. *Multiphysics Modelling with Finite Element Methods*. World Science Publishing, 2006. ISBN 13 978-981-256-843-4.

Appendix A

The Conference Paper

Some facts have to be noted in terms of the article hereby presented.

The experimental setup is mirrored, compared to the setup shown in the report, in Chapter 4, thus the anode is on the right-hand side and the cathode on the left-hand side.

Errors found after the submission of the article are listed below:

- The cell gap has a width of 7.68 mm, as stated in this report, not 7.5 mm, as reported in the Conference Paper.
- Distance E has a value of 16.16 mm.
- The constant current density at which the cell was operated during experimental work for the paper is 1.875 mA/cm^2, not 18.75 mA/cm^2. The corrected value is thus, in agreement with the voltage of 2.5 V.

Measurement of bubble shape and size in bubbly flow structure for stagnant and pulsating liquid flow using an undivided electrochlorination cell and Telecentric Direct Image Method

Nikolaj K. Andersen[1]**, Rodica-Elisabeta Stroe**[1]**, Lau Hedensted**[1]**, Anders C. Olesen**[2]**, Jakob Hærvig**[2] **and Henrik Sørensen**[2]
[1]*Thermal Energy And Process Engineering, School of Engineering and Science, Aalborg University*
Fibigerstræde 10, 9220 Aalborg East, Denmark
nkan11@student.aau.dk

[2]*Department of Energy Technology, Aalborg University*
Pontoppidanstræde 111, 9220 Aalborg East, Denmark
aco@et.aau.dk

Abstract

This study presents the measurement of shape and diameter of bubbles in different regions of the bubbly flow structure at the cathode for stagnant and pulsating liquid flow in a single undivided electrochlorination cell. The cell is filled with a dilute sodium chloride electrolyte solution with a concentration of 30 g/L, and operated at a current density of 18.75 mA/cm^2, and stagnant liquid flow, or pulsating liquid flow with a pulsation period of 3.5 s and rate of 760 mL/h. Measurements are conducted using a Telecentric Direct Image Method for acquiring images of the bubbles, and processing is done in MATLAB and NI Vision in LabVIEW to determine shape and diameter of the bubbles. Three bubble regions are observed: adherence, bubble diffusion and bulk region. For stagnant liquid flow the mean bubble diameter increases from 30 to 60 µm going from the adherence region to the bulk region, which is supported by an increase in fraction of total gas volume constituted by large bubbles. For pulsating liquid flow the mean bubble diameter is observed to remain constant around 35 µm when moving across the bubbly flow structure, which likewise is supported by the fraction of total gas volume investigations. Hence, showing horizontal displacement of the three bubble regions with the pulsating liquid flow.

Keywords: Direct imaging, electrochlorination, bubbly flow, bubble size, bubble shape, pulsating liquid flow

1. Introduction

Chlorine is widely used in the water treatment industry, but due to handling risks and hazards, attention has been given to on-site generation in recent years [1, 2]. Electrochlorination cells are devices for on-site hypochlorite generation through salt water electrolysis. Much research has been done experimentally, however fundamental knowledge of the processes occurring are still lacking, hence modelling of the electrochlorination process is necessary for studying the details of the process [2]. The multiphase flow behaviour is an important part of the working principle of the cell. Thus, in order to fully understand the multiphase flow behaviour in such cells, without time expensive resolving of all bubbles numerically, accurate measurements of the bubbles generated at the electrodes are required.

1.1. Measurement and visualisation technique

Many different techniques have been deployed for measuring parameters and visualising phenomena of importance in understanding multiphase flows and the influence of these on the performance of devices and processes. Such phenomena and parameters include flow regime, phase velocity and volume fraction, and bubble diameter distribution.

Bubble diameter and shape as well as flow regime and structure are of great importance since these influence the performance of electrochemical cells. Thus, to obtain these parameters and visualise the flow behaviour, imaging techniques are often used since these do not disturb the flow occurring in the cells.

1.2. Studied hydrodynamic aspects in electrochemical cells

Flow regimes have been studied intensively because generation of bubbles greatly influences the performance of electrochemical cells by hindering the liquid reactants access to the electrode surface [3]. Studies show that bubbly flow is the predominant flow regime in these electrochemical cells, but that transition to slug flow may occur at low liquid flow rates and sufficiently high current densities [3].

Several studies have been conducted on investigating bubble evolution and diameter while varying the current density. It has been seen that increasing the current density increases the bubble generation, in accordance with Faraday's law of electrolysis [3, 4, 5]. As the current density is increased, the mean bubble diameter is seen to increase [3, 6, 7, 8]. Additionally, the mean bubble diameter has been reported to increase in the direction of the flow along the electrode surface [6, 8, 9].

In the bubbly flow, the two phase flow structure occurring has been studied. It has been reported that bubbly flows consist of three regions: adherence, bubble diffusion and bulk region [6]. Furthermore, it was observed that the bubble diameter increases from the adherence region to the bulk region [6]. In the adherence region bubbles stick to or stay close to the electrodes and the thickness of this region is that of the mean diameter of the bubbles. Furthermore, the bubble diameter has been observed to increase along the flow direction in the adherence and bubble diffusion regions [6]. The larger bubbles formed through this growth have been seen to jump from the surface through bursts and into the bulk region along with smaller bubbles they had taken with them during the jump [6]. Quite dispersed bubbles were seen in the bulk region and these bubbles were not observed to grow further in size [6]. In all cases of increasing bubble diameters described in the above, the bubble growth is reported to be caused by coalescence between larger and smaller bubbles, especially in the vicinity of the electrode surface [6], and/or mass transfer from supersaturated zones in the liquid phase [8].

The present study aims at investigating bubble diameter and shape in the adherence, bubble diffusion and bulk regions occurring at the electrode surfaces, under the influence of a pulsating liquid flow. In order to observe the influence of this pulsating flow, a reference investigation is performed in a stagnant liquid flow. Here stagnant liquid flow denotes an inlet velocity of zero for the electrolyte. The above is done using an undivided electrochlorination cell and Telecentric Direct Image Method (TDIM). Such investigations should be performed in the cell gap, however preliminary tests have shown low visibility between the electrodes. Hence, the investigations are carried out by studying the bubble regions above the cathode of the electrochlorination cell since this is the electrode with the predominant bubble generation.

2. Methodology

The TDIM applied in this study involves the capture of images of bubbles and subsequent analysis with the purpose of determining bubble diameter and shape. Thus TDIM enables a clear identification of the bubbles evolving at the cathode, without affecting the fluid dynamics of the system.

2.1. Experimental setup

Figure 1 shows the experimental setup which consists of an undivided electrochlorination cell, a camera, and a LED chipset with camera optics. The electrochlorination cell, with internal dimensions of 40 x 40.4 x 111 mm, is made of plexiglass and fitted with two 40 x 40 mm titanium electrodes with a cell gap of 7.5 mm. The cell has an inlet at the bottom through which the electrolyte enters and an outlet at the top through which the waste solution and the formed gases leave the cell. The electrolyte is a dilute sodium chloride solution with a concentration of 30 ± 0.1 g/L and flow rate of 760 mL/h. The inlet pressure is delivered by a Grundfos DDA 7.5-16 dosing pump with a stroke volume of 0.74 ml, which gives a pulsation period of approximately 3.5 s. The cell is operated at a constant current density of approximately 18.75 mA/cm^2 corresponding to a cell voltage of 2.5 V.

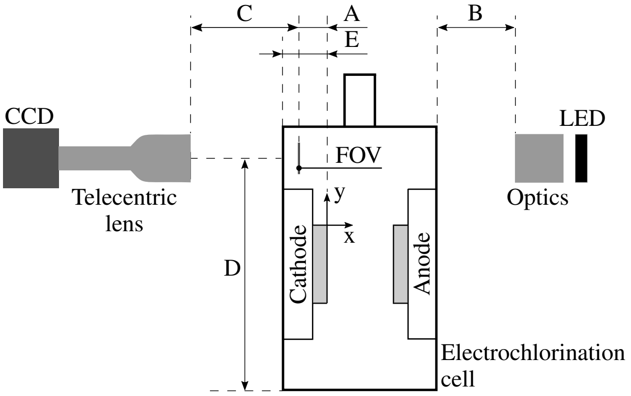

Figure 1: Conceptual drawing of the experimental setup.

The camera is a Basler acA1300-30um USB 3.0 area scan, monochrome CCD camera fitted with an Edmund Optics 63-729 telecentric lens with a 0.5x primary magnification and a working distance (C) of 110 mm. The image resolution of 1280 x 960, sensor pixel size of 3.75 x 3.75 mm and the primary magnification give the system a field of view (FOV) of 9.6 x 7.2 mm. Based on these characteristics, the camera and the optics system yield a pixel size of 7.5 µm. The FOV is located above the cathode at a height (D) of 111.2 mm and with a distance (A) to the plane of the cathode face. The cathode face is located at a distance (E) of 16.18 mm from the inner cell wall. Test are performed by moving across the bubbly flow structure from the normalised horizontal position A/E = -0.35 to A/E = -0.06, hereafter referred to as horizontal position (A/E). The cell and the equipment described above are mounted together on a heavy aluminium structure in order to stabilize the viewing field.

As the bubbles move through the FOV of the imaging system, it is of high importance to reduce perspective, and hence measurement errors. To eliminate perspective errors occurring in the case of conventional lenses used for capturing moving objects, a telecentric lens is chosen. This lens type has a constant, zero angular FOV. Hence, a telecentric lens has a constant magnification and FOV regardless of the distance to the object [10].

The background lighting is provided by a LED chipset mounted together with camera optics. The lighting is placed at a distance (B) of 132.9 to 137.5 mm from the outer surface of the cell, when moving across the bubbly flow structure, and centred with respect to the camera and lens configuration at the height (D). This LED and camera optics combination enables focused lighting at varying intensities.

2.2. Image acquisition settings

For each image series, 100 images are captured at an exposure time of 16 µs. Preliminary measurements showed a minimum bubble velocity of approximately 1 mm/s, hence a dead time of 10 s is set between the capture of each image. This ensures that the same bubbles are not captured across multiple images and therefore do not appear multiple times in the data set. Noting that the pulsation period of 3.5 s does not align with the dead time, the dead time results in a time averaging of the captured bubbly flow structure. Hence, giving an offset of 30 seconds over 100 images.

Furthermore, each image series has a total acquisition time of 16.5 minutes per image series and a total of 10 image series are made.

2.3. Image processing and analysis

The image processing procedure is conducted in two parts; 1) Preprocessing in MATLAB and 2) Processing and analysis using the NI Vision toolbox in LabVIEW. The steps of each part is summarized in Fig. 2.

Figure 3 shows a typical unprocessed image, which includes both in-focus bubbles, with sharp contours and steep greyscale gradients, and out-of-focus bubbles, with soft edges and small greyscale gradients.

The purpose of the preprocessing is to ease the processing in LabVIEW by creating a uniform background, as well as increase the contrast between background and the bubble contours.

The first step of the preprocessing is the removal of the non-uniform background seen in Fig. 3. To do this, the original image is divided by an averaged background image and all results above 1 are set to 1, according to Eqn (1).

$$I_f(x,y) = \frac{I_0(x,y)}{\bar{I}_{BG}(x,y)} \quad \text{if } I_f > 1 \text{ then } I_f = 1 \tag{1}$$

where I_f is the foreground image (without background), I_0 is the original unprocessed image and $\bar{I}_{BG}$ is the averaged background image, which is generated by computing the average of 50 subsequently captured images with the light source on, but the cell turned off. In Eqn (1) values above 1 are set equal to 1 in order to avoid distorting the normalisation. This normalisation, shown in Eqn (2), is then applied to I_f to increase the utilization of the greyscale spectrum.

$$I_n(x,y) = \frac{I_f(x,y) - \min(I_f)}{\max(I_f) - \min(I_f)} \tag{2}$$

where I_n is the normalised foreground image.

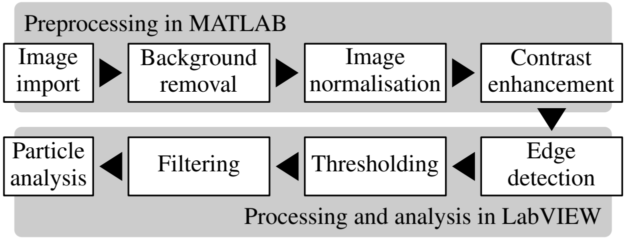

Figure 2: Flowchart of the image processing procedure.

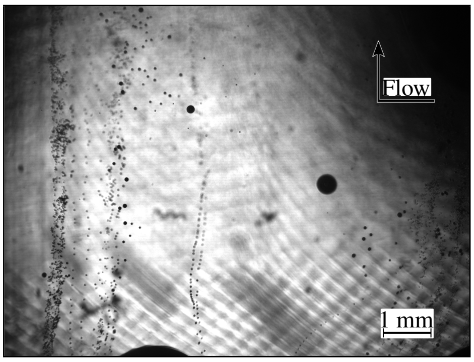

Figure 3: Unprocessed reference image of the two-phase flow.

Then, I_n undergoes contrast enhancement, which increases the greyscale values larger than 0.5 and decreases those smaller than 0.5, hence dark regions are darkened and light regions are lightened [11]. In this study a non-linear intensifier operation, given in Eqn (3), is applied for the contrast enhancement [11].

$$I_c(x,y) = \begin{cases} 2 \cdot [I_n(x,y)]^2 & \text{for } I_n \in [0.0; 0.5] \\ 1 - 2 \cdot [1 - I_n(x,y)]^2 & \text{for } I_n \in]0.5; 1.0] \end{cases} \tag{3}$$

where I_c is the contrast enhanced image. From Fig. 4 it is seen that the image preprocessing has enhanced the quality of the image in terms of bubble recognition - the uneven background has been removed and a larger contrast, and hence greyscale gradients, between particle edges and background has been created, thus, improving the conditions for edge detection.

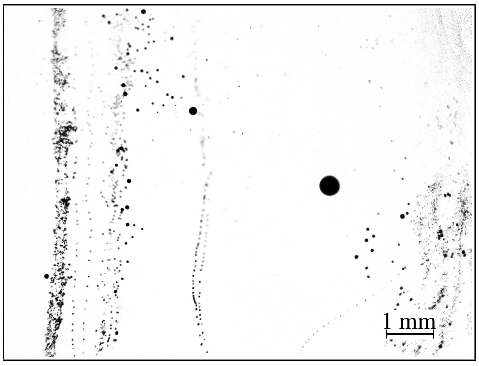

Figure 4: Reference image after preprocessing.

The preprocessed images are further processed and analysed in LabVIEW to determine bubble shape and diameter. This part of the processing aims to remove problematic bubble contours and shapes which alter the accuracy of the measurements, such as bubbles that are out of focus, have incomplete edges or overlap other bubbles. Bubble contours are extracted and outlined by means of an edge detection filter implemented in LabVIEW. The filter applied in this study is the non-linear Roberts filter, which gives in-focus bubbles with sharp edges light and complete outlines, whereas out-of-focus bubbles receive fuzzy, darker or even incomplete outlines. Afterwards a threshold of 80 is applied, which breaks up the fuzzy outlines of out-of-focus bubbles while keeping the outlines of in-focus bubbles closed and intact. The complete contours are then filled and the images go through binary morphology, which includes removal of border objects as well as single pixel sized residue. Furthermore, a ratio of equivalent ellipse axes filter excluding ratios larger than 1.5 is applied in order to remove any incomplete contours left over by the thresholding, as well as overlapping bubbles.

After the processing of the images the bubbles are analysed and bounding rectangle width, which approximates the bubble diameter, and a Heywood Circularity Factor (HCF) are extracted for each bubble. The HCF is defined as the perimeter P of the object divided by the circumference of a circle with the same area A, see Eqn (4). Thus, the closer the shape of an object is to a perfect circle, the closer the HCF is to 1.

$$\text{HCF} = \frac{P}{4\pi A} \tag{4}$$

2.4. *Method verification*

The TDIM was verified by applying it to polyamid particles, with a known mean size of 50 µm, suspended in water. A series of 100 images was captured and processed using the procedure described above resulting in a total of 1342 recognised and measured particles. The size distribution is shown in Fig. 5.

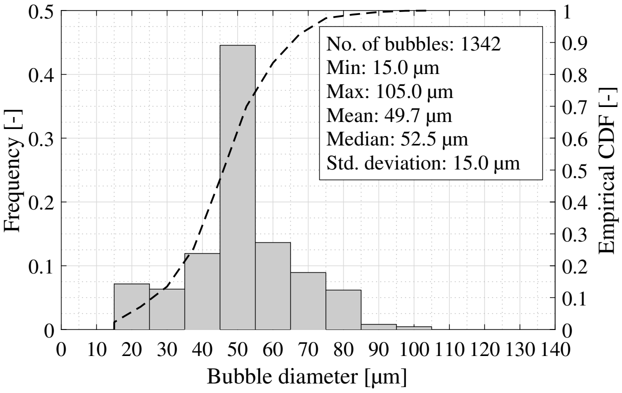

Figure 5: Normalised size distribution of polyamid particles measured using TDIM. The particles have a known mean of 50 µm.

The resulting mean estimate of 49.7 µm, with a confidence interval of approximately ± 0.9 µm, is in agreement with the known diameter of 50 µm. Thus, it is concluded that the applied method is suitable for measuring diameter and shape of bubbles evolving at the electrodes of the electrochlorination cell.

In the above a threshold of 80 was applied in the image processing. The value of the threshold influences which particles (or bubbles) are included in the final data set and which are not. In order to investigate the influence of the threshold, the processing of the polyamid particle images was repeated with thresholds of 70 and 90. The resulting mean size estimates are listed in Table 1 with the results for a threshold of 80.

From Table 1 it is seen that changing the threshold by ± 10 results in an insignificant change of the mean size estimate of approximately ± 3 %, compared to the mean size estimate with a threshold of 80.

Table 1: Estimated mean particle size and number of recognised particles for image processing thresholds of 70, 80, and 90.

Threshold	Estimated mean size [µm]	No. of particles
70	51.2	1701
80	49.7	1342
90	48.2	1065

3. Results

Figure 6 shows the HCF as function of the bubble diameter for bubbles in pulsating and stagnant liquid flow, across all investigated horizontal positions (A/E).

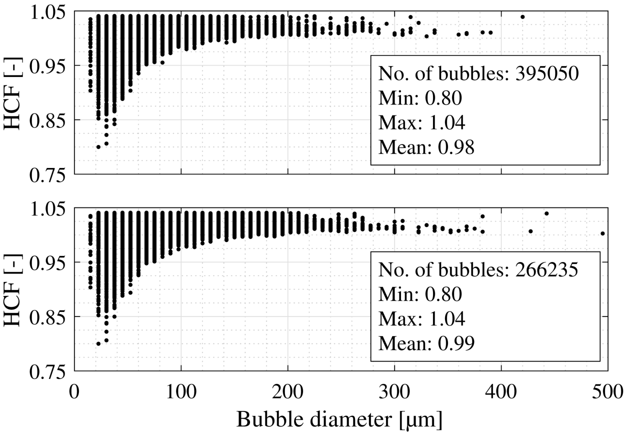

Figure 6: Heywood circularity factor measurements across all horizontal positions (A/E) for pulsating liquid flow (top) at 760 mL/h and stagnant liquid flow (bottom), 18.75 mA/cm^2, 2.5 V, and a salt concentration of 30 g/L.

As seen from Fig. 6 the mean circularity factors for both pulsating and stagnant liquid flow show that the bubbles can be considered spherical and hence the width of the bubbles is regarded as the diameter of the bubbles. Moreover, it is seen that the main portion of the bubbles are located around a circularity factor of 1, which indicates that a large portion are spherical or very close to being spherical. However, Fig. 6 also shows that smaller bubbles have circularity factors as low as 0.8 and hence appear less spherical in the data set.

Figure 7 shows a typical picture of the bubbly flow structure occurring just above and in the plane perpendicular to the cathode of the electrochlorination cell.

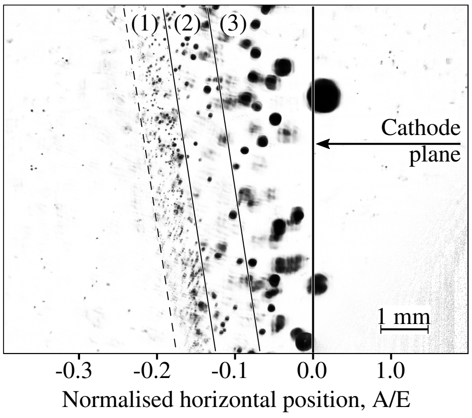

Figure 7: Bubbles above and in the plane of the cathode at 760 mL/h, 37.5 mA/cm^2, 2.8 V and a salt concentration of 30 g/L.

In Fig. 7 small bubbles seem to be confined to the left in the picture, thus being the bubbles coming from the region closest to the electrode surface to which they have been reported to adhere or stay close to. Furthermore, it is seen that the bubble diameter increases going from left to right in the picture and that dispersed large bubbles are seen in the bulk region (3) of the flow. This confirms the observations made by Ref. [6], thus showing the occurrence of three regions in the bubbly flow structure: adherence, bubble diffusion and bulk region as indicated in Fig. 7 by (1), (2) and (3), respectively. Finally, it is seen from Fig. 7 that a larger number of small bubbles are found in comparison to the number of large bubbles.

Figure 8 shows the evolution in mean bubble diameter as a function of the horizontal position (A/E) in the electrochlorination cell. The values are given with a maximum confidence interval of ± 1.1 µm.

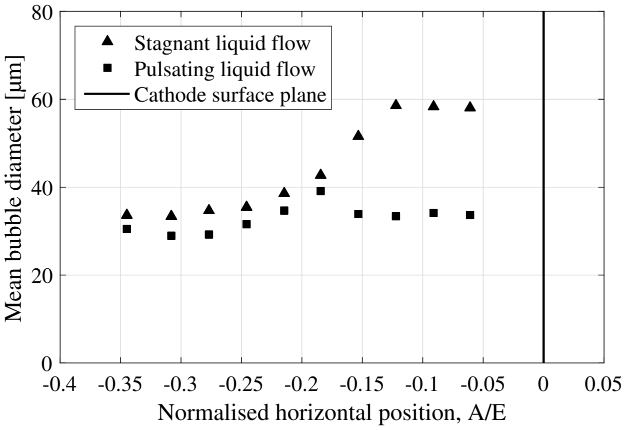

Figure 8: Mean bubble diameter as function of horizontal position (A/E) for stagnant liquid flow and pulsating liquid flow of 760 mL/h, both performed at 18.75 mA/cm^2, 2.5 V and a salt concentration of 30 g/L.

In the case of a stagnant liquid flow, Fig. 8 shows a significant increase in mean diameter of the bubbles as the horizontal position increases from -0.35 to -0.06. In the case of a pulsating flow only small variations exist in the mean bubble diameter as the horizontal position increases, and a maximum diameter difference of 10 µm is seen between A/E = -0.35 and A/E = -0.18. This is expected considering the time averaging of the bubble diameters occurring between the three regions of the bubbly flow structure. Comparing the mean bubble diameter for the stagnant and pulsating liquid flows at the different horizontal positions, it is seen that reasonable agreement exists between the mean bubble diameters at horizontal positions from -0.35 to -0.18. For A/E greater than -0.18 the mean bubble diameters are seen to deviate from each other. Moving from the adherence region (1) to the bulk region (3) means that small bubbles should move out of focus and large bubbles into focus, whereby the recognised number of small and large bubbles should decrease and increase, respectively.

Figures 9 and 10 show the fraction of total gas volume as function of bubble diameter for stagnant and pulsating liquid flow, respectively, at horizontal positions (A/E) of -0.35, -0.18 and -0.06.

As seen from Fig. 9 the fraction of total gas volume for small and large bubbles decreases and increases, respectively, as A/E goes to zero. This indicates that more small and large bubbles have moved out of and into focus, respectively, as the horizontal position increases. From Fig. 10 it is seen that the fraction of total gas volume for small and large bubbles decreases and increases, respectively, at a horizontal position of -0.18 compared to a horizontal position of -0.35 as expected from Fig. 9. However, at a horizontal position of -0.06 the reverse trends with little to no large bubbles are seen.

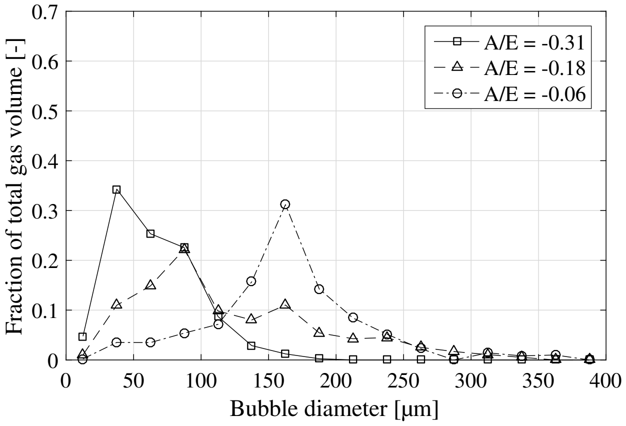

Figure 9: Fraction of total gas volume as function of bubble diameter at horizontal positions (A/E) of -0.35, -0.18 and -0.06 for stagnant liquid flow at 18.75 mA/cm^2, 2.5 V, and a salt concentration of 30 g/L.

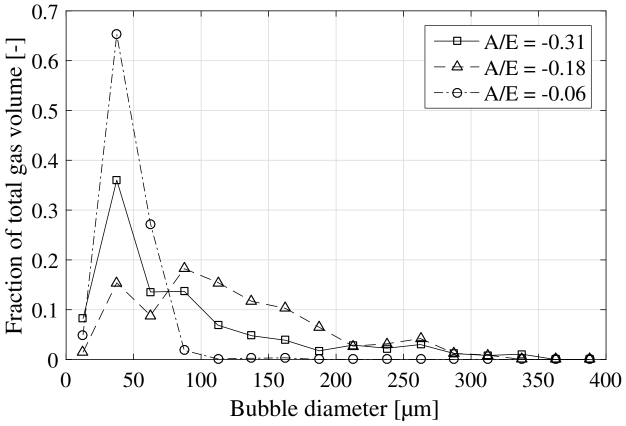

Figure 10: Fraction of total gas volume as function of bubble diameter at horizontal positions (A/E) of -0.35, -0.18 and -0.06 for pulsating liquid flow at 760 mL/h, 18.75 mA/cm^2, 2.5 V, and a salt concentration of 30 g/L.

4. Discussion

In terms of bubble shape, it is seen that the HCF of the bubbles concentrates around 1. However, the factor can go as low as 0.8 for small bubbles, as shown in Fig. 6. This is expected to be caused by small bubbles only consisting of a few pixels. Hence, a bubble can have an unclear edge, if the bubble is slightly out of focus or light reflections within the cell affecting the bubble. Thus, a pixel can be lost in the height or width of the bubble, thus skewing the shape of the bubble and make it appear non-spherical.

For stagnant liquid flow it is observed that the mean bubble diameter increases as the horizontal position increases as shown in Fig. 8. This is further supported by the fraction of total gas volume as function of bubble diameter, illustrated in Fig. 9, where the fraction of total gas volume of small and large bubbles decrease and increase, respectively, as the horizontal position in the cell is increased. Hence, indicating that small bubbles have moved out of focus and large bubbles into focus. These observations are in line with the bubbly flow structure shown in Fig. 7, where the diameter of the bubbles are seen to increase moving from the adherence region (1) to the bulk region (3).

For pulsating liquid flow small variations in mean bubble diameters as function of horizontal position are observed, where only a difference in bubble diameter of 10 µm is found. These small variations are further supported by the fraction of total gas volume as function of bubble diameter, as illustrated in Fig. 10, where the fraction of total gas volume for small and large bubbles decrease and increase, respectively, up to a horizontal position (A/E) of -0.18 after which the reverse trend is observed. These observations are inconsistent with the bubbly flow structure shown in Fig. 7. Hence, indicating that small and large bubbles move across the horizontal positions, where they were located in the case of stagnant liquid flow. Figure 11 illustrates the evolution in the bubbly flow structure during a pulsation in the liquid flow by the used dosing pump. At t = 9 s the pulsation by the pump is initiated. At t = 10.8 s a considerable displacement to the left is seen for the adherence and bubble diffusion regions, whereas the bulk region, and hence the large bubbles, appears unaffected by the pulsating liquid flow. The significant difference in time between the two frames is explained by the delay in time between the initiated pulsation of the pump and its influence on the bubbly flow structure is observed. At t = 12.5 s a similar bubbly flow structure as at t = 9 s is observed, after which the periodic cycle reoccurs at a frequency approximately equal to the stroke frequency of the dosing pump. The pulsating liquid flow thus creates a sideways displacement of the bubbly flow structure evolving at the cathode. This displacement of the bubbly flow structure makes the differentiation between the three bubble regions difficult, and furthermore causes mixing of the bubble diameters. Hence, due to a larger production of small bubbles compared to large bubbles the mean bubble diameter is favoured towards that of the small bubbles.

The time averaging of the pulsating liquid flow is seen to indicate a stable mean of the bubble diameter for all horizontal positions. This is further verified by the visualisation of the displacement of the three regions in the bubbly flow structure and mixing of the bubble diameters, shown in Fig. 11. Hence, the displacement of specific bubble diameters could be further investigated by synchronising the camera with the pulsation period of the dosing pump. Thus, the same mean bubble diameters are expected to be acquired at increased horizontal positions compared to the stagnant liquid flow. The current investigations were carried out at one current density as well as with electrodes of a certain size. Further investigations could be conducted at varying current density, which are expected to show an increase in bubble diameter at increasing current density, as reported by Refs. [3, 6, 7, 8]. Similarly, more investigations could be performed with electrodes of decreasing and increasing height. Such investigations are expected to show bubbles with decreasing and increasing diameter, respectively, since bubbles have been observed to increase along the electrode surface due to coalescence with other bubbles and/or mass transfer from supersaturated zones in the liquid phase to the bubbles [6, 8].

5. Conclusion

The aim of this study has been to investigate the three bubble regions reported in the literature: adherence, bubble diffusion and bulk region, under the influence of a pulsating flow. To clearly isolate the effect of the pulsation, a reference investigation at stagnant liquid flow has been performed as well. These investigations have been done using an undivided electrochlorination cell and a Telecentric Direct Image Method (TDIM).

The applied TDIM was verified using polyamid particles of a known mean size of 50 µm. The verification showed that the ap-

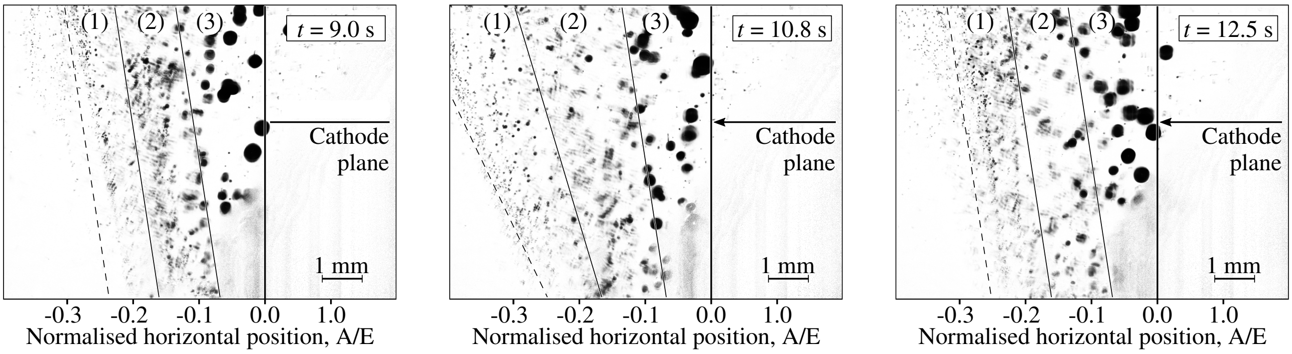

Figure 11: Displacement of the three bubble regions for sequentially captured images during one pulsation period of the dosing pump. Regions: (1) adherence, (2) bubble diffusion, (3) bulk.

plied method estimates a mean size of the polyamid particles of 49.7 μm and thus the TDIM is found applicable for determination of bubble shape and diameter.

The three bubble regions reported to be occurring in bubbly flows are identified: adherence, bubble diffusion and bulk region. The bubble diameter is observed to increase moving from the adherence region to the bulk region.

For stagnant liquid flow it is found that the mean bubble diameter significantly increases with increasing horizontal position in the electrochlorination cell. Furthermore, the fraction of total gas volume for small and large bubbles is found to decrease and increase, respectively, as the horizontal position increases. This is in agreement with the observed increase in bubble diameter across the bubbly flow structure.

For pulsating liquid flow only small variations in mean bubble diameter are observed with increasing horizontal position. Moreover, the pulsating liquid flow shows a more uniform distribution in fraction of total gas volume across different bubble diameters at different positions, which likewise supports the small variations in mean bubble diameter for pulsating liquid flow. The pulsating liquid flow, created by the applied dosing pump, is seen to displace the bubble regions horizontally. Hence, making the differentiation of the three different bubble regions difficult as well as causing mixing of the bubble diameters. This is due to a larger production of small bubbles compared to large bubbles as well as the time averaging resulting from the test methodology, thus favouring the mean diameter towards that of the small bubbles.

6. Acknowledgements

The authors would like to thank Grundfos Holding A/S for providing financial support as well as the electrochlorination system used for measurements. Furthermore, the authors would like to thank Karin Doolewerdt, Maryam Momeni and Helge Grann for very valuable discussions and much knowledgeable criticism.

References

[1] Spasojević, M., Krstajić, N., Spasojević, P. and Ribic-Zelenović, L., Modelling current efficiency in an electrochemical hypochlorite reactor, *Chem. Eng. Res. Des.*, 93, pp. 591-601, 2015.

[2] Cheng, C. and Kelsall, G., Models of Hypochlorite production in electrochemical reactors with plate and porous anodes, *J. Appl. Electrochem.*, 37, pp. 1203-1217, 2007.

[3] Dedigama, I., Angeli, P., Ayers, K., Robinson, J., Shearing, P., Tsaoulidis, D. and Brett, D., In situ diagnostic techniques for characterisation of polymer electrolyte membrane water electrolysers - Flow visualisation and electrochemical impedance spectroscopy, *Int. J. Hydrogen Energy*, 39, pp. 4468-4482, 2014.

[4] Aldas, K., Pehlivanoglu, N. and Mat, M., Numerical and experimental investigation of two-phase flow in an electrochemical cell, *Int. J. Hydrogen Energy*, 33, pp. 3668-3675, 2008.

[5] El-Askary, W., Sakr, I., Ibrahim, K. and Balabel, A., Hydrodynamics characteristics of hydrogen evolution process through electrolysis: Numerical and experimental studies, *Energy*, 90, pp. 722-737, 2015.

[6] Boissonneau, P. and Byrne, P., An experimental investigation of bubble-induced free convection in a small electrochemical cell, *J. Appl. Electrochem.*, 30, pp. 767-775, 2000.

[7] Nagai, N., Takeuchi, M. and Nakao, M., Effects of Generated Bubbles Between Electrodes on Efficiency of Alkaline Water Electrolysis, *JSME Int. J.*, 46, pp. 549-556, 2003.

[8] Abdelouahed, L., Hreiz, R., Valentin, G., Poncin, S. and Lapicque, F., Hydrodynamics of gas bubbles in the gap of lantern blade electrodes without forced flow of electrolyte: Experiments and CFD modelling, *Chem. Eng. Res. Des.*, 111, pp. 255-265, 2014.

[9] Dedigama, I., Angeli, P., Dijk, N., Millichamp, J., Shearing, P., Tsaoulidis, D. and Brett, D., Current density mapping and optical flow visualisation of a polymer electrolyte membrane water electrolyser, *J. Power Sources*, 265, pp. 97-103, 2014.

[10] Li, D. and Tian, J., An accurate calibration method for a camera with telecentric lenses, *Optics and Lasers in Engineering*, 51, pp. 538-541, 2013.

[11] Chaira, T., Ray, A.K., *Fuzzy Image Processing and Applications with MATLAB*, first ed., CRC Press, Florida, 2010.

Appendix B

Laboratory work

This appendix serves to describe the experimental setup as well as the applied experimental conditions, procedures and obtained results.

B.1 Experimental setup

This section serves to describe the experimental setup, used for the Telecentric Direct Image Method (TDIM), in terms of equipment and their working principle. Figure B.1 shows the experimental setup used for bubble image acquisition.

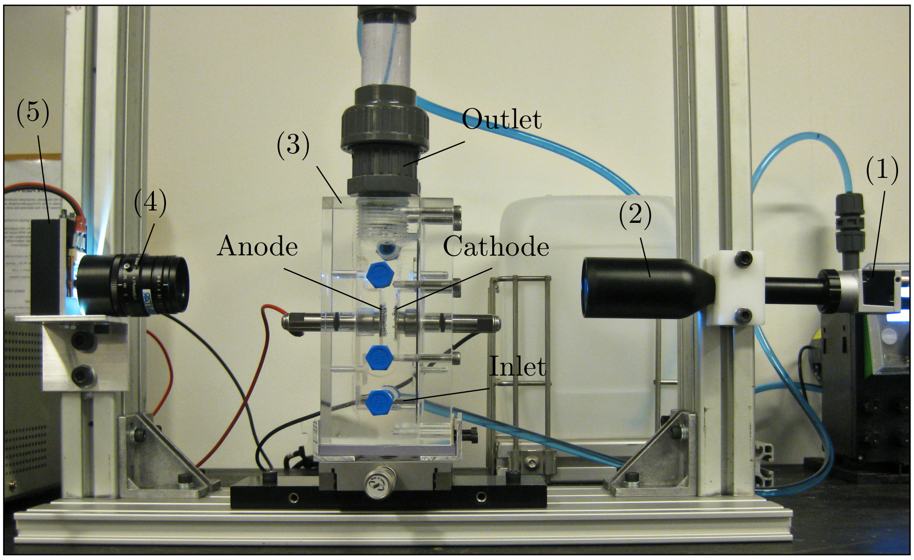

Figure B.1. Experimental setup used for TDIM.

Table B.1 lists the manufacturer, model, and AAU number of the devices that are part of this setup. The experimental setup is designed to achieve the electrolysis of an aqueous sodium chloride solution, which takes place together with bubble evolution, and to determine the size distribution and velocity of the formed bubbles.

Table B.1. List of devices, manufacture, model, and AAU number.

Device	Manufacturer	Model	AAU No.
Electrochlorination cell (3)	Grundfos	-	-
Pump	Generic submersion pump from Biltema		
Power supply x 2	GW Instek	GPS-4303	79077, 87768
LED chip (5)	Phlatlight	-	-
Digital cameras (1)	Basler	acA1300-30um	-
	Basler	acA1920-155um	-
Camera optics (2),(4)	Edmund Optics	63-729	109934
	Navitar	NMV-25M1	-
Data acquisition system	National Instruments	NI USB-6215	74279
Flow meter	Omega	FLR1008	-

In Figure B.1, the main components are marked with numbers. These will be used as reference throughout the following.

B.1.1 Electrochlorination cell

The electrochlorination cell (3) is made out of plexiglass with internal dimensions of $40\,\text{mm} \times 40\,\text{mm} \times 111\,\text{mm}$ and is equipped with two $40\,\text{mm} \times 40\,\text{mm}$ electrodes. Both electrodes are made of titanium, of which the anode is coated with ruthenium oxide (RuO_2), and are mounted at a distance of 7.68 mm relative to each other, cell gap. As seen in Figure B.1, the cell has an inlet at the bottom through which the electrolytic solution is fed and an outlet at the top through which the formed gases are exhausted and the product solution leaves the cell.

B.1.2 Digital cameras

The digital cameras (1) used for image capturing of evolved bubbles are manufactured by Basler and used depending on the type of the experiment to be conducted, as described in Chapter 4. Their technical details are given in Table B.2.

Table B.2. Technical data for Basler cameras [Basler, 2016a,b].

	Basler acA1300-30um	Basler acA1920-155um
Resolution [px]	1294 x 964	1920 x 1200
Pixel Size [µm]	3.75 x 3.75	5.86 x 5.86
Max. frame rate [fps]	30	164
Sensor type	CCD	CMOS
Sensor model	Sony ICX445	Sony IMX174
Max. image circle	1/3 "	1/1.2 "
Shutter	Global	Global
Interface	USB 3.0	USB 3.0

It can be seen from Table B.2 that the cameras use different types of sensors, but broadly speaking CCD and CMOS image sensors are integrated circuits based on silicion, consisting of a matrix of photodiodes, which convert light energy, in the form of photons, into electronic charges. Through the photoelectric effect the photon releases an electron and produces a hole as a consequence. The sensor collects these photogenerated electrons on its "potential wells" or pixels during the exposure. The more light striking the sensor the more electrons are collected on a pixel. The electrons are then transferred to the output circuit, where the output signal is converted into digital images through an analog-to-digital converter and transferred to the computer for image regeneration or processing.[Li and Nathan, 2005; Devadhasan et al., 2015]

B.1.3 Telecentric lens

Similar to the human vision, the angular fields of view (FOV) of conventional lenses result in a decreasing magnification, as the distance between the lens and object increases. This causes a perspective error, which decreases the accuracy of the measurements, as the measurements of the vision system will change as the object is moved, due to the change in magnification, as seen in Figure B.2.

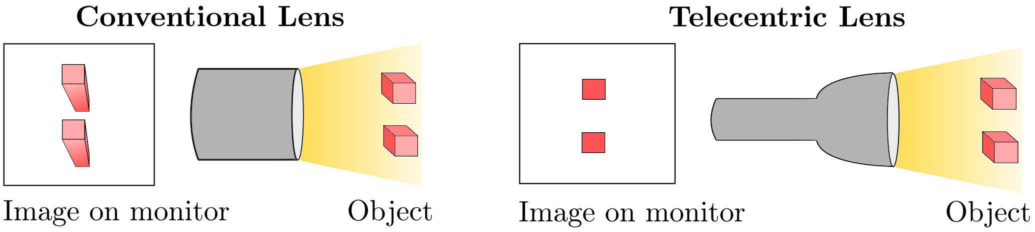

Figure B.2. Visual representation of perspective error in the case of a fixed length (conventional) lens and elimination of this error by means of a telecentric lens. Inspired by Edmund Optics [2016b].

For bubble size determination measurement errors of this kind are not acceptable, since it is of high importance to reduce the perspective error, in order to avoid a false determination of size.

To eliminate the perspective error a telecentric lens (2) is used with the digital camera. This type of lens have a constant, zero angular FOV, meaning that regardless of the distance from the lens, a telecentric lens will always have the same FOV. How size measurements can be unreliable with conventional lenses and how objects at different distances from each other are seen through a telecentric lens in Figure B.3.

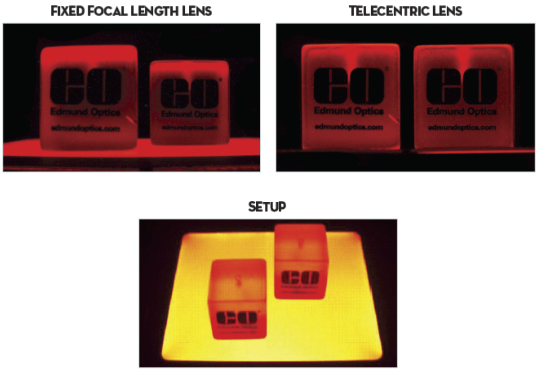

Figure B.3. Objects of the same size at different distances seen through a conventional lens (*top left*) and a telecentric lens (*top right*) [Edmund Optics, 2015b].

As illustrated, the angular FOV of the fixed focal length lens gives a perspective error in the image, causing the two cubes to appear of different sizes. [Edmund Optics, 2015b]

The experimental setup is thus equipped with a 63-729 telecentric lens from Edmund Optics. Its characteristics are shown in Table B.3 and a short explanation of each parameter is given below.

Table B.3. Technical data for Edmund Optics 63-729 Telecentric Lens [Edmund Optics, 2015a].

Edmund Optics 63-729 Telecentric Lens	
Primary magnification	0.5x
Working distance	110 mm
Field of Depth	±1.9 mm
Field of View (1.3" sensor)	9.6 mm
Telecentricity	$< 0.05°$
Distortion	< 0.25 %

The *magnification* refers to the size of the image relative to the object, thus, having a magnification of 0.5x the lens will reduce the size of the object by a factor of 2 onto the imaging plane. The *working distance* is a fixed parameter for a telecentric lens and represents the distance from the front of the lens' housing to its focus plane. The *Field of View* is the maximum size that the object can have, in order for it to be processed. The *telecentricity* is the angular deviation influencing the primary ray compared to a ray parallel to the optical axis. It is desired to have a value as low as possible to get an accurate image. The *distortion* is an absolute deviation which depends on the height of the image. [Petrozzo and Singer, 2001] The *Field of Depth* is the ability of the lens to maintain a desired amount of image quality, without having to refocus, when the object is closer to and farther from the best focus [Edmund Optics, 2016a].

With respect to the working distance it is important to note that the 110 mm listed in Table B.3 is the working distance provided by the manufaturer in the datasheet of the telecentric lens. However, during preliminary measurements it was found that the practical working distance was 120 mm, as listed in Table 4.1 on page 16. It has not been possible to find an explanation for this change of the working distance, but nothing has indicated that this change influenced the measurements.

B.1.4 Other equipment

The most suitable *lighting* for the setup is a telecentric lighting to be used in parallel with the telecentric lens. This combination provides sharp edges, as well as accuracy and reliability of the results [Hornberg, 2006]. Even though it would be the best choice as a light source, this would require a second telecentric lens with a FOV equal to or larger than the FOV of the primary lens. Such a lens was unavailable and instead a LED chipset (5) of red color is utilised together with camera optics (4) to allow a better focus of the light.

Two *power supplies* are used - one delivers power to the electrodes and the LED, and the other one to the pump and flow meter. These are GPS-4303 GW Instek 4-channel

200 W DC Power Supplies, with main applicability in tests and measurements. The power supply output is adjustable, making it easy to control the current and voltage fed to the electrodes.

For measuring the flow rate of the electrolytic solution delivered by the pump an Omega flow meter is used along with a NI USB-6125 *Data Acquisition system (DAQ)* for data sampling. The relevant technical data of the data acquisition module is given in Table B.4. The DAQ module measures the voltage generated by the output signal of the flow meter, thus the flow rate can be monitored and controlled.

Table B.4. DAQ module technical data [National Instruments, 2016].

NI USB-6125 DAQ Module	
Measurement type	Voltage V
Max. voltage range	±10 V
Resolution	16 bits
No. channels	8 differential or 19 single ended

The *flowmeter* used to monitor the flow rate to the cell is an Omega FLR1000 series flow sensor. The flow rate of the liquid is determined by a Pelton-type turbine characterised by high turndown ratios, fast response, and repeatable accuracy. As this turbine rotates proportional to the liquid flow rate, electrical pulses are generated, which constitute the DC voltage output transmitted to the DAQ module[Omega, 2016]. Additional data about the used model, FLR1008, is given in Table B.5.

Table B.5. Flow meter technical data [Omega, 2016].

Omega FLR1008 Flow meter	
Output signal	0 - 5 Vdc
Power input	12 Vdc
Flow range	20 - 200 mL/min
Max. pressure drop	10 psi
Accuracy	±3%

B.2 Experimental conditions and procedures

The conditions under which the different experiments are carried out are presented in this section, together with the laboratory procedures applied for determining the mean bubble size and its variation with current density, as well as for determining the bubble velocity.

B.2.1 Experimental conditions

The experimental conditions under which bubble size and velocity determinations are made, were described in Section 4.2. Certain parameters are kept constant or varied during the different conditions under which data is collected. The electrolytic solution has the same concentration for all measurements, namely 30 g of NaCl to each 1 L of water.

The rate at which this solution flows to the cell is 2 L/h and the power settings for the flow meter are 15 V and 0.3 A.

B.2.2 Experimental procedures

The two types of measurements conducted have similarities, but also distinguish themselves with respect to the image acquisition method. The common part of the procedure will be presented first.

The electrolytic solution is made by weighing 90 g of salt and mixing it with 3 L of deionised water, thus obtaining the reported electrolytic concentration of 30 g/L. The pump is turned on in order to fill the cell with the electrolytic solution and afterwards the cell is supplied with power. The flow meter and lighting are also turned on, where the settings for the lighting vary depending on the amount of bubbles produced which can cloud and darken the acquired images.

As the cell is powered on, bubbles start to evolve at the electrodes and the software NI MAX is started up so that the flow can be visualised. Before starting the image acquisition session the cell is left to run until the flow seems to level and the production of gas bubbles is constant. As the flow "settles" the VI set up in LabVIEW is used to capture images is started. The distance from the lens to the cell (distance C in Figure 4.3 on Page 15) is changed for each set of images taken due to the presence of different bubble sizes which are grouped in three regions, defined with respect to the working electrode, i.e. the cathode; the regions are adherence, diffusion and bulk region, characterised by small, medium, and large bubbles, respectively. The existence of this flow structure has been reported in the literature, as well as in the Conference Paper. The FOV is placed over the cathode, its location being given in Figure 4.3.

The aspects that differentiate the two types of measurements are described in the following.

Task (A) - Bubble size determination

When images are captured for the purpose of determining the variation in mean bubble size with varying current density, the applied voltages to the cathode were: 2.57 V, 2.66 V, 2.73 V and 2.78 V, corresponding to current densities of 1.25 mA/cm^2, 2.5 mA/cm^2, 3.75 mA/cm^2 and 5 mA/cm^2, respectively. As stated, the images are taken at different distances inside the cell, normalised positions A/E of -0.04 to 0.28. The acquired data consists of sets of 100 images together with 50 background images for each combination of current density and position, with a dead time of 10 s between each image. The camera used is the Basler acA1300-30um CCD camera.

Task (B) - Bubble velocity measurements

Images for the bubble velocity determination are taken in the form of 4 sets of 100 sequences, each consisting of 15 images, together with 50 background images, with the Basler acA1920-155um CMOS camera at 150 fps. The variation of current density is no longer targeted in this case, thus the conditions at which the cell operates are constant: 2.66 V and 40 mA. For these measurements normalised positions, A/E, of 0.10, 0.16, 0.22 and 0.28 are applied.

Flow visualisation

Experiments carried out for bubble size determination and velocity have shown that inside the cell the bubble flow structure is displaced to the right when exiting the cell gap. In order to visualise this displacement the layout of the setup is changed compared to bubble size and velocity measurements. The alternative layout can be seen in Figure B.4. The FOV is located at the same position, above the cathode, where most of the bubbles evolve.

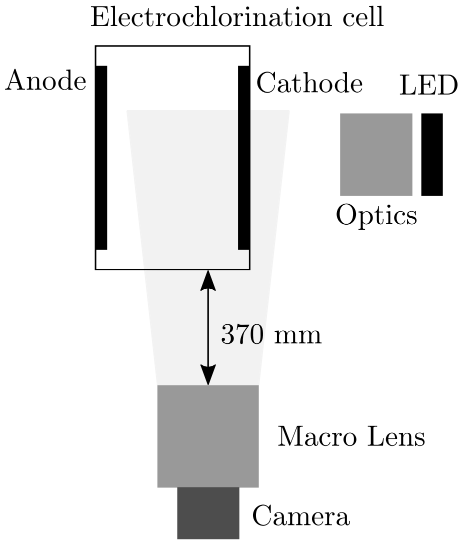

Figure B.4. View of the setup from above. Layout used for flow visualisation image capture.

In order to visualise the displacement three sets of 150 images were captured with the Balser acA1920-155um camera at an exposure time of 13000 µs and a frame rate of 65 fps. The camera is connected to a Sigma 105mm f/2.8 EX DG macro lens. The sets were taken at different current densities - 2.5 mA/cm^2, 3.75 mA/cm^2 and 5 mA/cm^2, corresponding to cell voltages of 2.57 V, 2.66 V and 2.73 V, respectively. The distance from the cell to the lens is set to 370 mm.

The images are then processed by means of the Dantec DynamicStudio software, which is a software package for image acquisition and analysis in applications such as Particle Image Velocimetry (PIV), Laser Induced Fluorescence (LIF), Laser Induced Incandescence (LII), and Particle Sizing [Dantec Dynamics A/S, 2015]. After the images are acquired analysis methods can be applied. For the flow visualisation the methods applied are the Adaptive correlation method, which calculates the velocity vector field, and the Universal outlier detection method, which detects and optionally substitutes false vectors [Dantec Dynamics A/S, 2015]. A 32 x 32 px interrogation window with 25% overlap, 3 refinement steps, and moving average validation is used. For more information on how these methods work and settings apllied the reader is referred to Appendix E.

B.3 Bubble size and velocity measurement results

This section presents the results obtained from the measurement of bubble size and velocity. This includes results which were not found to be necessary to be included in the main body of this document as well as a explanation of the choice to change the purpose of the bubble size measurements, as described in Chapter 4.

Throughout the following and in the report the mean values, standard deviations and 95 % confidence intervals have been computed using Equations (B.1) to (B.3). Note that the confidence intervals are computed under the assumption that the measurements are normally distributed, $N \geq 30$ [Walpole et al., 2011].

$$\bar{h} = \frac{\sum_{i=1}^{N} h_i}{N} \tag{B.1}$$

$$\mathrm{std}(h) = \sqrt{\frac{1}{N-1}\sum_{i=1}^{N} |h_i - \bar{h}|} \tag{B.2}$$

$$\mathrm{CI}_{95\%} = \bar{h} \pm 1.96\frac{\mathrm{std}(h)}{\sqrt{N}} \tag{B.3}$$

B.3.1 Bubble size measurements at varying current density

The initial measurement results of the mean bubble size for current densities of 1.25, 2.50, 3.75 and 5.00 mA/cm^2 and multiple horizontal positions (A/E) are shown in Figure B.5.

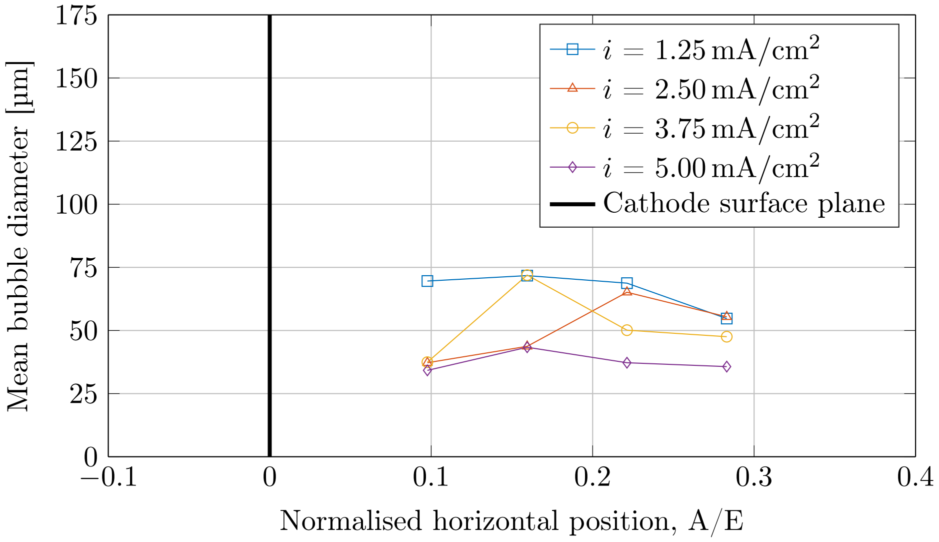

Figure B.5. Initial measurement results for mean bubble diameter as function of horizontal position (A/E) for multiple current densities. All measurements were performed with a cell gap of 7.68 mm and NaCl concentration of 30 g/L.

Two problems are observed from Figure B.5. Firstly, the results for the series at 2.50 and 3.75 mA/cm^2 show somewhat inconsistent size changes across the different positions in the cell. This conflicts with the experience obtained during the work with the Conference Paper (see Appendix A), where the bubble size change with the horizontal position generally was seen to occur in a smooth manner, like the results at 1.25 mA/cm^2. Secondly, Figure B.5 shows the mean bubble size to decrease with increasing current density. This directly contradicts the literature which states that the mean bubble diameter increases with increasing current density [Boissonneau and Byrne, 2000; Nagai et al., 2003; Abdelouahed et al., 2014; Dedigama et al., 2014].

As a result of the problems noted above, the procedure and experimental setup were reviewed in order to try and determine the cause of these problems. During this it was found that the flow meter, which had been changed shortly before the measurements of Figure B.5 were conducted, had been set up wrong and hence produced floating measurements. This was rectified and the measurements repeated. The results are shown in Figure B.6.

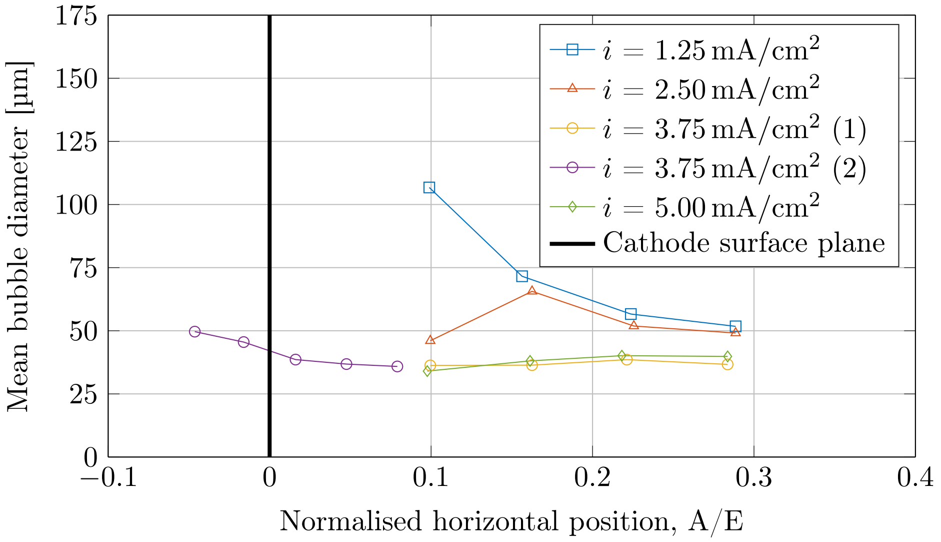

Figure B.6. Final measurement results for mean bubble size as function of horizontal position (A/E) for multiple current densities. All measurements were performed at a constant liquid flow rate of 2 L/h, a cell gap of 7.68 mm and a NaCl concentration of 30 g/L.

From Figure B.6 it is seen that the results are much more consistent compared to Figure B.5, but the problem with decreasing bubble sizes for increasing current densities persists. After some discussion, it was suggested to do additional measurements at positions moving closer to and past the cathode surface plane with the argument that larger bubbles would be less influenced by the liquid phase flow and thus, be positioned above the electrode to a greater extent than the small bubbles. However, it was quickly observed that the bubble size did not change much as the FOV was moved past the cathode plane, as can be seen from the extra measurement set at 3.75 mA/cm^2 (marked with (2) in Figure B.6).

To explain why the measurements consistently show smaller mean bubble sizes for increased current density, it is necessary to look at the raw bubble shadow images. Figure B.7 shows four examples of bubble images captured at a current densities of 1.25, 2.50, 3.75 and 5.00 mA/cm^2.

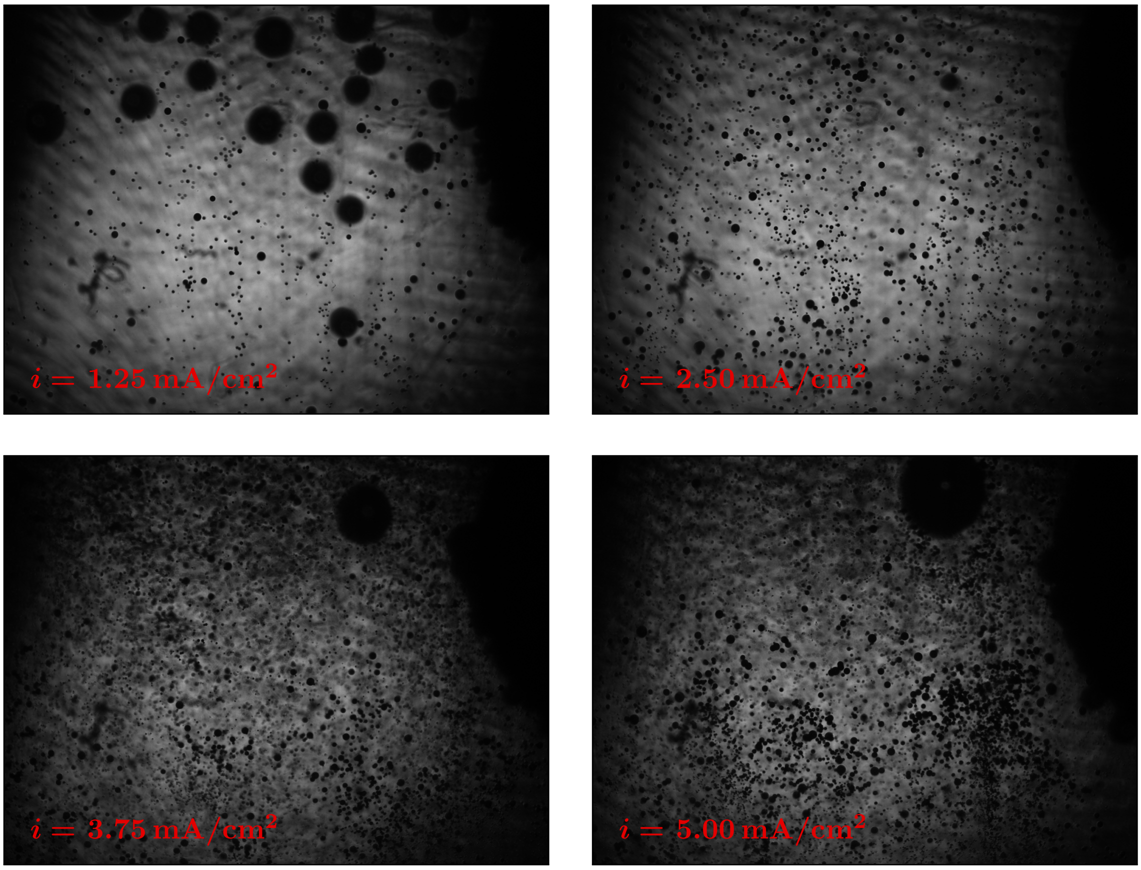

Figure B.7. Examples of bubble shadow images captured at current densities of 1.25, 2.50, 3.75 and 5.00 mA/cm^2 at normalised horizontal positions (A/E) of approximately 0.22.

Comparing the images in Figure B.7 it is seen that the amount of bubbles in the images increases greatly with the current density. Hence, at low current densities, very few bubbles overlap and thus it is easier to identify both larger and smaller bubbles. However, at higher current densities the bubble density is so large that the large bubbles become obfuscated by clouds of smaller bubbles and only the smaller bubbles are clearly visible between these clouds. The result is that the edges of the large bubbles cannot be identified and thus these bubbles are not suitable for size measurement, and these well be ignored by the data processing as it was intended.

Based on the above, it is concluded that the problematic observations of decreasing bubble size with increasing current density is a result of the limitations of the applied methodology. Due to time constraints on this project it has been chosen not to invest any further effort in resolving this problem, but rather to not use the faulty measurements obtained at current densities of 3.75 mA/cm^2 and 5.00 mA/cm^2 and repurpose the measurements obtained at current densities of 1.25 mA/cm^2 and 2.50 mA/cm^2, as these resembles the measurements obtained during the work for the Conference Paper, to create a single estimate of the mean bubble size to be used as input to the model, as well as local gas volume fractions at each position to be used for validating the model. From the data collected at 1.25 mA/cm^2 and 2.50 mA/cm^2 the mean bubble size is determined to be 62.4 µm. The number of recognised bubbles as well as the confidence intervals for each of the mean values given in Figure B.6 are provided in Figures B.8 and B.9, respectively.

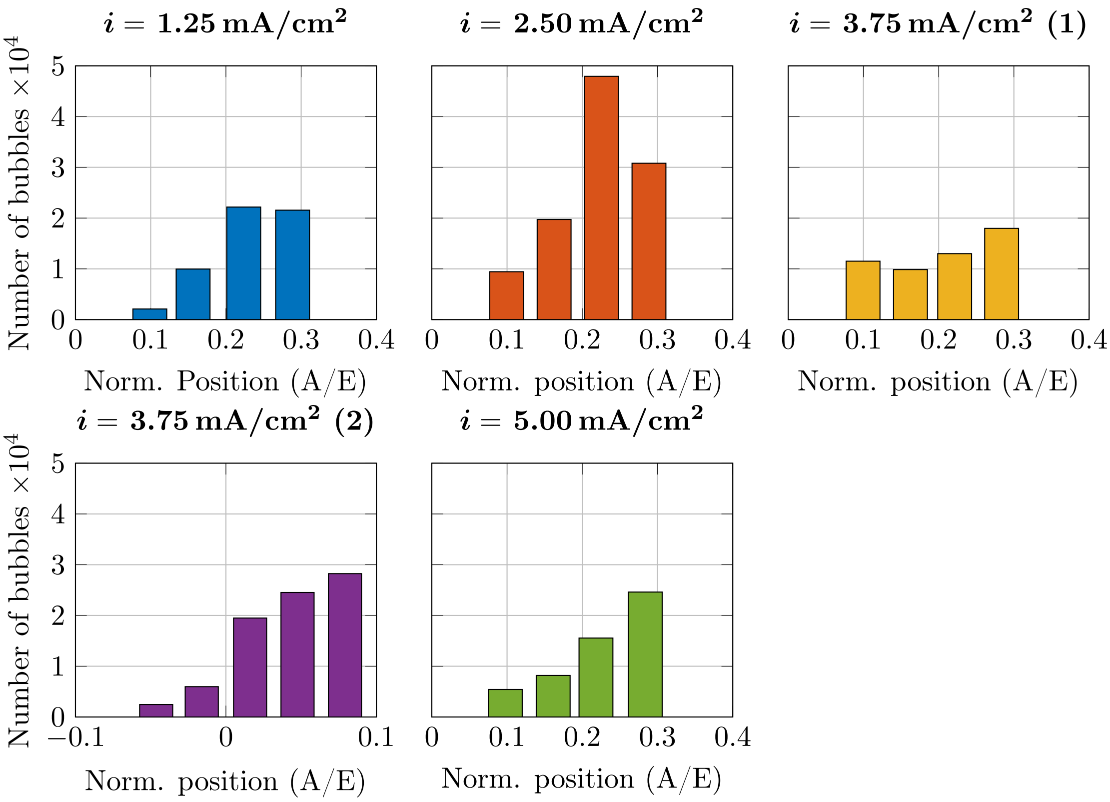

Figure B.8. Number of recognised bubbles plotted as function of the normalised horizontal position (A/E) for each position and current density combination in Figure B.6.

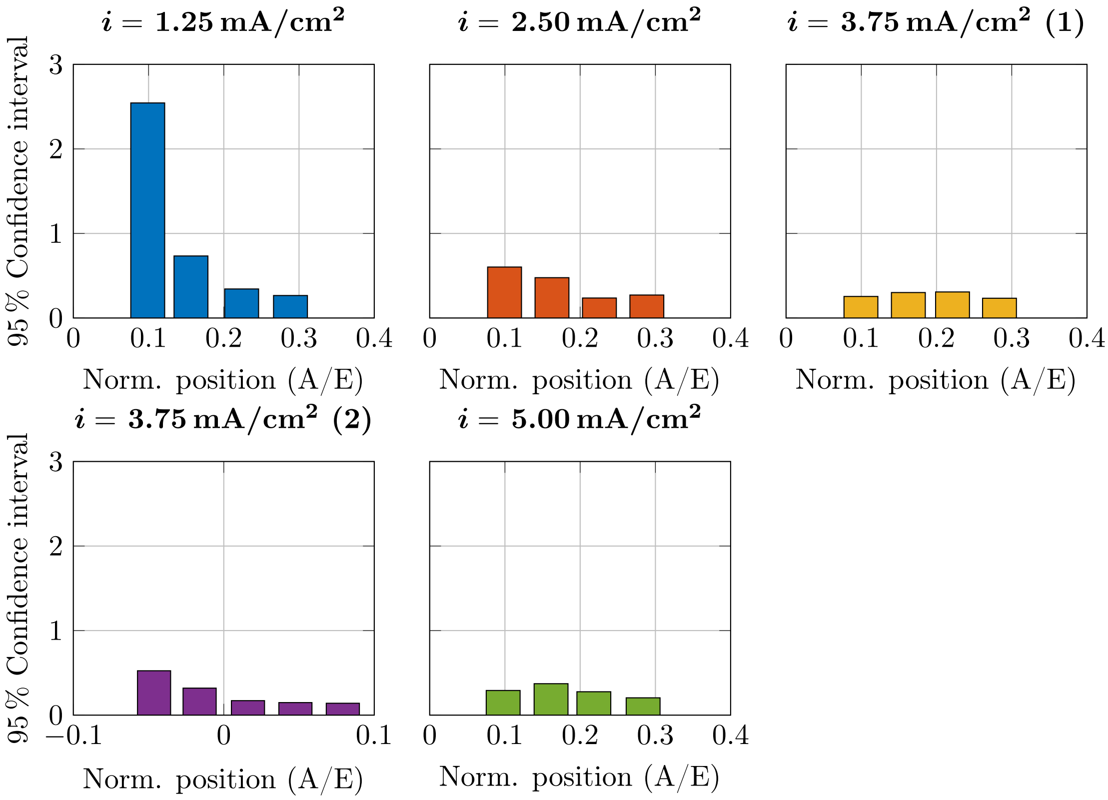

Figure B.9. 95 % confidence intervals for the final measurements of mean bubble size plotted as function of the normalised horizontal position (A/E).

B.3.2 Mean bubble velocity

The y-components of the velocity for each tracked bubble was determined as described in Section 4.5. The data are then sorted into size groups of 25 µm and the mean y-component of each size group is computed. The resulting mean y-component of the bubble velocity and corresponding standard deviations for each size group are shown in Figure B.10.

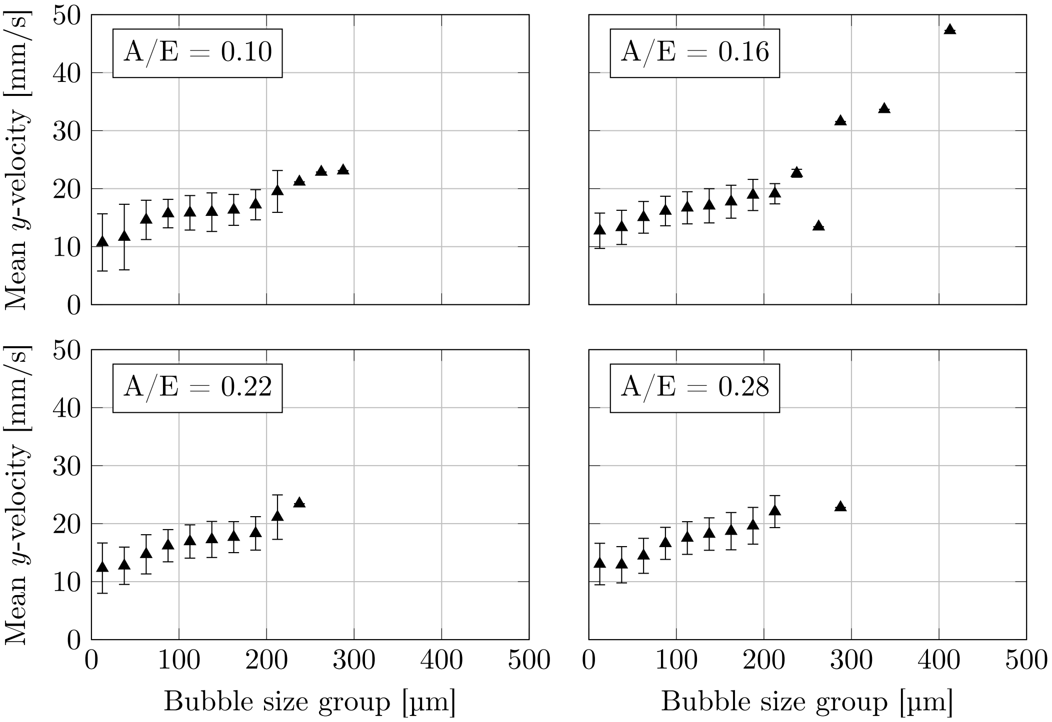

Figure B.10. Mean y-component of bubble velocity with standard deviations as function of bubble size group. Note that the cathode face plane it located at A/E = 0.0, hence the top left plot is just to the right of the cathode and the bottom right is closest to the cell wall (see Figure 4.3 on page 15).

Comparing the plots of Figure B.10 the mean y-component of the bubble velocity is seen to increase approximately linearly with the bubble size for bubbles sizes up to 225 µm across all positions from 0.10 to 0.28. For bubbles larger than 225 µm the data become sporadic, and in the case of A/E = 0.16 seemingly random, as a result of the low number of bubbles in these size groups, as shown in Figure B.11.

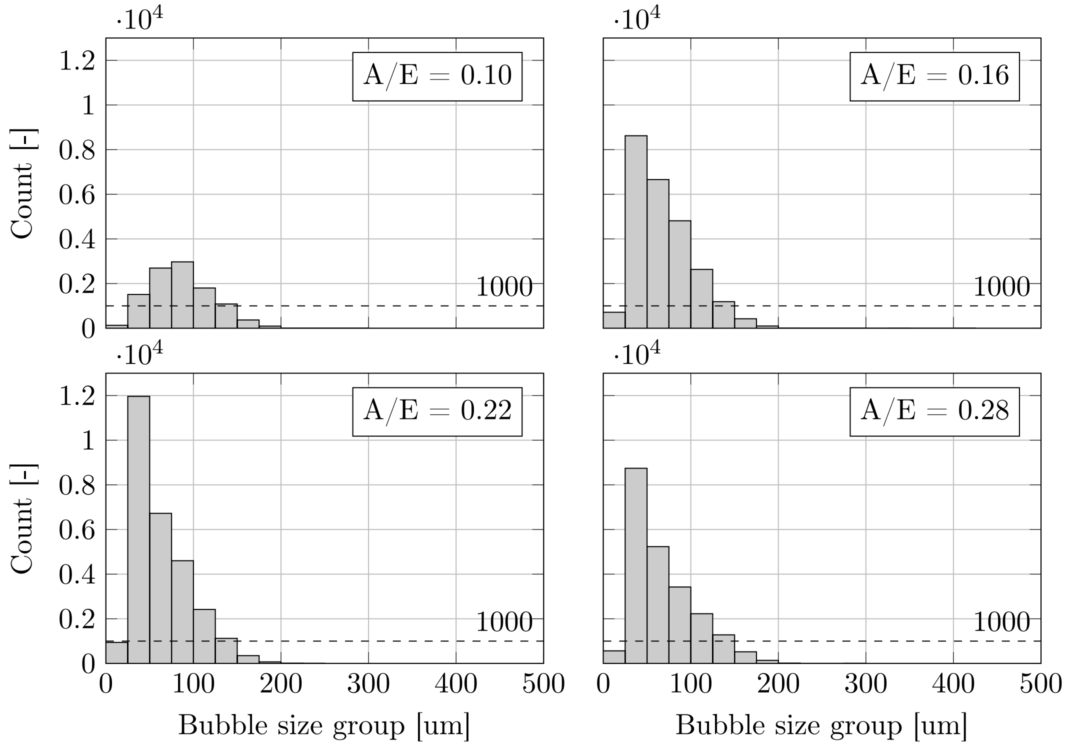

Figure B.11. Bubble count for each size group in Figure B.10. Note that the cathode face plane it located at A/E = 0.0, hence the top left plot is just to the right of the cathode and the bottom right is closest to the cell wall (see Figure 4.3 on page 15).

In order to assess the minimum number of bubbles within a size group required to be tracked to obtain a stable estimate, the mean y-component of the bubble velocity, standard deviation and confidence interval as function of the number of bubbles are shown in Figure B.12 for the size group from 25 to 50 µm at a normalised horizontal position (A/E) of 0.16. From Figure B.12 it is seen that the mean y-component of the velocity and the standard deviations reach the steady value after approximately 1000 bubbles, at which point the confidence interval has reached a value of approximately 0.2 which is found to be sufficiently small. Based on this it is chosen to only use the tracking data for the size groups with at least 1000 bubbles for the model validation in Chapter 7. Lines have been added to Figure B.11 to help identify the size groups with at least 1000 bubbles. Note that the data markers and columns in Figures B.10 and B.11 are plotted in the same order from left to right.

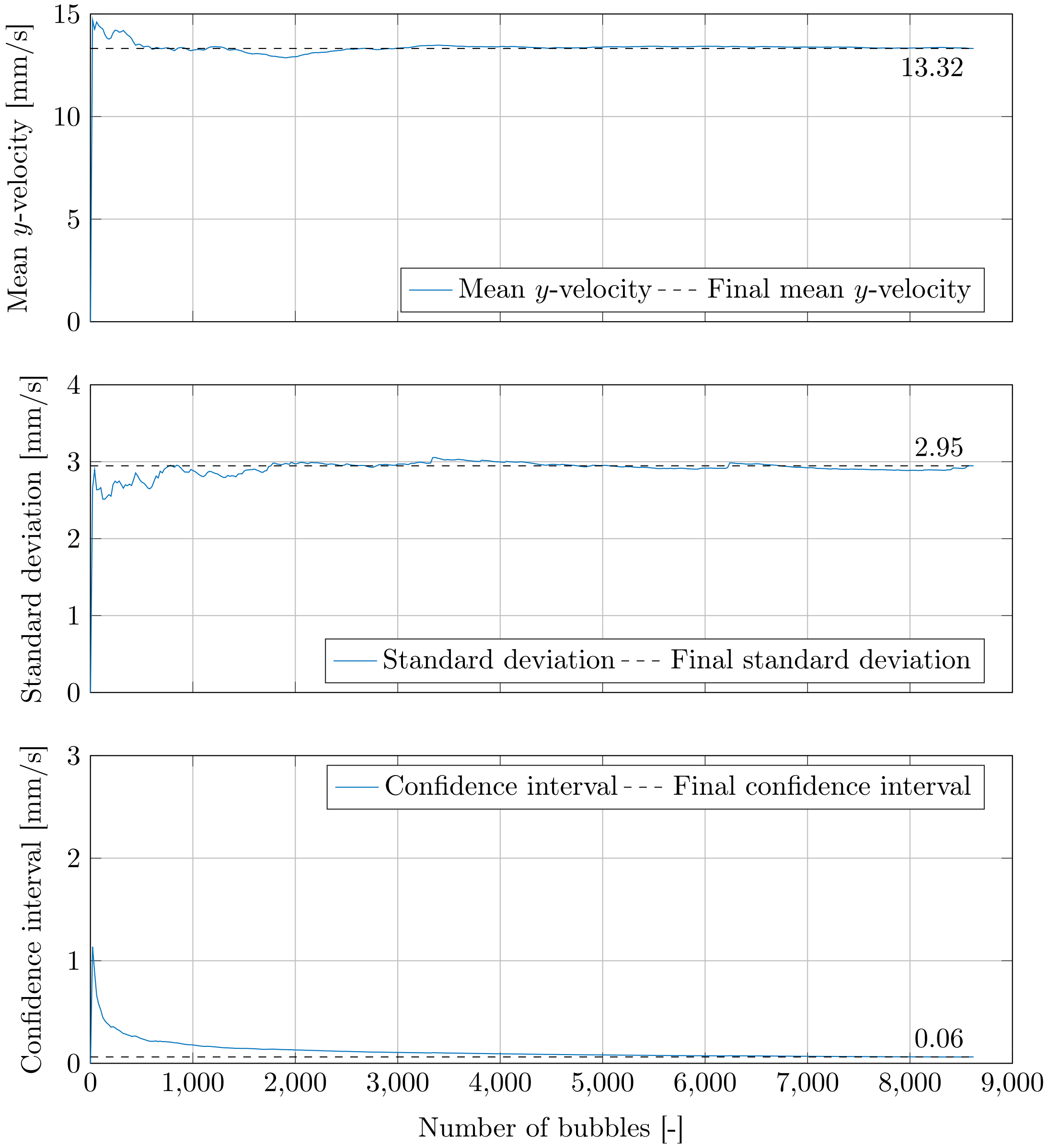

Figure B.12. Mean y-component of the bubble velocity, standard deviation and 95 % confidence interval versus the number of recognised bubbles for the bubble size group from 25 to 50 µm at a normalised horizontal position (A/E) of 0.16.

Appendix C

Tracking: Image count per sequence

This appendix investigates the necessary image count per sequence for the bubble tracking and velocity estimation described in Chapter 4.

The purpose of the bubble tracking is to estimate the mean y-component of the bubble velocity for different size groups. Hence, intuitively it would be advantageous to track the bubbles over the longest possible period of time as this would result in mean velocity estimates which are as close as possible to the true mean value. However, tracking over a longer period also introduces an increased risk of the numerical tracking algorithm loosing track of bubbles and, hence, introducing errors into the data set, as described in Section 4.5.

Thus, it is necessary to investigate how the resulting estimates of the mean y-component of the bubble velocity are influenced by the number of images used for bubble tracking. To achieve this, 30 sequences of each 30 images were captured and processed repeatedly as described in Chapter 4 with bubble tracking over 5, 10, 15, 20, 25 and 30 images. The measurement results were then grouped with respect to bubble size and the mean y-component of the bubble velocity was computed for each size group. The results are plotted in Figure C.1.

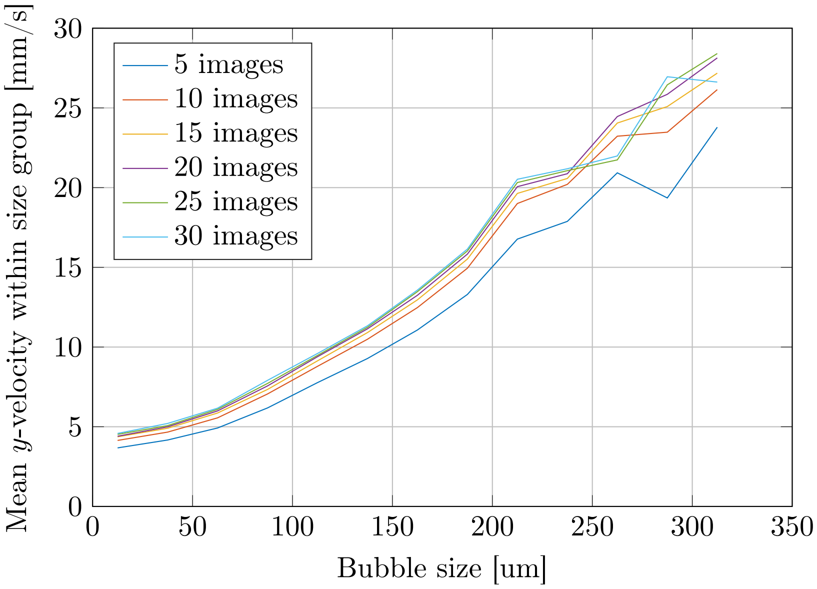

Figure C.1. Plot of the mean y-component of the bubble velocity as function of the measured bubble size for a varying number of images per sequence. The bubbles are binned into size groups of [0:25:350] µm.

Figure C.1 shows exponentially increasing y-components of the bubble velocity with increasing bubble size. This is expected considering that the volume of individual bubbles, and hence the buoyancy forces acting on the bubbles, increase exponentially with the diameter. Additionally, it is seen that the difference between the different series, as the number of images used for tracking increases, decreases and thus the mean velocity estimates move closer to the true mean.

From Figure C.1 it is assessed that it will be sufficient to track bubbles over a total of 15 images, as increasing the image count per sequence further only provides little change to the results. Moreover, increasing the number of images per sequence will increase the risk of larger bubbles moving out of the images during tracking and hence being lost, as described in Section 4.5.

Appendix D

Concepts of the pyramid-based Lucas Kanade algorithm

The following describes the concepts behind the pyramid-based Lucas Kanade (LKP) algorithm embedded in LabVIEW. For a complete and detailed description please refer to the work of Bouguet [1999].

For the following it is necessary to introduce the concept of the image pyramid representation. In this context an image pyramid representation is the repeated smoothing and subsampling of an image $I = I^0$ [Bouguet, 1999]. Put simply: I^0 is smoothed and subsampled to create I^1 which in turn is further smoothed and subsampled to create I^2, and so on up to I^{L_m}. Stacking the images I^0 through I^{L_m} on top of each other creates a pyramid with levels 0 through L_m, as shown in Figure D.1, hence the name. Each subsampling approximately halves the height and the width of the image, so if I^0 has a resolution of 640 px × 640 px, then I^1, I^2 and I^3 would have resolutions of 320 px × 320 px, 160 px × 160 px and 80 px × 80 px, respectively.

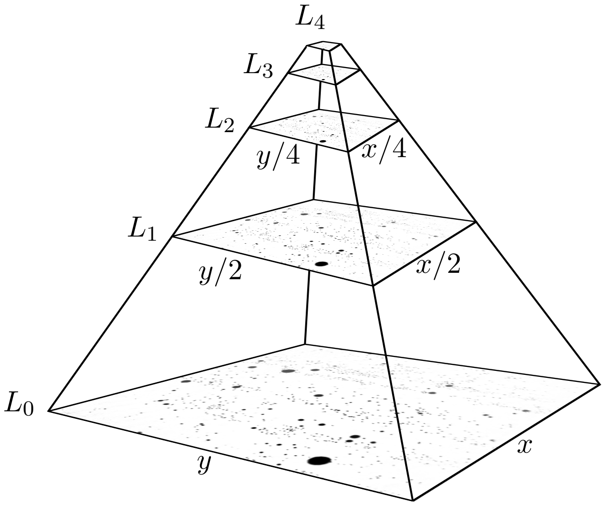

Figure D.1. Illustration of the pyramid representation concept.

Let I_{i-1} and I_i be two sequentially captured images, and $I_{i-1}(\boldsymbol{x}) = I_{i-1}(x, y)$ and $I_i(\boldsymbol{x}) = I_i(x, y)$ be greyscale values in the two images at the coordinate set $\boldsymbol{x} = (x, y)^T$. The LKP algorithm is a feature tracking algorithm which when given a coordinate set $\boldsymbol{o}_{i-1}$ in I_{i-1}, is able to find the corresponding point $\boldsymbol{o}_i$ in the current image I_i such that $I_{i-1}(\boldsymbol{o}_{i-1}) \approx I_i(\boldsymbol{o}_i)$ [Bouguet, 1999].

The LKP algorithm achieves the above by first creating pyramid representations of the images and then estimate the displacement at the deepest pyramid level L_m. The resulting estimate is then applied to the next pyramid level $L_m - 1$ as an initial guess and a refined displacement vector estimate is computed at pyramid level $L_m - 1$. The estimate from $L_m - 1$ is then used as initial guess for the further refined estimate at $L_m - 2$ and so on up to pyramid level 0, the original image [Bouguet, 1999].

At each pyramid level the displacement vector is computed iteratively by determining the residual displacement vector $\Delta \boldsymbol{S}_r^L$ which minimises the image matching error function defined in Equation (D.1) [Bouguet, 1999].

$$\begin{aligned}
&\varepsilon^L(\Delta S_{r,x}^L, \Delta S_{r,y}^L) \\
&\quad = \sum_{x=o_{i-1,x}^L-\omega_x}^{o_{i-1,x}^L+\omega_x} \sum_{y=o_{i-1,y}^L-\omega_y}^{o_{i-1,y}^L+\omega_y} \left[I_{i-1}^L(x,y) - I_i^L(x+\xi_x^L+\Delta S_{r,x}^L, y+\xi_y^L+\Delta S_{r,y}^L)\right]^2
\end{aligned} \tag{D.1}$$

where:			
	ε^L	Image matching error at the L^{th} level	[−]
	$\Delta S_{r,x}^L$, $\Delta S_{r,y}^L$	Residual displacement vector components at the L^{th} level	[px]
	ξ_x^L, ξ_y^L	Guess vector components at the L^{th} level	[px]
	ω_x, ω_y	Integers which defines the search area	[px]

The displacement is then computed as the sum of the residual displacement vector and the guess vector at pyramid level L_0 as shown in Equation (D.2) [Bouguet, 1999].

$$\Delta \boldsymbol{S} = \boldsymbol{\xi}^0 + \Delta \boldsymbol{S}_r^0 \tag{D.2}$$

where:			
	$\Delta \boldsymbol{S}$	Displacement vector	[px]
	$\boldsymbol{\xi}^0$	Initial guess vector for the original image	[px]
	$\Delta \boldsymbol{S}_r^0$	Residual displacement vector for the original image	[px]

From Equation (D.1) it can be seen that the use of the guess vector $\boldsymbol{\xi}^L = (\xi_x^L, \xi_y^L)$ results in the residual displacement vector $\Delta \boldsymbol{S}_r^L = (\Delta \boldsymbol{S}_{r,x}^L, \Delta \boldsymbol{S}_{r,y}^L)$ being small and hence computed easily by minimising Equation (D.1) [Bouguet, 1999].

Appendix E

Methods for flow visualisation

From the set of subsequently captured images the flow can be visualised by calculating the velocity vectors. These are calculated through the Adaptive correlation, and the false vectors which may appear are detected and substituted through Universal Outlier Detection.

E.1 Adaptive correlation

Generally, correlations such as cross-correlation, adaptive correlation and average correlation are calculated using the Fast Fourier Transform (FFT), giving a faster calculation speed than a direct implementation would. The FFT method transforms the spatial domain into the frequency domain and then back again, and correlates across the interrogation area (IA) boundary using the assumption that the input particle patterns are cyclic. [Dantec Dynamics A/S, 2015]

The adaptive correlation calculates the velocity vectors based on an initial interrogation area (IA) of N times the size of the final IA [Dantec Dynamics A/S, 2015]. The intermediate results are then used as inputs for the next IA of smaller size, until the final IA size is reached [Dantec Dynamics A/S, 2015]. The IA is defined in terms of horizontal and vertical dimensions given in pixels. When a number of refinement of 3 is selected together with an IA of 32 x 32 pixels, as it is the case of the current application, the initial IA size is 128 x 128 pixels.

During the processing vector field resolution can be lost. In order to compensate for this an overlap of the IA is used, often with a value of 25%. In other words, the "overlap" parameter defines a relative overlap between neighboring IAs. In Figure E.1 an interrogation area is depicted together with neighboring overlap areas at horizontal and vertical overlap of 50%. [Dantec Dynamics A/S, 2015]

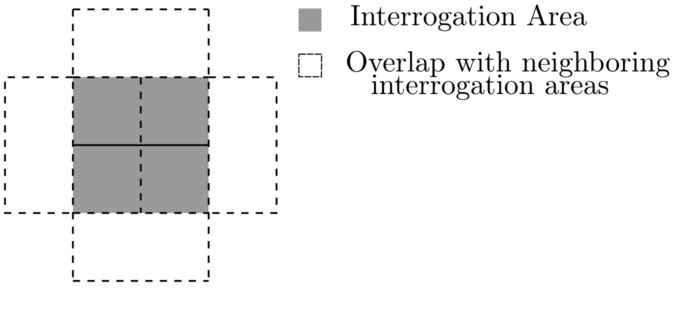

Figure E.1. Interrogation areas and corresponding overlap areas for horizontal and vertical overlap of 50%. Inspired by [Dantec Dynamics A/S, 2015].

Having the possibility of defining the overlap in both the horizontal and the vertical direction, which results in the freedom of increasing the resolution of the vector map in any direction, thus compensating for the resolution loss which may occur [Dantec Dynamics A/S, 2015].

The validation parameters of the adaptive correlation are used to fine-tune the processing by identifying and eliminating invalid vectors. DynamicStudio offers two types of validations, which can be used individually or in combination - "Peak validation" and "Local neighborhood validation". The Peak validation identifies the spurious vectors, but cannot approximate the correct vector, thus the false vector is simply replaced with zero. Because this estimate is not always realistic, this validation method is combined with the "Local neighborhood validation", which is able to make a realistic estimate of what the invalid vector should have been. This validation method compares single vectors to the local vectors comprised in the neighborhood vector area defined by the user. The invalid vector is detected, then it is removed or replaced by a vector determined through local interpolation of the vectors present in the local area. The interpolation can be done either by moving average or by local median. [Dantec Dynamics A/S, 2015]

In this study, an area of 3 x 3 pixels and a moving average interpolation were used. The mean particle displacements inside the IA determine the velocity vectors as follows:

$$\Delta S(\vec{X}; t_0, t_{+1}) \approx \int_{t_0}^{t_{+1}} u[\vec{X}(t), t] dt \tag{E.1}$$

where:			
	ΔS	Displacement	[px]
	u	Velocity	[m/s]
	t	Time	[s]

The formula is converted into an algebraic equation by using the Central or Forward Difference Schemes. It is noted by Dantec Dynamics A/S [2015] that the Central Difference Scheme works well in PIV applications, therefore it is used for the flow visualisation inside the electrochlorination cell. [Dantec Dynamics A/S, 2015]

E.2 Universal Outlier Detection

The Universal Outlier Detection (UOD) recognises invalid vectors, which may alter the final results, and in addition it gives the possibility of replacing them. The UOD is commonly used in analysing PIV data because it is able to handle different flow conditions and characteristics.

In DynamicStudios the neighborhood size (given by an uneven MxN number of vectors), detection threshold and the minimum normalisation level can be specified. The result can be validated and the false vectors rejected or replaced with a median vector, which is calculated using the neighborhood vectors. The displacement vector can be substituted by its median vector if the normalised vector residual is above the chosen detection threshold.

The calculation of the normalised vector residual, r_0, is given by Equation (E.2).

$$r_0 = \frac{|\Delta S_0 - \boldsymbol{U}_m|}{r_m + \epsilon} \tag{E.2}$$

where:

r_0	Normalised vector residual
ΔS_0	Displacement vector
$\boldsymbol{U}_m$	Median vector
r_m	Median residual
ϵ	Minimum normalisation level

The algorithm of the method is defined to ignore vectors which were previously rejected and in the case that the targeted displacement vector turns out to be a false one, it is left unchanged. When one or more of the vectors in the neighborhood area are invalid, these are left out of the median calculation. Moreover, if none of the neighboring vectors can be used for the median calculation, the displacement vector is left unchanged also in this case. [Dantec Dynamics A/S, 2015]

In Figure E.2 it is shown how the spurious vectors are identified for the flow above the cathode in the case of a correlation for which UOD is applied. It can be seen by comparing the two cases that most of the invalid vectors are found, then replaced with vectors which make the flow visualisation smoother.

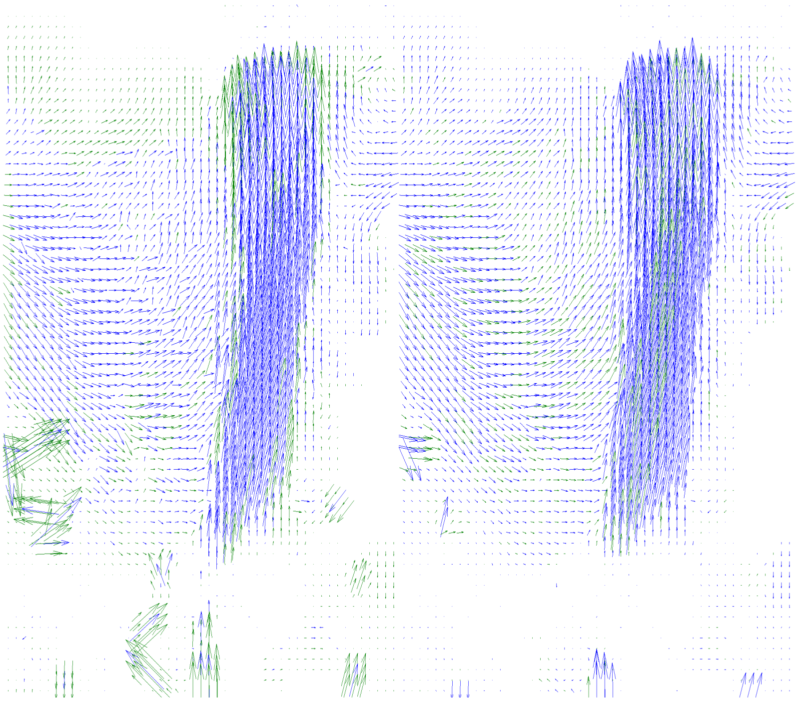

Figure E.2. Cross-correlations - without UOD (left) and with UOD analysis (right).

For this UOD analysis a neighborhood area of 5 x 5 pixels, detection threshold of 1.0, and a normalisation level of 0.10 pixels were chosen. In addition, the invalid vectors are substituted.

APPENDIX F

Finite Element Method

COMSOL Multiphysics uses the finite element method (FEM) for solving the linear and non-linear partial differential equations (PDE) on which the modules are based.

The following describes the basic ideas about the FEM and introduces the Galerkin method.

F.1 Basic Ideas

FEM is a technique used to solve differential equations numerically. This is done by firstly rewriting the differential equation, also known as strong form, into its corresponding weak form, which is a variational equation obtained by multiplying the strong form with a set of carefully selected test functions. This allows for a relaxation of the solution, due to the fact that weak forms accept a larger range of functions than the strong form. The solution to this weak form is obtained in a finite dimensional function space defined by simple functions, such as polynomials. The construction of this space involves the division of the computational domain into a mesh of geometrical elements, such as triangles, quadrilaterals or tetrahedrons. [Bengzon, 2009]

To introduce the basic aspects of FEM, the quasi-harmonic Poisson equation is considered:

$$-\frac{\partial}{\partial x_i}\left(k\frac{\partial \varphi}{\partial x_i}\right)+\Lambda=0 \tag{F.1}$$

where:			
	k	Thermal conductivity	[(W/(m K))]
	φ	Potential function	
	Λ	Generic source term	

Setting appropriate boundary conditions of Dirichlet, Equation (F.2) or Neumann, Equation (F.3), type defines the problem uniquely.

$$\varphi=\bar{\varphi} \text{ on } \Gamma_\varphi \tag{F.2}$$

$$q_n=-k\frac{\partial\varphi}{\partial n}=\bar{q}_n \text{ on } \Gamma_q \tag{F.3}$$

where:			
	Γ_q	Control surface for definition of q	[m^2]
	Γ_ϕ	Control surface for definition of φ	[m^2]
	q	Heat flux	[W/(m^2)]

Equation (F.1) is the *strong form* of the problem. Its direct use implies the computation of second order derivatives using approximation techniques. This can be circumvented by considering an integral expression over the domain Ω for Equation (F.1) expressed by Equation (F.4).

$$\int_{\Omega} v \left[-\frac{\partial}{\partial x_i} \left(k \frac{\partial \varphi}{\partial x_i} \right) + \Lambda \right] d\Omega = 0 \tag{F.4}$$

where:			
	Ω	Domain surface	[m^2]
	v	Arbitrary function	

The terms in Equation (F.4) are integrated by parts, the boundary being divided into two parts, denoted Γ_φ and Γ_q, with $\Gamma = \Gamma_\varphi \cup \Gamma_q$, and by making use of Equation (F.3), Equation (F.4) becomes:

$$\int_{\Omega} \frac{\partial v}{\partial x_i} \left(k \frac{\partial \varphi}{\partial x_i} \right) d\Omega + \int_{\Omega} v \Lambda d\Omega + \int_{\Gamma_q} v \bar{q}_n d\Gamma = 0 \tag{F.5}$$

Equation (F.5) is known as the *weak form* of the problem, because it is defined only in terms of first order derivatives. [Zienkiewicz et al., 2005]

F.2 The Galerkin method

As mentioned in Chapter 6 modelling species transport and multiphase flows involves highly non-linear PDEs, which in turn give a highly non-linear problem to solve. Thus, it was decided to opt for a time-dependent solution to the problem.

COMSOL Multiphysics incorporates efficient and accurate integration schemes applied to the finite element method expressed through an integral property, the Galerkin method [Zimmerman, 2006]. This section is written based on Thomas Condra and Erik Lund [2016]

Galerkin method for 1D diffusion problem

To simplify the following, the discretization pathway for the Galerkin method is illustrated here using a 1D diffusion problem. The governing equation for a 1D heat transfer problem is given by Equation (F.6).

$$\int_{\forall} \frac{d}{dx} \left(k \frac{dT}{dx} \right) d\forall + \int_{\forall} \Lambda d\forall = 0 \tag{F.6}$$

where:			
	$\forall$	Volume	[m^3]
	T	Temperature	[K]

For this equation the diffusion coefficient k is allowed to vary over the domain. Inserting an approximation of the temperature function, $\tilde{T}$, in the governing equation will cause the equation not to hold exact solutions and thus residuals are defined in order to measure the error. The Galerkin method, based on weighted residuals, is used to obtain the needed equations. Firstly, the temperature field $\tilde{T}$ is linearly interpolated along the element by using the shape functions, N_i, and the corresponding nodal temperature values T_i, as given in Equation (F.7), where i is the local node number of the element. In a 1D space each element has 2 nodes.

$$\tilde{T} = \sum_{i=1}^{n} N_i T_i \tag{F.7}$$

where:			
	$\tilde{T}$	Temperature field	[K]
	N_i	Shape function	

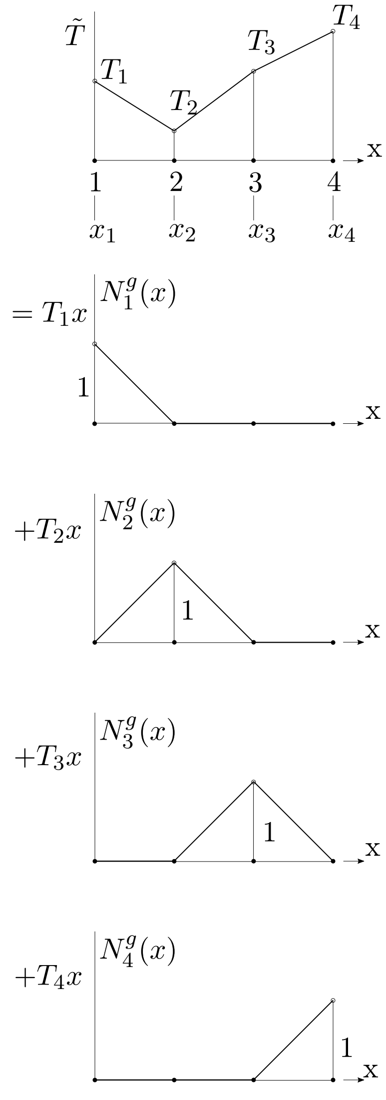

Figure F.1. 1D Galerkin weighting with linear shape functions for four nodes [Thomas Condra and Erik Lund, 2016].

For the Galerkin method the approximation function $\tilde{T}$ is inserted in Equation (F.6) and to measure the error which is introduced the equation is multiplied by a weighted function $w(x)$, Equation (F.8). In addition, the weight functions are chosen to be the shape functions, N_i. An example of a visual 1D Galerkin weighting on four elements with linear shape functions is shown in Figure F.1.

$$\int_{\not{V}} w(x) \left(\frac{d}{dx} \left(k \frac{d\tilde{T}}{dx} \right) + \Lambda \right) d\not{V} = \int_{x} w(x) \left(\frac{d}{dx} \left(Ak \frac{d\tilde{T}}{dx} \right) + \Lambda A \right) dx \tag{F.8}$$

Integrating by parts as also shown in Appendix F.1, considering that the computational domain is defined as $0 \leq x \leq l$ and the weighted functions are considered to be differentiable once, the weak function of the heat conduction problem for one finite element is obtained:

$$\left[wAk\frac{d\tilde{T}}{dx} \right]_0^l - \int_0^l \frac{dw}{dx}Ak\frac{d\tilde{T}}{dx}dx + \int_0^l w\Lambda A dx = 0 \tag{F.9}$$

The first and last term of Equation (F.9) are given by the Neumann boundary condition (Equation (F.3)) and distributed load, respectively. Replacing the weight function $w(x)$ with the linear shape functions N_i the Galerkin residuals can be derived, one for each node of the element. Here, a 1D element is considered, thus two residual equations can be written, one for each shape function N_i.

$$\begin{aligned} \int_0^l \frac{dN_1}{dx}Ak\frac{d\tilde{T}(x)}{dx}dx &= -[N_1 A q_x]_0^l + \int_0^l N_1 \Lambda A dx \\ \int_0^l \frac{dN_2}{dx}Ak\frac{d\tilde{T}(x)}{dx}dx &= -[N_2 A q_x]_0^l + \int_0^l N_2 \Lambda A dx \end{aligned} \tag{F.10}$$

To get the discretized equation for one finite element the shape functions and the approximation function have to be differentiated. The nodal temperature values T_e are related to fixed nodal points in space, only the shape functions $N_i(x)$ varying with the position x. Thus, by differentiating the approximation function the following is obtained:

$$\frac{d\tilde{T}}{dx} = \frac{d([N]\{T^e\})}{dx} = \frac{d[N]}{dx}\{T^e\} \tag{F.11}$$

Hence, the discretized equations for one finite element is obtained:

$$\int_0^l \frac{d[N]^T}{dx}Ak\frac{d[N]}{dx}dx\{T^e\} = -[[N]^T A q_x]_0^l + \int_0^l [N]^T \Lambda A dx \tag{F.12}$$

This concludes the description of the FEM used in COMSOL Multiphysics.

Appendix G

2D representation and zooms

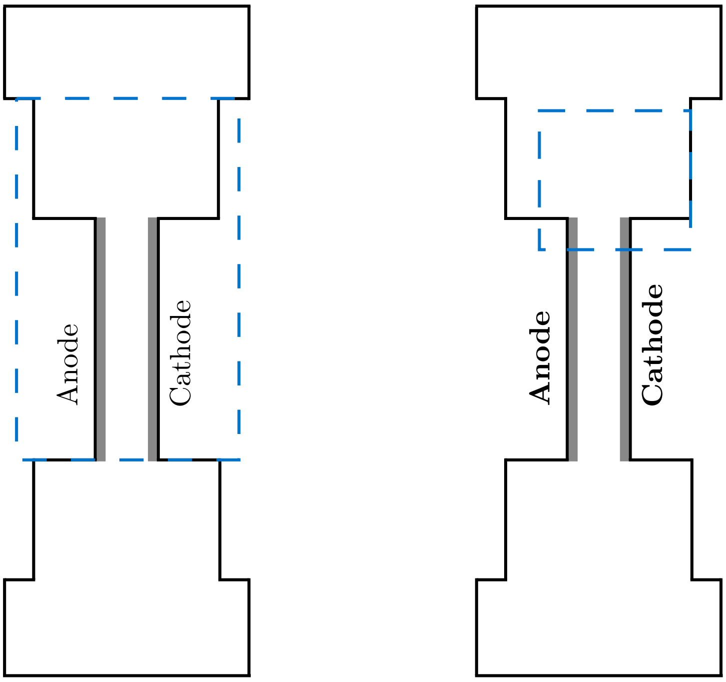

(a) Zoom at region defining model geometry.

(b) Zoom at region for flow visualisation comparison.

Figure G.1. Illustration of two zooms at regions defining model geometry and flow visualisation comparison, respectively.

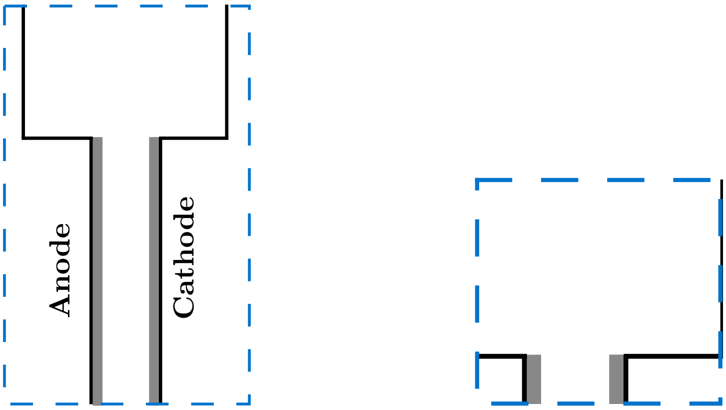

(a) Model geometry.

(b) Region for flow visualisation comparison.

Figure G.2. Model geometry and region for flow visualisation comparison.

APPENDIX H

CD

The attached CD contains:

Description	**File name**
Digital version of the report	Report.pdf
Digital version of the executive summary	Executive summary.pdf
Digital version of the conference paper	ConfPaper.pdf
Digital version of the poster	Poster.pdf
Image preprocessing MATLAB script	imgPreProcessing.m
MATLAB function for background division (image preprocessing)	bgDiv.m
MATLAB function for normalisation (image preprocessing)	imNorm.m
MATLAB function for contrast enhancement (image preprocessing)	contrastENH.m
LabVIEW program for image processing	Bubble measurements.vi
LabVIEW program for bubble tracking	Bubble tracking.vi
COMSOL Multiphysics model with 7.68 mm cell gap geometry (without solution)	LargeCellGapGeometry.mph
COMSOL Multiphysics model with 2 mm cell gap geometry (without solution)	SmallCellGapGeometry.mph
Folder containing example images for the preprocessing script	PREP-IMGS

Please note that the LabVIEW scripts cannot be run, due to the absence of images to be processed, as well as the lack of the file structure implemented in these.